Summer 8-15-2015

Using Fluorescence – Polarization Endoscopy in Detection of Precancerous and Cancerous Lesions in Colon and Pancreatic Cancer

Tauseef Charanya
Washington University in St. Louis

WASHINGTON UNIVERSITY

School of Engineering and Applied Science
Department of Biomedical Engineering

Dissertation Examination Committee

Samuel Achilefu, Chair
Mark Anastasio
Joseph Culver
Viktor Gruev
Deborah Rubin
Lihong Wang

Using Fluorescence – Polarization Endoscopy in Detection of Precancerous and Cancerous Lesions in Colon and Pancreatic Cancer

By

Tauseef Charanya

A dissertation presented to the
Graduate School of Arts and Sciences
of Washington University in
partial fulfillment of the
requirements for the degree
of Doctor of Philosophy

August 2015
St. Louis, Missouri

Table of Contents

Acknowledgements

I would like to thank several people for (i) getting me to the opportunity to pursue a PhD and (ii) for helping me through the process.

I would like to thank my parents who made the bold move of moving from India to the U.S. during the later stage in their career, for the sole purpose their children's education. Along with my sister, they have been nothing but supportive in encouraging me to always shoot for the stars and pursue my dream. I would like to thank my wife, Aliya for always being there for me, even in the most difficult and stressful times. Her love and support has always helped me go the extra mile personally, and professionally. I would have not been the first PhD in my family if it was not for aforementioned individuals.

As for during my PhD, I am most grateful to having Dr. Achilefu as my advisor. He has been one of the most understanding and influential people I have witnessed in my life thus far. Dr. Achilefu knew what it took to challenge myself and he provided me with all the resources to do so throughout my tenure as his graduate student. He guided me through identifying a clinically relevant problem that interested me most and putting together a successful NIH grant proposal. Dr. Achilefu has and will continue to serve as a true role-model, where his work ethic, scientific curiosity, and humbleness continue to inspire me every day.

Along with Dr. Achilefu, I would like to thank my thesis committee comprised of Dr. Viktor Gruev, Dr. Deborah Rubin, Dr. Lihong Wang, Dr. Joseph Culver and Dr. Mark Anastasio who have always opened their doors to me and shared their expert opinions in their respective fields. I have been fortunate enough to have such great minds and leading experts in their

respective fields come together and provide their input on helping me achieve goals established for my project.

Furthermore, I would like to thank members of the Optical Radiology Lab who have always helped me keep my spirits high during my PhD, especially Avik Som, Adnan Muhammed, Mrinal Pahwa and administrator Brenda Phelps. I would like to thank members of the group who have always taken interest in my work and indulged in deep scientific conversations with me such as Nalini Kotagiri and Christopher Egbulefu. I would like to thank collaborators Viktor Gruev and his students, Timothy York and Missael Garcia for their contributions towards my project.

While these are just a few of the people I am thankful to, it would be impossible to record all the people who have helped me get to where I am today. I have been fortunate enough to be surrounded by remarkable individuals throughout the course of my PhD.

Tauseef Charanya

Washington University in St. Louis

August 2015

ABSTRACT OF THE DISSERTATION

Using Fluorescence-Polarization Endoscopy in Detection of Precancerous and Cancerous Lesions in Colon and Pancreatic cancer

By

Tauseef Charanya

Doctor of Philosophy in Biomedical Engineering

Washington University in St. Louis, 2015

Professor Samuel Achilefu, Chair

Colitis-associated cancer (CAC) arises from premalignant flat lesions of the colon, which are difficult to detect with current endoscopic screening approaches. We have developed a complementary fluorescence and polarization reporting strategy that combines the unique biochemical and physical properties of dysplasia and cancer for real time detection of these lesions. Utilizing a new thermoresponsive sol-gel formulation with targeted molecular probe allowed topical application and detection of precancerous and cancerous lesions during endoscopy.

Incorporation of nanowire-filtered polarization imaging into NIR fluorescence endoscopy served as a validation strategy prior to obtaining biopsies.

In order to reduce repeat surgeries arising from incomplete tumor resection, we demonstrated the efficacy of the targeted molecular probe towards margins of sporadic colorectal cancer (SCC). Fluorescence-polarization microscopy using circular polarized (CP) light served as a rapid, supplementary tool for assessment and validation of excised tissue to ensure complete tumor resection for examining tumor margins prior to H&E-based pathological diagnosis. We extended our platform towards non-invasive directed detection of pancreatic cancer utilizing fluorescence molecular tomography (FMT) and NIR laparoscopy using identified targeted molecular probe. We were able to non-invasively distinguished between pancreatitis and pancreatic cancer and guide pancreatic tumor resection using NIR laparoscopy.

Chapter 1

1.1 Overview of Doctoral Research and Dissertation

My doctoral research focuses on the development of an endoscope capable of detecting near infrared (NIR) fluorescence and tissue-sensitive polarized light information from suspect colon cancer lesions. During this doctoral study, I have identified a targeting molecular probe for detection of precancerous and cancerous lesions, explored delivery routes of molecular probes for *in vivo* application, and demonstrated the use of the novel fluorescence-polarization endoscopy and associated microscopy. The dissertation is structured as follows: Chapter 1 is an introduction to sporadic and colitis-associated cancer (CAC), targeted NIR molecular imaging, and fluorescence-polarization imaging. Chapters 2-6 derive in large part from published journal manuscripts or manuscripts in preparation, where I was a lead author. Chapter 7 presents a concise summary of the dissertation with conclusions.

1.2Epidemiology and Clinical Standards in Staging and Treatment of Colorectal Cancer

1.2.1 Sporadic colorectal cancer (SCC) and colitis-associated cancer (CAC)

Every year in the United States alone, there are 160,000 cases of colorectal cancer diagnosed, and 57,000 reported deaths making it the second leading cause of death from cancer amongst adults[1]. Colorectal cancer (CRC) can be divided into two primary categories: sporadic colorectal cancer (SCC) and colitis-associated cancer (CAC). While sporadic colorectal cancer is more common, it is known that people who suffer from inflammatory bowel disease (IBD), comprised of Crohn's disease and ulcerative colitis, are at a greater risk of developing CAC. As

many as 1.4 million people in the United States alone suffer from IBD. A meta-analysis of colorectal cancer risk suggests a cumulative incidence of malignancy of 2% by 10 years, 8% by 20 years and 18% by 30 years post diagnosis[2]. Because the peak onset of this disease occurs in the second and third decades of life, these patients are subject to a two-fold or greater lifetime risk of developing colorectal cancer than normal subjects[3]

Both, SCC and CAC arise from pre-cancerous dysplastic mucosa[4]. However, approximately 67% of sporadic colorectal cancers arise from polyps, whereas colitis-associated cancers typically arise from flat dysplastic mucosa. In CAC, evidence for dysfunctional signaling in the Wingless (Wnt) signaling pathway, due to the adenomatous polyposis coli (APC) mutation, occurs late in the dysplasia-cancer sequence. This late occurrence likely is why polyps do not form in dysplasia-driven cancer in CAC[5]. Conversely, p53 mutation occurs at a relatively early stage in CAC, as shown in Figure 1[6]. Furthermore, duplication of chromosome 17p, which contains p53, is common even in non-dysplastic colitis of the epithelium, affecting 22% of epithelial cells, 10% of cells in normal mucosa, and 37% of the cells high-grade dysplasia and cancer[7]. For treating colorectal cancer patients, it is crucial to identify both these lesions, flat and polypoid, for improved diagnosis and establishment of treatment regime.

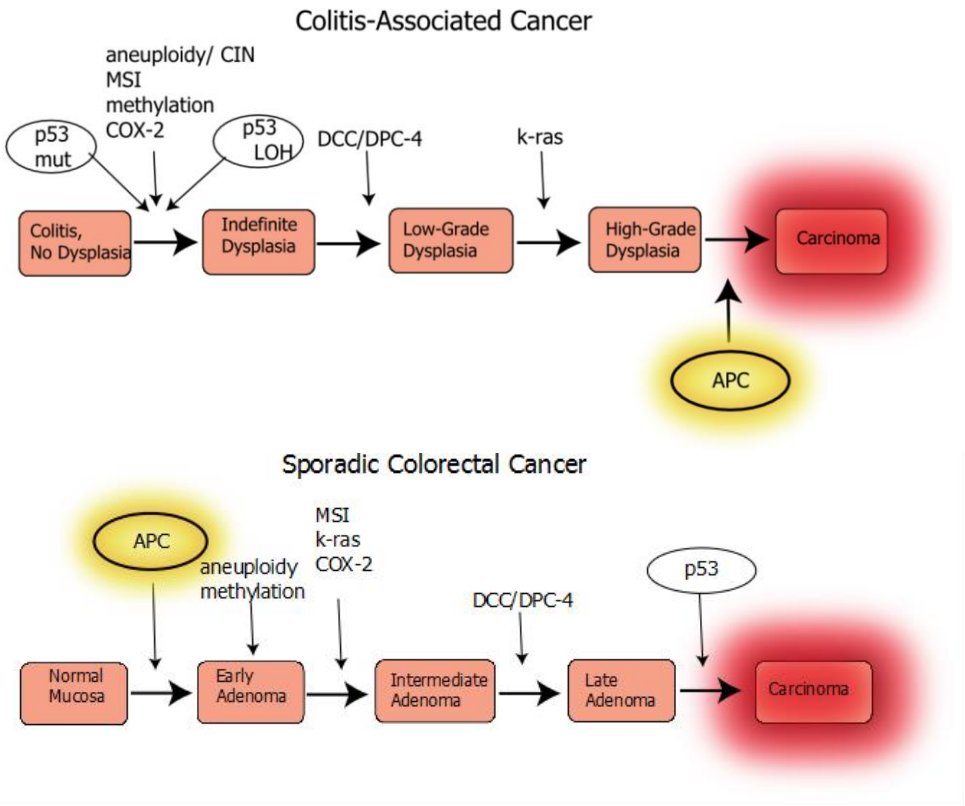

Figure 1. Mutation sequences in CAC and SCC

In conventional practice, diagnosis of colonic polyps is governed by gold standard approaches, such as endoscopic polypectomy, that rely primarily on the trained eye of the physicians performing the procedure[8]. Diagnosis of small premalignant lesions and early-stage primary tumors is crucial for the success of cancer therapy and increases survival rates. While surveillance endoscopy is the clinical standard for detection and resection of suspicious colonic cancerous lesions, the lack of an elevated growth component, such as polyps in the case of CAC, make it challenging to detect flat lesions during surveillance colonoscopy. Studies have shown up that up to 50-80% of the lesions that are missed during surveillance colonoscopy are flat[9,10]. Hence, interest has increased within the past decade in fluorescence-based and other optical imaging techniques for clinical oncology.

1.2.2 Staging and Treatment in Colorectal Cancer

By convention, staging of colon cancer is based on tumor size/invasiveness/histology by tumor node metastasis (TNM) staging. These invasive cancers can be completely curable by resection if they remain confined to the wall of the colon: mucosa-submucosa (T1-2, N0, M0 and T3-4, N0, M0). However, as the tumor invades past the muscle layers and serosa, it spreads to nearby organs (T1-4, N1-2, M0) or to even distant organs (T any, N any, M1) through lymph node involvement, making it extremely difficult to resect and leading to possible recurrence [11,12].

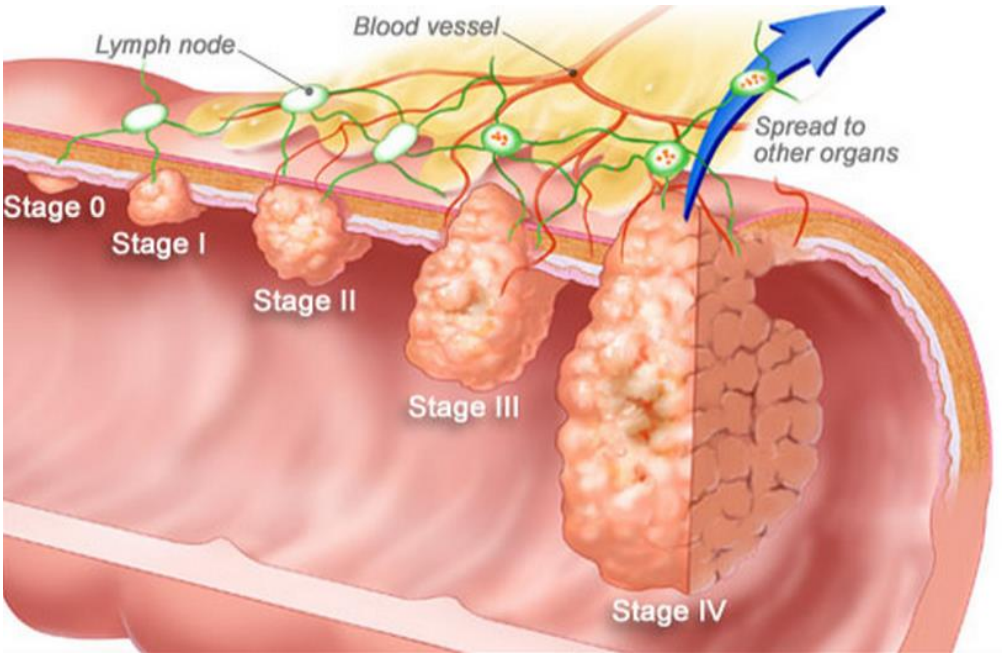

Figure 2. Staging of colorectal cancer

As shown in Figure 2, in stage 0, abnormal cells are found in the innermost layer of the colon wall and may become cancer and spread. In Stage 1, cancer has formed in the mucosa of the colon wall and has spread to the submucosal layer. There is a chance that the cancer may have already spread to the muscle layer of the colon wall. In Stage 2 IIA, cancer has spread through the muscle layer of the colon wall to the serosa (outermost layer) of the colon wall. In Stage IIB, cancer has spread through the serosa but has not

spread to the nearby organs. In Stage IIC, cancer has spread through the serosa of the colon to nearby organs. In Stage IIIA the cancer has spread to at least one but not more than three nearby lymph nodes, or cancer cells have formed in tissues near the lymph nodes. In Stage IIIB, cancer has spread to at least four but not more than six lymph nodes. In Stage IIIC, the cancer has spread through the serosa of the colon wall and to nearby organs. In Stage IVA, cancer has spread through the colon wall and to one organ that is not near the colon such as liver, lung or kidney. Last, in Stage IVB, cancer has spread through the colon wall to nearby organs or lymph nodes and spread to more than one organ that is not near the colon.

Colonoscopy plays an extremely important role in the care of patients with colorectal cancer as it is not only used for diagnosis of different stages of colorectal cancer but also treatment of early colorectal cancer and its precursors. While diagnostic challenges in early stages of colorectal cancer (lesions <1 cm and flat in nature) still persist, treatment for colorectal neoplastic lesions typically begins with hot biopsy and snare polpectomy, and endoscopic submucosal resection (EMR). In the case of large and flat lesions, techniques such as endoscopic submucosal dissection (ESD) are usually employed. EMR is an endoscopic technique developed for removal of sessile or flat neoplasms that are confined to the superficial mucosal layers (mucosa and submucosa) of the GI tract[13]. It is typically used for removal of lesions that are smaller than 2 cm. ESD, on the other hand, has specifically been developed for en bloc removal of large (more than 2 cm), flat GI tract lesions[14,15]. Pathological examination utilizing gold standard hematoxylin and eosin (H&E) stains of biopsy specimen is conducted in order to confirm the stage and complete diagnosis of the colorectal cancer patient. However, the EMR technique has yielded recurrence rates as high as 55% in some studies [16,17]. Lymph node metastasis with/without organ involvement in N0 is known to have a recurrence of 20%-30% and that of 50%-80% in T1-4, N1-2, M0 after surgery [18]. The high recurrence rates are highly attributed to incomplete tumor resection and late stage diagnosis. To address this, efforts have been directed primarily to early diagnosis of colon cancer *via* specific structural or functional characteristics that are specific to colon cancer.

1.3 Existing Detection Methods in Colitis-Associated Cancer

Recent developments in imaging technologies and the validation of newer imaging techniques may lead to significant improvements in the management of patients with colorectal cancer. Diagnostic techniques that are based primarily on structural information include, but are not limited to, high resolution microendoscopy (HRME), optical coherence tomorgraphy (OCT), narrow-band imaging (NBI), and computed tomography colonography (CTC) to name a few. Techniques that are based primarily on functional information include and are not limited to chromoendoscopy (CE), confocal laser endomicroscopy (CLE), and targeted molecular endoscopy. These technologies are briefly described below:

1.3.1 High-Resolution Microendoscopy (HRME)

HRME is a novel method for imaging colorectal mucosa at a subcellular level, with up to a 1000X magnification and resolution as fine as 4.4 μm. Developed by Muldoon et al., the device is flexible portable, and consists of 30,000 optical fibers in a 1 mm diameter bundle. The device typically uses light-emitting diode (LED) illumination and is connected to a charge-coupled device (CCD) camera[19]. Given its small size, it can be easily inserted in the accessory channel of the colonoscope to visualize sub-cellular characteristics of polyp mucosa.

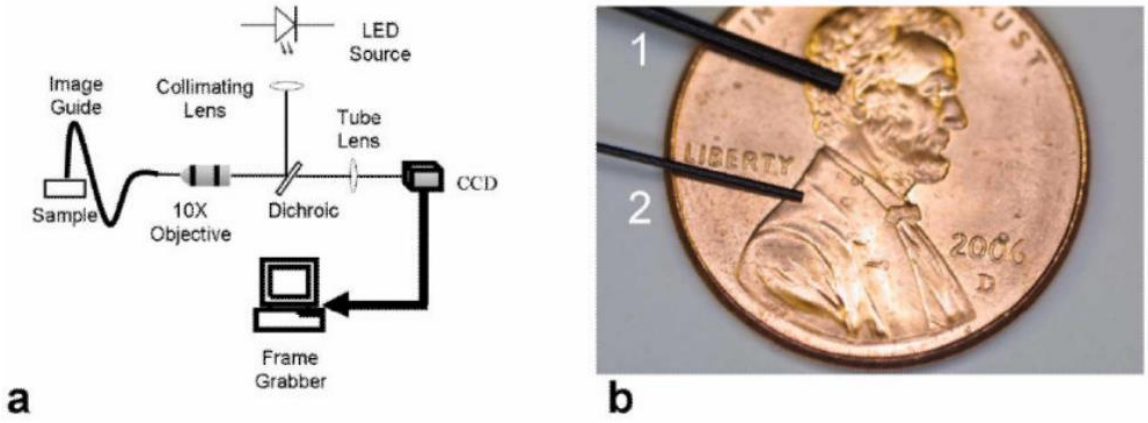

Figure 3: Fiber-optic micro endoscopy system. a) Schematic, b) fiber-optic bundle diameters, compared on a US penny[19]. Bundles one and two have outer diameters of 1 mm and 0.5 mm respectively.

Chang et al. further demonstrated the use of the HRME system in the colon[20]. The system was operated as a compact, battery-powered fluorescence microscope, coupled to a 1 mm diameter fiberoptic imaging probe. LED illumination was delivered from the HRME unit, through the imaging probe, to the tissue surface. In acquisition mode, the fluorescence light returning to the bundle was directed to a CCD that transmitted real-time images to a computer at 12 frames per second (fps), as shown in the schematic in Figure 3[20].

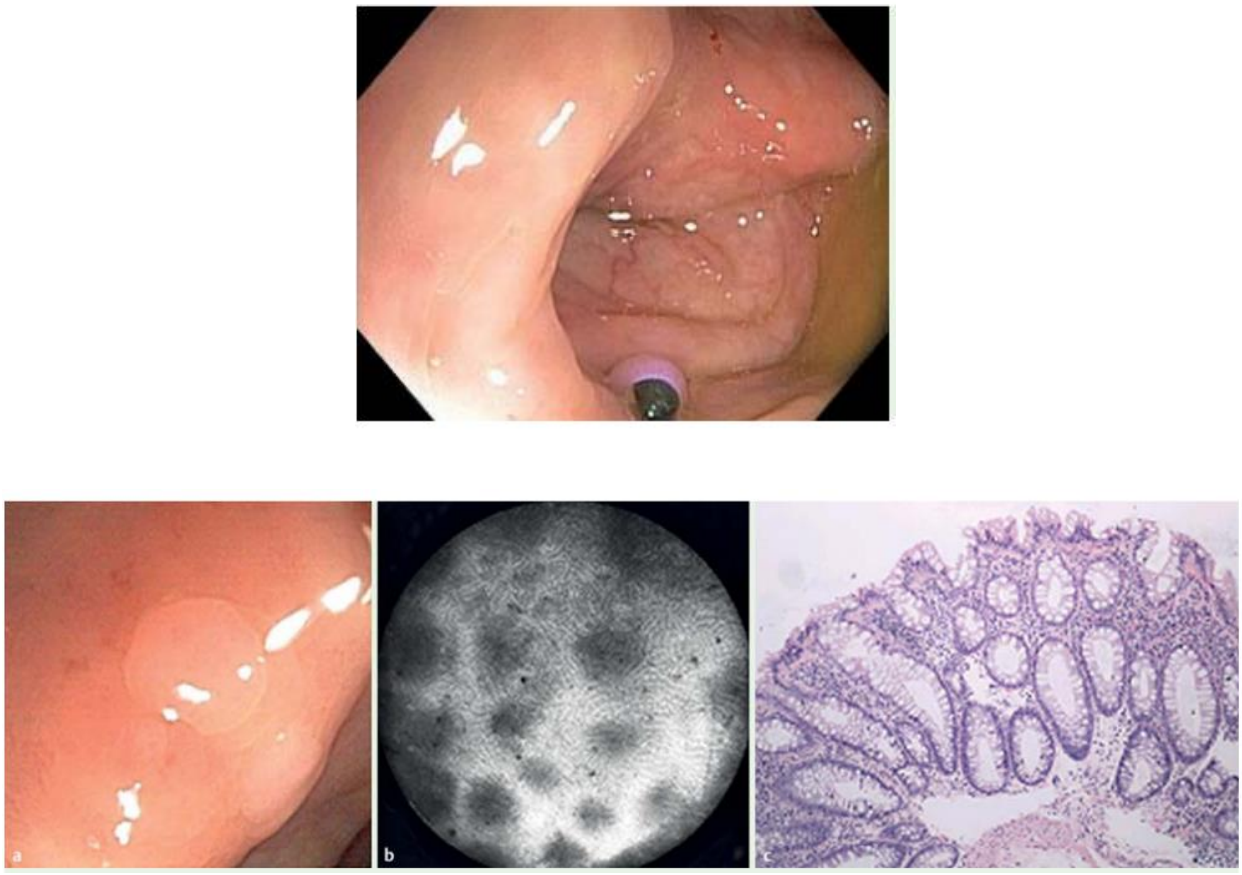

Figure 4. Use of HRME probe during colonoscopy procedure[20]. The top image is a wide field view of the colon, showing an illuminated polyp. While the polyp under white light as shown in (a) is inconclusive for diagnosis, the HRME image (b) is able to provide diagnosis regarding neoplasia or lack thereof in polyps. (c) Validated finding in H&E image[20].

While HRME provides the ability to distinguish neoplastic polyps from benign polyps with a sensitivity of 67%, a specificity of 97%, and accuracy of 87%, the utilization of this technique in identifying flat lesions in colitis-associated cancer remains problematic. Also, the HRME technique requires an expert endoscopist to identify the polyp in the first place using white light, prior to using the HRME probe for a closer microscopic examination and diagnosis. The inability

to distinguish flat lesions from their surroundings makes this technique very challenging, and time-intensive for this purpose.

1.3.2 Optical Coherence Tomography (OCT)

OCT obtains cross-sectional images of target tissue with high resolution, on the order of a low power microscope. OCT utilizes a technique known as interferometry that measures the path length of reflected light and processes the information for image generation. While OCT is very similar to ultrasound, except that it uses light as a signal instead of sound signal, OCT obtains images that correlate with the subsurface of the tissue. Sergeev et al. were one of the first groups to demonstrate the use of OCT imaging in precancerous and cancerous states of human mucosa[21]. They demonstrated the use of this system in identifying an esophageal tumor in the stomach as shown in Figure 11.

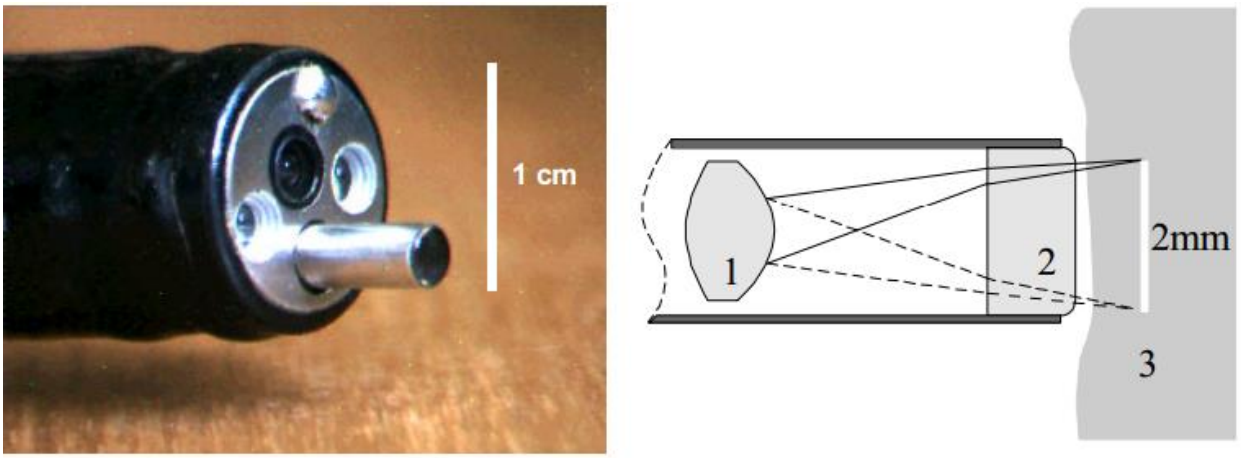

Figure 10. Distal end of the gastroscope with OCT probe, along with schematic of scanning unit on the right: 1; output lens, 2; output glass window, 3; sample.

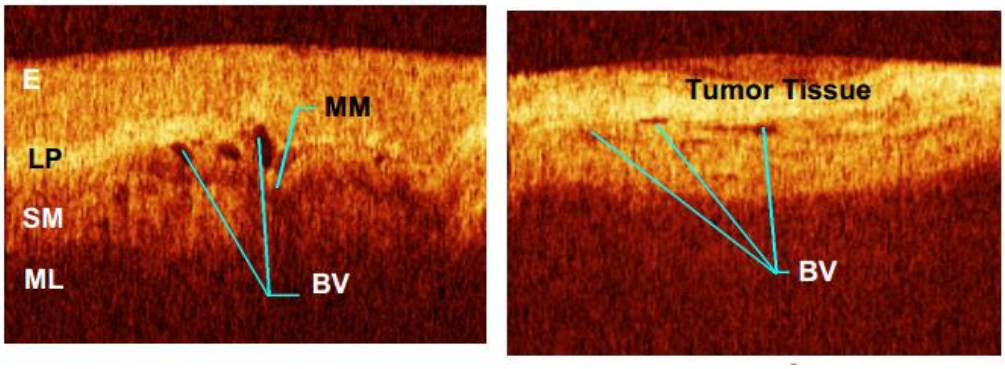

Figure 11. OCT image of healthy esophagus (left) and esophageal tumor in the stomach. E: epithelium, LP: lamina propia, SM: smooth muscle, ML: muscularis layer, BV: blood vessel

Due to their different backscattering intensities, the different mucosa layers can be identified. For example, the stratified squamous epithelium (E) appears as a weakly scattering layer, while the lamina propia appears as the most scattering layer. Furthermore, the muscularis mucosa (ML), the minimally backscattering layer, appears as a dark stripe. Also, deep layers that are submucosa (more backscattering) can be differentiated from muscular layers (less backscattering). Vessels and glands in the lamina propia (LP) are visible as circular or elongated formations. While endoscopic OCT can identify differences in well-defined stratified healthy mucosa in cancerous tissues, it does have limitations, such as non-real-time acquisition and a length procedural time.

To provide faster real-time imaging with high resolution, developments have been made towards frequency domain OCT[22]. Volumetric laser endomicroscopy can provide a resolution of 10 µm and imaging depth up to 3 mm. It can scan a 6 cm length of esophagus tissue in a minute and a half. This device has also gained clearance from the FDA. Furthermore, Tearney et al. has developed a capsule containing optical frequency domain imaging (OFDI) technology-that is

composed of a rotating laser tip emitting a beam of NIR light and sensors that record reflected backscattered light from esophageal lining. This imaging platform allows for several OCT images for the esophagus during a five minute procedure as the pill is swallowed by the patient and controlled via a tether externally by the physician[23].

1.3.3 Narrow Band Imaging (NBI)

NBI is an optical imaging enhancement technology that improves the visibility of blood vessels and other structures on the mucosa. It has demonstrated tremendous potential in tumor detection in the colon due to enhanced vascularization associated with tumors. Basically, NBI filters white light into specific shorter light wavelengths, 540 nm and 415 nm that are absorbed by hemoglobin and penetrate only the surface of human tissue. This method takes advantage of the phenomena that shorter wavelengths penetrate only the superficial layers of the mucosa, allowing capillaries to be displayed in brown on a video image. The 540 nm light penetrates deeper than 415 nm light and is absorbed by blood vessels located deeper within the mucosal layer, appearing cyan on the NBI image. The wavelength is particularly useful for detecting tumors due to enhanced vasculature appearing as brown while veins are displayed in cyan. The NBI system uses optical filters of blue (440-460 nm) and green (540-560 nm) wavelength, which enhance the visualization of blood vessels and mucosal pit patterns[24].

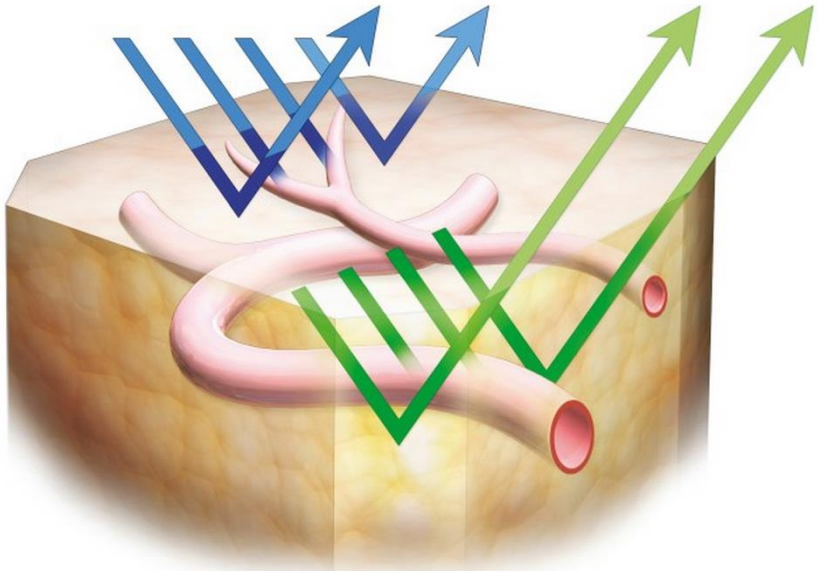

Figure 7. Narrow band imaging (NBI) uses two wavelengths, 415 nm and 540 nm, for enhanced visualization of blood vessels (Olympus, America).

However, whether the NBI system actually helps to improve colonic polyp detection remains controversial. Recently published meta-analyses failed to demonstrate any superiority of current NBI over white light endoscopy in detecting colon polyps[25-27]. The older version of the NBI yielded dimmer images, making it difficult to distinguish polyps or detect adenoma, while the newly available second generation of NBI provides a two-fold brighter image. Leung et al. compared the miss rates of adenomas using the new NBI system to WL colonoscopy and recorded a miss rate differential of 21.5% using the new NBI system[24]. They did, however, notice an improvement in the polyp detection rate of 14% over white light colonoscopy. Figure 8 demonstrates the appearance of a colorectal polyp utilizing a second generation NBI scope in a close-up and distant view.

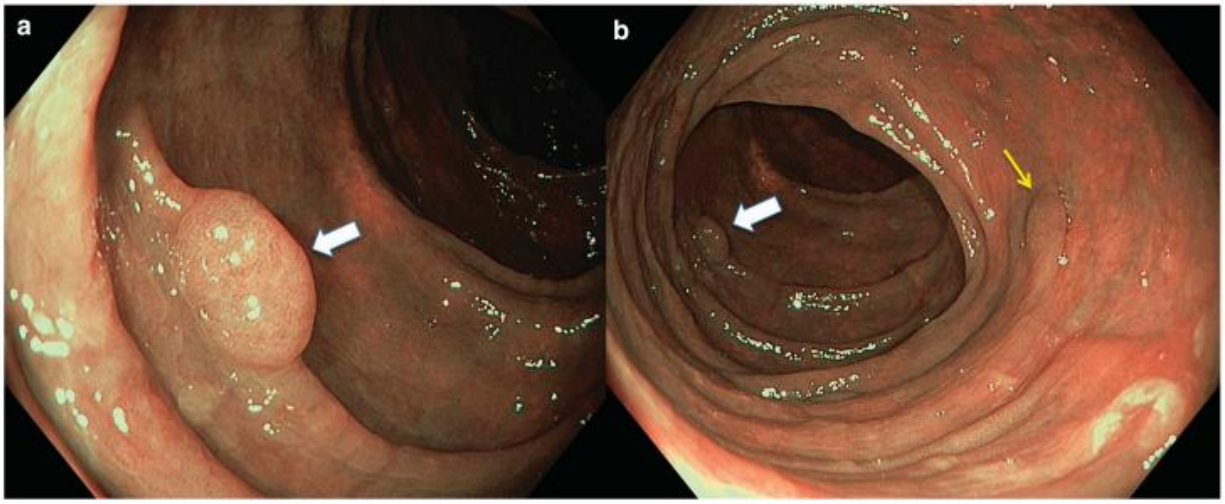

Figure 8. (a) Close-up and (b) distant view of a colorectal polyp using NBI. White arrows in (a) and (b) indicate a polyp at a closer and further view, respectively. Yellow arrow in (b) indicates a flat lesion.

1.3.4 Virtual CT colonoscopy (CTC)

CT colonography is a non-invasive radiological technique that combines a CT scanner and reconstruction methods to provide an accurate method to screen for large colorectal polyps and cancer. CTC is a quick, minimally invasive procedure that requires no anesthesia. A CT scanner obtains hundreds of X-ray images of the entire colon, and reconstruction algorithms allow for two or three dimensional images of the colon. While this technique is not recommended for everyone due to the low dose of radiation involved, it is recommended for individuals who have ulcerative colitis or Crohn's disease as a pre-existing condition.

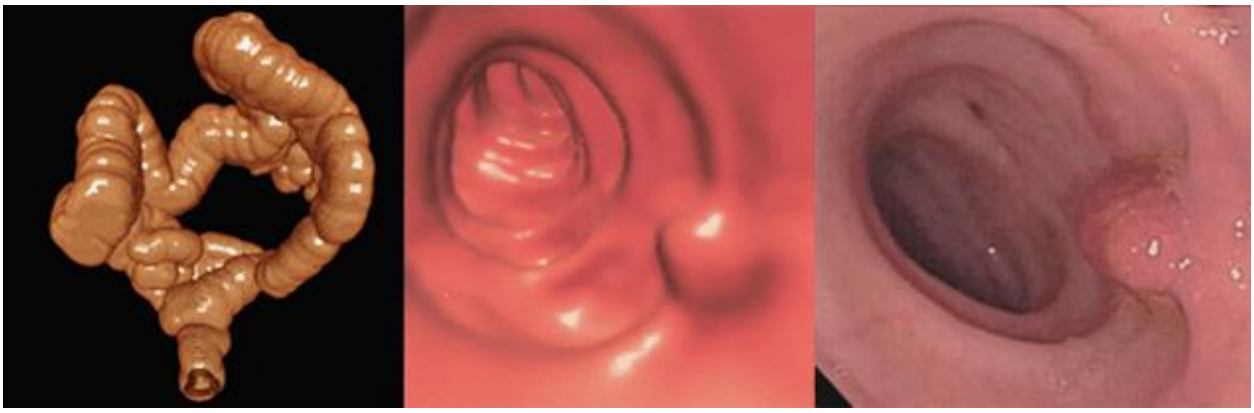

Figure 9. 3-D reconstructed colonography showing a growth protruding to the lumen of the colon. The image on the left represents a reconstructed CT of the whole colon from the exterior. The image in the middle represents a reconstructed CT showing the interior of the lumen. Image of the right represents a white light image of the same region shown by image in the middle.

Johnson et al. have demonstrated that polyps greater than 10 mm in diameter are identified by CTC experts with detection rates that range from 75% to 95%[28]. However, this detection sensitivity drastically drops when investigating flat lesions of the colon. In a study of 547 patients, Fidler et al. demonstrated that CTC detection sensitivities for all flat lesions and flat adenomas ranged from 65% and 100% to 15% and 13% amongst expert reviewers[29]. The drastic inter-observer variability in detection of flat lesions via CTC primarily arises from perception errors. Furthermore, reading CT colonographies requires a high level of expertise, making it difficult to substitute for white light colonoscopy as a gold standard.

1.3.5 Chromoendoscopy

In chromoendoscopy (CE), dye is sprayed onto the colonic mucosa using a catheter passed through the working channel of the endoscope. Used with dyes, a high resolution or high magnification endoscope, allows for detailed evaluation of the mucosal surface[9]. Inexpensive dyes such as methylene blue are used, and are absorbed by intestinal epithelium after local application. The result is a relatively stable staining pattern, which allows visualization of the openings of the glandular pits during chromoendoscopy[30,31]. In a study of 1000 patients undergoing routine colonoscopy, Rembacken et al. demonstrated that chromoendoscopy improved early diagnosis of adenomas and early colorectal cancers[32].

Kiesslich et al. performed a further systematic study to compare diagnoses *via* conventional white light endoscopy and chromoendoscopy in patients with a longstanding history of UC. They established that CE differentiated neoplastic from non-neoplastic changes with high specificity and sensitivity. CE using methylene blue demonstrated a three-fold increase in the number of detected intraepithelial neoplasias. Figures 10 and 11 excerpted from their study, demonstrate the ability of chromoendoscopy to help identify low-grade intraepithelial neoplasia and high-grade intraepithelial neoplasia respectively.

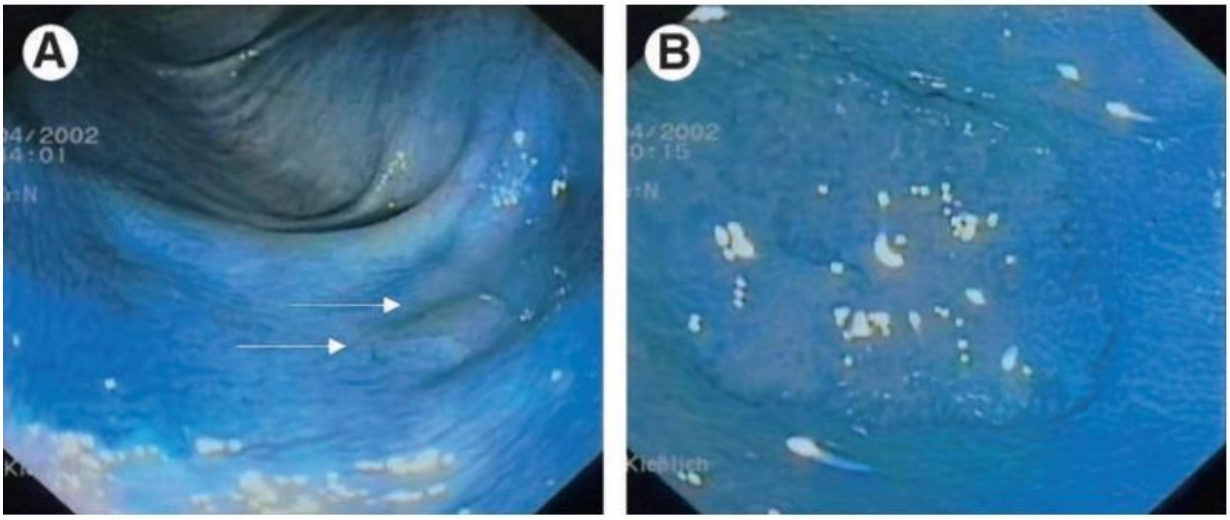

Figure 10. Low-grade intraepithelial neoplasia identified by chromoendoscopy[31]. Arrows in (a) identify the low-grade intraepithelial neoplasia that is further magnified in (b).

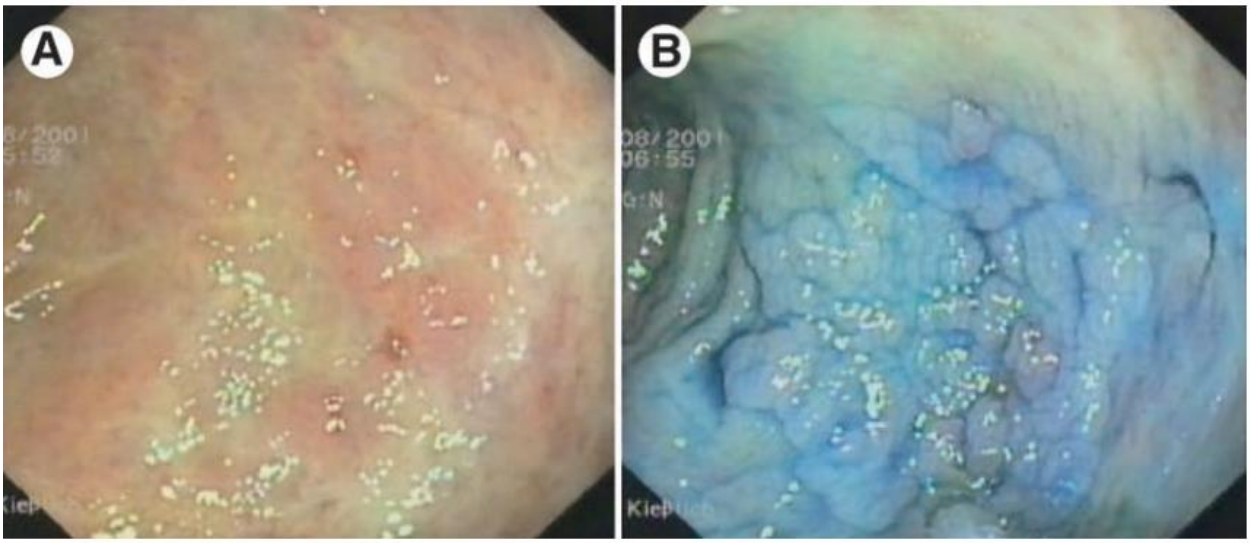

Figure 11. High-grade intraepithelial neoplasia identified by chromoendoscopy[31]

CE is often used in routine practice to identify low and high grade neoplasia. However, this technique does increase the procedure time by at least 33% and still requires very careful examination by the endoscopist. Furthermore, the contrast between low-grade intraepithelial neoplasia and the surrounding mucosa is very minimal. While it does help define pit patterns such as those present in high grade neoplasia, it cannot provide contrast between diseased and surrounding uninvolved regions for a quicker diagnosis and subsequent complete resection. To that end, there have been efforts in developing targeting molecular agents to specifically distinguish precancerous and cancerous lesions from surrounding uninvolved tissue.

1.3.6 Confocal Laser Endomicroscopy (CLE)

In confocal Laser endomicroscopy (CLE) is based on tissue illumination with low-power laser light pulses, and the entitled fluorescence from the tissue passes through a single mode optical fiber on the main optical axis between the objective lens and the detector. Both the illumination and collection systems are aligned in the same focal plane. The laser light is focused at a selected depth in the tissue of interest, and the fluorescence is refocused onto the detection system by the same lens. A high numerical aperture (NA) lens is used to illuminate and collect light to achieve subcellular resolution with maximum light collection. Only the refocused light through the fiber is detected while the remaining light, scattered at different geometric angles, is excluded from detection, which improves the spatial resolution of confocal endomicroscopy. Confocal endomicroscopy allows high resolution optical sectioning over a small field-of-view (FOV), and it can also be scaled down to millimeter dimensions. The size of the FOV is further constrained because the overall package must be less than 5 mm in diameter for endoscopic application. While

confocal imaging is possible based purely on tissue reflectance, confocal systems based on fluorescence arising from targeted contrast agents have been extensively developed.

In scanning fiber endoscopy (SFE), a single-mode optical fiber is driven by a tubular piezoelectric actuator to scan in a spiral pattern by tubular piezoelectric actuator in order to create an image with a large FOV. Red, green, and blue laser light (440, 532, and 635 nm wavelengths) is delivered through the scanning fiber and focused on to the tissue of interest by a multi-lens assembly at the distal tip of the probe. Both reflected and emitted fluorescent light are then collected by a ring of multimode optical fibers arranged along the outer edge of the instrument. This technology has been used in diagnosing cancer of the esophagus, pancreatic duct, and airways using reflected white light[33,34].

The SFE system has also been used to collect fluorescence in molecular imaging. Wang et al. have demonstrated the use of topically applied fluorescein dye on colonic mucosa to distinguish between normal mucosa, hyperplasia and adenoma[35]. Figure 12 shows the endomicroscopic probe, which fits into the instrument channel of a working endoscope, and shows the endoscope in use.

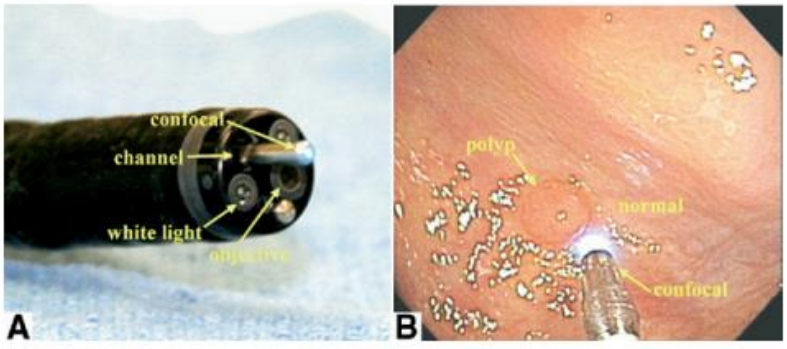

Figure 12. Probe based confocal laser endomicroscopy[35]

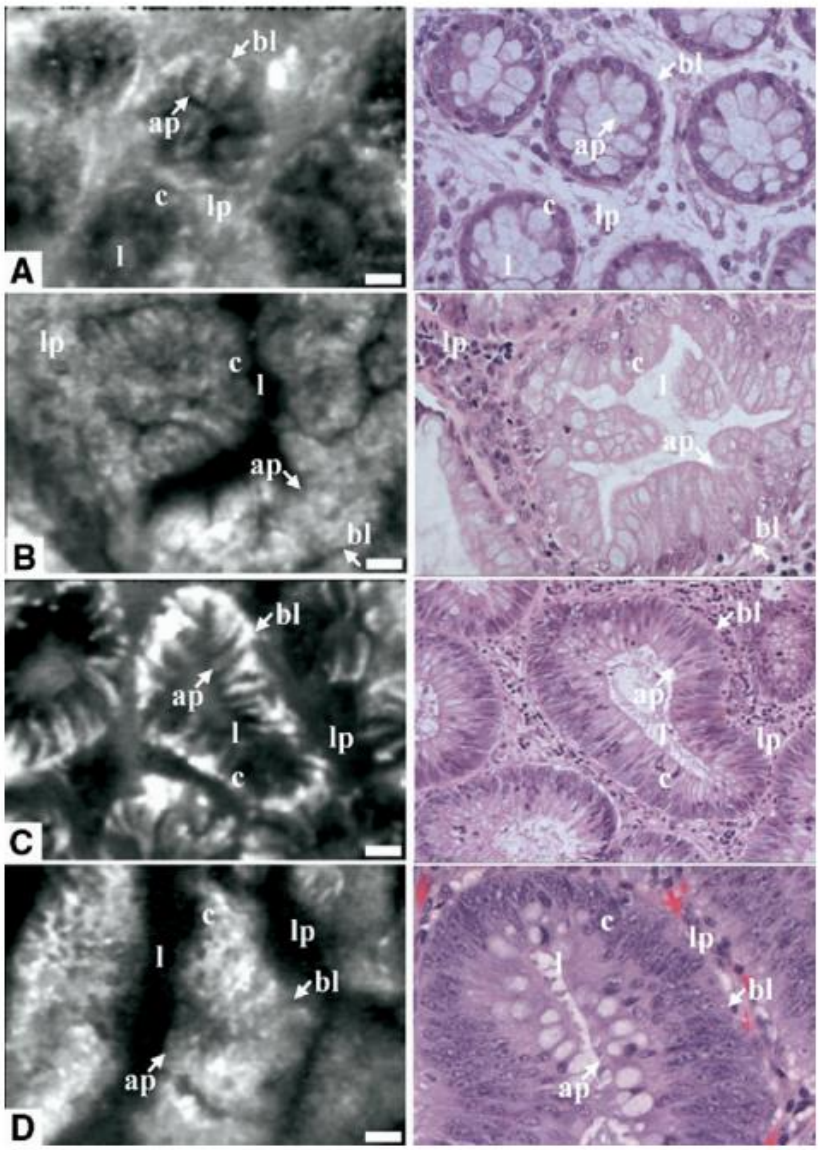

Figure 13. Colonic fluorescence distribution with corresponding H&E in (a) normal mucosa, (b) hyperplasia, (c) tubular adenoma, and (d) villous adenoma[35] Scale bar, 40 μm. The crypt lumens (L), apical (AP), and basolateral (BL) borders of epithelial cells (C), and lamina propria (LP) can be distinguished.

The fiber based endoscope is small and flexible enough to be used in existing scopes, and provide images that demonstrate a striking resemblance to histology when using a contrast agent such as fluorescein. Nevertheless, it is restricted to a working distance of 0 microns (direct contact), which limits its use in flat lesions, unless they have been already distinguished from their

surroundings. Furthermore, acquisition is time-intensive as the acquisition rate is as low as 0.8 frames per second.

1.4Targeted NIR Fluorescence Imaging

1.4.1 Fluorescence Imaging

Fluorescence imaging is known for its high detection sensitivity, specificity, and spatial resolution. It is based on the molecular absorption of light: a region of interest containing the fluorophore is excited at a specific wavelength, and light at a different wavelength is emitted. Each fluorophore has characteristic excitation spectrum that is identified by monitoring the fluorescence emission while the fluorophore is excited by a range of consecutive wavelengths. When electrons go from an excited state to the ground state, there is loss of vibrational energy. As shown in Figure 14, the emission spectrum is shifted to longer wavelengths than the excitation spectrum (a phenomenon known as Stoke's shift). The emission intensity peak is lower than the excitation peak. In order to achieve maximum fluorescence intensity, the flurophore is usually excited at the peak wavelength of the excitation curve, and the emission detection is typically the peak wavelength of the emission curve. The fluorescence method is regenerative, allowing longitudinal imaging, unlike the radionuclide decay process in nuclear imaging. Each fluorescence emitting molecule can be excited multiple times to produce almost the same fluorescence intensity, unless there are other diminishing factors, such as photobleaching, that could interfere with the process[36].[37]

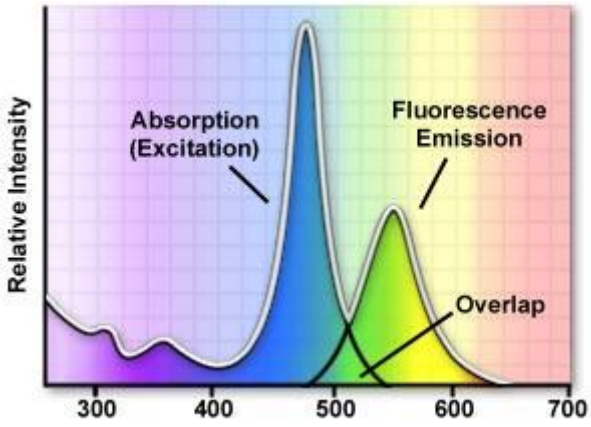

Fig 14. Excitation and Emission Spectra of a given flurophore

1.4.2 NIR Fluorescence Imaging

Fluorescence imaging can both use intrinsic tissue properties as a contrast (autofluorescence) and also can image exogenous contrast agents. The three primary processes that typically govern interaction of photons with tissues include light absorption, light scattering and fluorescence emission. Photons interact with tissues by absorption, scattering, and fluorescence emission. In short, light absorption and scattering decrease with increasing wavelength. Below 700 nm, tissue absorption results in low light penetration depth (a few millimeters), allowing only superficial assessment of tissues in the visible wavelength. The light absorption is caused by oxy- and deoxy-hemoglobin, by melanin at wavelengths <700 nm, and by lipid, and water at wavelengths >1000 nm[38,39]. Because the absorption coefficient of tissue is significantly lower in the near infrared (NIR) region (700-900 nm) than in the visible region, NIR light can penetrate more deeply into tissues, to depths of several centimeters[40,41]. A major goal of optical imaging has been the development of suitable targeted NIR fluorochromes with high molar extinction coefficients, good quantum yields, and specific tissue binding.

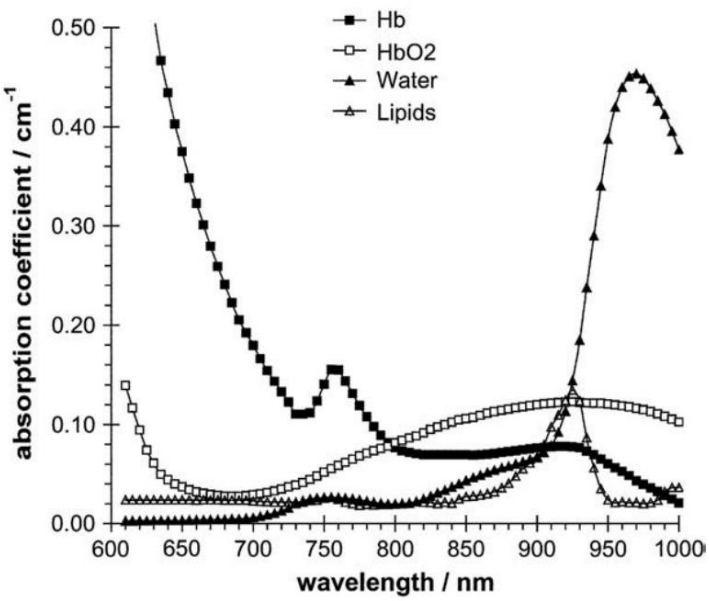

Figure 15. Tissue constituents absorbing in the 600 – 1000 nm range[42]

Due to the minimal NIR fluorescence contrast generated by most tissues, most *in vivo* studies require exogenous contrast agents. One important class of organic flurophores, hetamethine cyanines, comprised the benzoxazole, bezothiazole, idolyl, 2-quinoline and 4-quinoline subclasses. Indocyanines are the most widely used among these as they are free from aggregation problems associated with the other subclasses. The excitation peak of this class lies between 760-800 nm, and emission peak is between 790-830 nm[43]. Indocyanine green (ICG), one of the most common examples of indocyanine class, was approved by FDA for in-human use in 1958. It is one of the least toxic agents administered to humans, with the only adverse reaction being rare anaphylaxis. Furthermore, ICG is tetra-sulfonated, increasing its solubility and aqueous quantum yield (QY)[39].

In vivo imaging requires that the contrast agent be delivered to the target, have adequate contact time with the target for the binding to occur, and be retained by the target while non-bound

material is cleared. Unconjugated organic NIR flurophores are typically less than 1.2 kDa but have widely different bio-distributions and pharmacokinetics, depending on their charge and the properties of their conjugated targeted molecule. As the charge per molecule is increased, fluorophores remain extracellular and their plasma half-life increases proportionally[44]. Clearance is typically accomplished by a combination of renal filtration and excretion into bile.

Another important consideration for *in vivo* molecular probes is toxicity. Without charged groups, indocyanines can be quite toxic due to intracellular accumulation[45]. However, di-sulfonated ICG has been used in humans over 50 years and has an excellent safety profile. ICG has been used in a variety of applications, including angiograms of the eye[46,47], brain post-tumor resection margin determination [48,49], and GI tract lesion identification to name a few. Although ICG provides a contrast mechanism, its enhanced permeability and retention (EPR) create limitations. Studies utilizing ICG to detect colorectal tumors have demonstrated high background intensity in the subserosa around the tumor, resulting in unnecessary follow-up procedures [50]. For this reason, interest in developing tumor-specific optical contrast agents has been rapidly growing.

1.4.3 Targeted Molecular Imaging

Targeted molecular agents consist of a signal component and a targeting component. To recognize specific pathological tissues, a mass of targeting component, such as a small molecule, peptide, antibody, or aptamer is applied to ligand-directed imaging agents.

Small molecules are defined by a size <500 Da. Due to their small size, they can be applied to intracellular imaging and even to central nervous system imaging, crossing the blood/brain barrier. A common targeted small molecule, ^{18}F-FDG, has been clinically applied to a wide variety

of cancer imaging[51]. Other examples include, but are not limited to, the use of gadolinium (Gd) targeting human tumor telomerase reverse transcriptase (hTERT) for detection of telomerase positive carcinomas using magnetic resonance imaging[52].

Peptide, a widely used class of ligands for molecular imaging, offer superior selectivity and specificity and easy modification without changing their binding properties or distribution. Furthermore, peptides have higher stability and lower immunogenicity than antibodies, making them more desirable for imaging. Achilefu et al. conjugated of GRD-based peptide to a NIR fluorophore, cypate, for imaging A549 tumor-bearing mice, with the results shown in Figure 16[53]. The versatility of peptides in various modalities is evident from their use in micro-PET imaging as well. Hackel et al. employed ^{18}F labeled 2 cysteine knot to detect BxPc3 pancreatic adenocarcinoma tumors in mice, using micro-PET with high tumor uptake and demonstrating promise for cancer imaging[54].

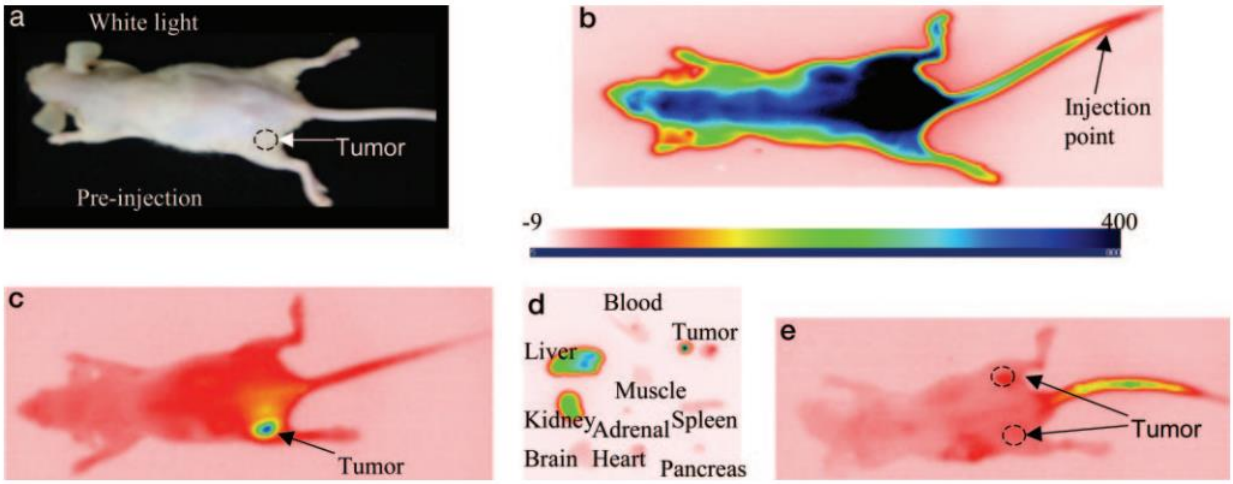

Figure 16. *In vivo* distribution of Cyp-GRD in A549 tumor-bearing mice[53]. A) White light image of mouse highlighting tumor prior to injection of probe. B) Post-injection, 0 hr image. C) 24 hour

post administration image. D) Biodistribution study post sacrifice. E) Blocking study demonstrating absence of binding in tumors.

Antibodies are characterized by their ability to bind to targets due to their high affinity and specificity and their easy synthesis. Thus far, there have been more antibody-based targeting moieties cleared by the FDA than any other type; with eight FDA approved radiolabeled antibodies for SPECT imaging and 20 antibodies approved for therapy. For example, Zhang et al. used PET with ^{64}Cu-NOTA-TRC105-Fab to image CD105 expression. Figure 17 showed clear uptake in 4T1 luc tumors[55].

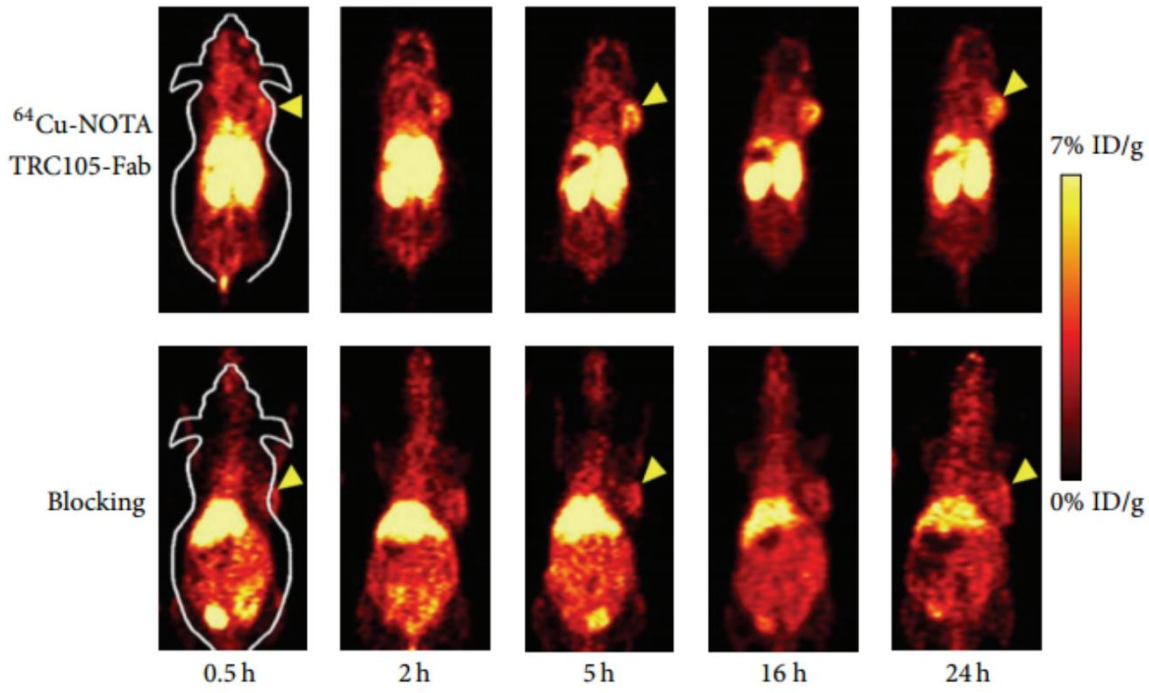

Figure 17. PET images of ^{64}Cu-NOTA-TRC105-Fab after treatment with blocking dose of TRC105 before injection.[55] Arrow marks the location of the tumor. The tumor is identified using the probe as opposed to when it is blocked having saturated the target site. Liver shows maximum signal uptake.

Molecular imaging enables both dynamic and quantitative visualization of specific biochemical processes. It has demonstrated its impact on early stage diagnosis, curative effect monitoring of diseases, drug development, gene therapy, and other fields. Its limitations stem from a dearth of multifunctional molecular imaging agents, the limitations of imaging technology (such as poor sensitivity to complement contrast agents), and the lack of non-radiative molecular imaging that can provide both structural and functional information. Although multi-modality imaging systems such as PET/MRI have clear advantages in sensitivity and specificity, they are more costly than single modality imaging, their performance is not markedly better, and they suffer from multimodal contrast agent fusion[56].

1.5 Polarization Imaging: Concepts and Application in vivo Imaging

While molecular imaging can report molecular-sensitive biochemical processes, it still requires a modality capable of providing structural information. Efforts have come in the form of color-fluorescence endoscopy, PET-CT, and even fluorescence-based confocal endomicroscopy (CLE). However, such dual-modal approaches have limitations in detection of flat lesions in CAC. Color-fluorescence imaging lacks a targeting probe that can detect both precancerous and cancerous lesions with high specificity and sensitivity and provide a high signal-to-background ratio (SBR). PET-CT is far too large to fit within an endoscope. Fluorescence CLE requires further development to provide a greater working distance and acquisition rate in an endoscopic setting. To address this, we have explored the potential of utilizing polarization-sensitive information to provide supplementary structural information about the f tissue of interest in endoscopy. Polarization imaging offers an additional contrast mechanism because it allows for discrimination against

multiply scattered light, enabling higher resolution imaging of tissues and their underlying structures. It provides a method for non-invasive and quantitative tissue diagnosis since the polarimetric characteristics of tissues can encode a large amount of biochemical, morphological, and functional information[57].

1.5.1 Fundamentals of Polarization Imaging

Polarization is a consequence of the electromagnetic (EM) wave nature of light, in which the transverse oscillations of the electric and magnetic field vectors ($\bar{E}$ and B) trace out stationary curves. If the electric and magnetic vectors instead followed random paths in their temporal evolution, the resulting light would be said to be unpolarized. The shape of the function traced out by the vectors would be defined as the polarization state of the beam.

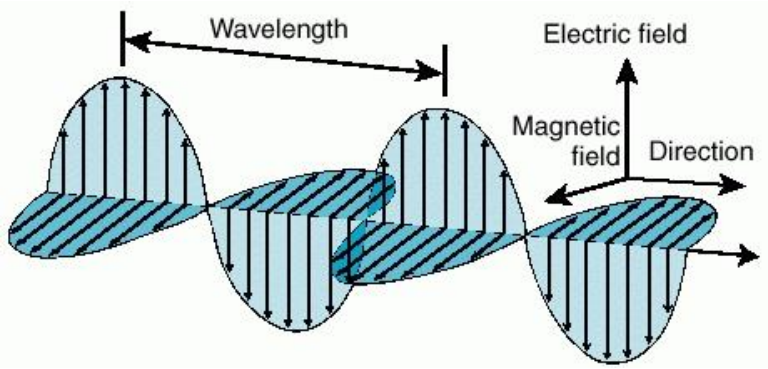

Figure 18. Electromagnetic Wave

When the electric field vector $\bar{E}$ of an EM wave is confined to a plane, the resulting light is said known to be linearly polarized, and when it traces out a helix normal to the direction of the wave's propagation, the resulting beam is known to be circularly polarized. When considering a

large number of photons, their collective behavior is consistent with the classical limit (wave solution to Maxwell's equations), and in the case when all the photons in a beam of light exhibit the same polarization, the light is said to be fully polarized. In the case of photons possessing different polarizations but with a distribution favoring one particular state, the light is considered partially polarized. Lastly, when the photons are uniformly distributed over all polarization states the light is said to be unpolarized. The degree of polarization (DOP) emerges as a very useful quantification in this case, where it measures the uniformity, or lack thereof. The DOP of fully polarized light is 1, and that of unpolarized light is 0. Depending on the magnitude of the relative surplus of a particular polarization state, a partially polarized beam of light can fall somewhere between the fully polarized and unpolarized light states. Usually, two mathematical formulations describe the polarization state: the Jones calculus and Stokes-Mueller calculus. While the Jones calculus is a field-based model which assumes coherent addition of phase and amplitude of EM waves, Stokes-Mueller calculus is an intensity-based model which utilizes incoherent addition of intensities. That said, the Jones calculus method is limited: It can describe pure polarization states, but in biological imaging cases where partially polarized states need to be addressed, it is ill suited. Stokes-Mueller formalism, on the other hand, can fully describe polarized light and its interaction with materials, thus suiting biomedical polarimetry.

1.5.2 The Stokes-Mueller formalism

Polarization states are described by four measurable quantities, known as Stokes parameters and denoted I, Q, U, and V relative to six different intensity measurements, each corresponding to the intensity of the beam in question after it has passed through various ideal polarizers. I_H is the intensity through a horizontal linear polarizer, I_V through a vertical linear

polarizer, I_P and I_M through linear polarizers at 45^0 and 135^0, and I_R and I_L through right and left circular polarizers, respectively. Combining I, Q, U, and V forms a four-dimensional vector, known as the Stokes vector:

$$S = \begin{bmatrix} I \\ Q \\ U \\ V \end{bmatrix} = \begin{bmatrix} I_H + I_V \\ I_H - I_V \\ I_P - I_M \\ I_R - I_L \end{bmatrix} \quad (1)$$

Here, I represents the total intensity of light, Q and U represent the degree and orientation of linear polarization, and V represents the degree and direction of circular polarization. The Stokes parameters are related by

$$I^2 \geq Q^2 + U^2 + V^2 \quad (2)$$

The equality holds in the case of full polarization, and the inequality holds in the case of partial polarization. Therefore, DOP is defined by

$$DOP = \frac{\sqrt{Q^2 + U^2 + V^2}}{I} \quad (3)$$

In the case of an unpolarized beam (DOP = 0), we have Q = V + U = 0. Therefore, the degree of linear polarization (DOLP) is defined by

$$DOLP = \frac{\sqrt{Q^2 + U^2}}{I} \quad (4)$$

.

When light that is described by the Stokes vector S_{in} interacts with a material, its polarization state is usually modified, and the resulting light can be described by the Stokes vector S_{out}. The resultant transfer function between the input and output polarization states can be given by

$$S_{out} = MS_{in} \tag{5}$$

Here M is a 4 x 4 matrix known as the Mueller matrix. Expanding the equation above into its components results in

$$\begin{bmatrix} I_{out} \\ Q_{out} \\ U_{out} \\ V_{out} \end{bmatrix} = \begin{bmatrix} M_{1,1} & M_{1,2} & M_{1,3} & M_{1,4} \\ M_{2,1} & M_{2,2} & M_{2,3} & M_{2,4} \\ M_{3,1} & M_{3,2} & M_{3,3} & M_{3,4} \\ M_{4,1} & M_{4,2} & M_{4,3} & M_{4,4} \end{bmatrix} \begin{bmatrix} I_{in} \\ Q_{in} \\ U_{in} \\ V_{in} \end{bmatrix} \tag{6}$$

Given that Mueller matrices provide a complete description of a wide range of physical materials, and that their elements are associated with various intensities, they can be experimentally determined with ease by using conventional intensity-measuring instruments such as polarimeters.

1.5.3 Polarimeteric characteristics

The three principle characteristics that can be encoded by a Mueller matrix include depolarization, diattenuation, and retardance. In biomedical applications such as tissue imaging and characterization, there is a strong need to measure signals that retain their original polarization. Biological tissues are strongly depolarizing by multiple scattering and/or birefringence domains of varying magnitude and orientation, depolarized noise that can inhibit detection of remaining weak remaining information-carrying polarization signals.

1.5.3.1 Depolarization

If the DOP of incident light is *m* (between 0 and 1), and the light resulting from interaction with the sample has a DOP of *n*, where (m > n), then the sample is said to be depolarizing. For incident beam polarized light *m*;

$$m = \frac{\sqrt{{Q_{in}}^2 + {U_{in}}^2 + {V_{in}}^2}}{I} \tag{7}$$

The DOP of the resultant light would be defined as:

$$n = \frac{\sqrt{{Q_{out}}^2 + {U_{out}}^2 + {V_{out}}^2}}{\mathrm{I}} = \frac{\sqrt{(aQ_{in})^2 + (bU_{in})^2 + (cV_{in})^2}}{I} \tag{8}$$

Here $|a|, |b|, |c| \leq 1$. In matrix form, this relation can be given as

$$M_\Delta = \begin{bmatrix} 1 & 0 & 0 & 0 \\ 0 & a & 0 & 0 \\ 0 & 0 & b & 0 \\ 0 & 0 & 0 & c \end{bmatrix} \quad |a|, |b|, |c| \leq 1 \tag{9}$$

Thus 1- $|a|$ and 1 -$|b|$ are linear depolarization factors, and 1 - $|c|$ is the circular depolarization factor. The net depolarization, given by delta, is defined as

$$\Delta = 1 - \frac{|a| + |b| + |c|}{3} = 1 - \frac{|T_r\,(M_\Delta - 1)|}{3} \tag{10}$$

In biomedical applications, the dominant processes causing depolarization are multiple scattering and spatially heterogeneous arrangements of uniaxial birefringent domains. A larger delta implies a lower degree of polarization of light after interaction with a medium.

Diattenuation and retardance are both the result of differences in refractive indices for different polarization states, and they are usually described in terms of the ordinary and

extraordinary axis and indices. Differences in the real parts of indices result in linear and circular birefringence (retardance), whereas differences in imaginary parts can cause linear and circular dichroism (diattenuation). Diattenuation is a measure of the differential attenuation of orthogonal polarization states for linear and circular polarization. Therefore, linear diattenuation can be described as differential attenuation of two orthogonal linear polarization states, and circular diattenuation is the difference between the right and left circular polarization states.

Although biological tissues are not easily amenable to polarimetric investigation due to the extensive polarization loss caused by multiple scattering and by spatially-varying birefringence, it is possible to reliably detect surviving polarization states after fully polarized light is shined on the tissue. Several issues remain, including how to reliably measure and characterize the surviving fraction, how to interpret the measured polarization signals, and how the signal for real-time polarization sensing in an *in vivo* setting. We have made significant efforts on that front, while combining the resulting information with other functional level information via targeted NIR fluorescence.

1.6 Our Approach

In order to address the poor miss rates of flat lesions, we have developed a four-step approach: (1) Identifying and characterizing a targeted molecular probe capable of identifying precancerous and cancerous lesions in CAC, (2) Exploring administration routes for the molecular probe in clinically relevant murine models, (3) Developing the supporting instrumentation for a color-fluorescence-polarization endoscope, (4) Demonstrating the probe and endoscope in diagnosis and

validation post-biopsy of SCC and CAC (5) Expanding the scope of the platform to include other disease models.

1.6.1 Choice of Molecular Probe for Colorectal Cancer detection

A targeted, NIR probe termed LS301 was reported previously[58]. The probe is composed of a NIR fluorescent dye, cypate (780_{ex}/ 830_{em}), and a cyclic peptide sequence, D-Cys-Gly-Arg-Asp-Ser-Pro-Cys-Lys (c($_{D}$CGRDSPC)K). Figure 19 shows the molecular structure, absorption, and emission spectra of LS301. The versatility of this molecular probe in detecting precancerous and cancerous lesions in a variety of cancers has been demonstrated for lung cancer cells A549[53], the mammary tumor cell line 4T1 luc, colorectal cancer cell line HT-29, and even pancreatic cancer in murine models. Figure 20 demonstrates its efficacy in 4T1luc tumor bearing mice transfected with luciferase for bioluminescence imaging, in comparison to NIR fluorescence.

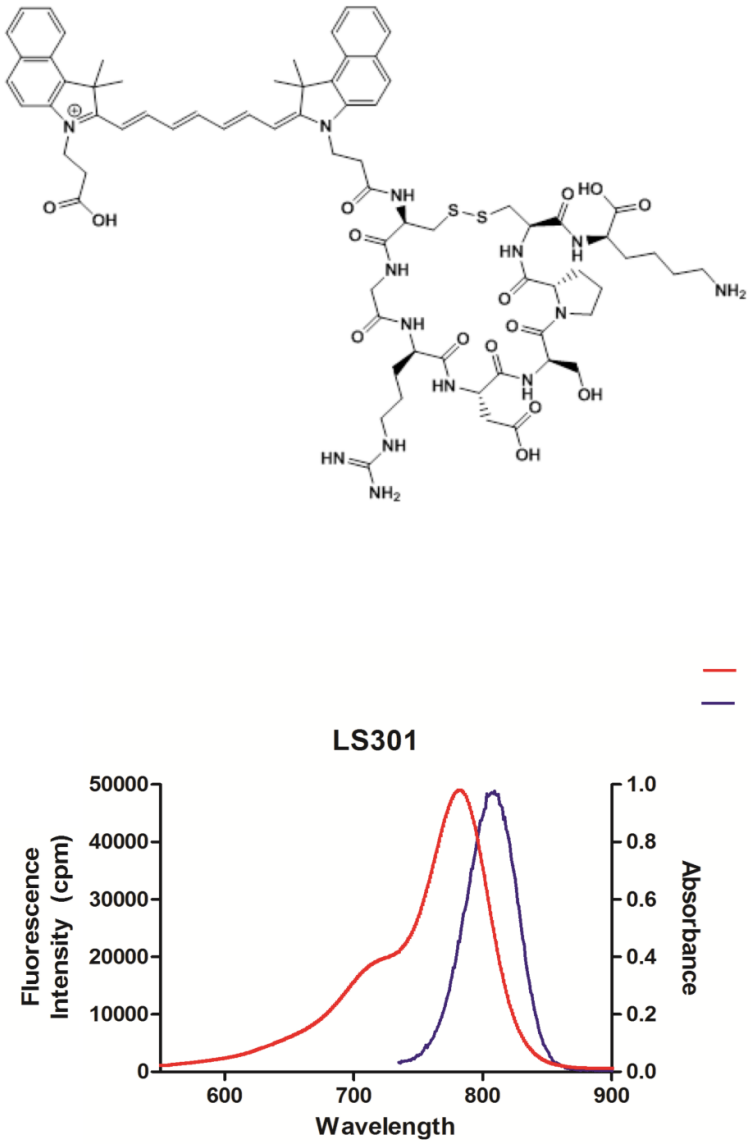

Figure 19. Molecular Structure and excitation/emission characteristics of NIR fluorescence targeted LS301

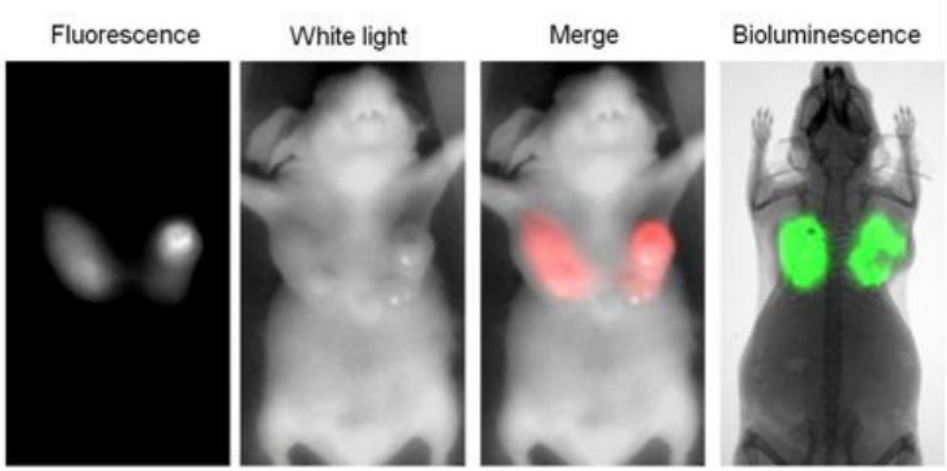

Figure 20. Targeted molecular probe LS301 for tumor imaging in 4T1luc tumor-bearing mice

We first employed LS301 on murine colorectal cancer tissue sections derived from various stages in and tested its binding preferences. Figures 21 and 22 demonstrate the performance of LS301 with various stages (cancerous and dysplastic, respectively) of CAC in an azoxymethane-dextran sodium sulfate (AOM-DSS) model. AOM-DSS model has been used to demonstrate that advanced cancers develop from flat lesions without transitioning through a polypoid intermediate.[59] H&E staining and corresponding NIR fluorescence are presented for adenomatous tumor (Figure 21) as well as dysplastic tissue (Figure 22). A preferential uptake of LS301 is observed in these abnormalities when compared to surrounding uninvolved tissue.

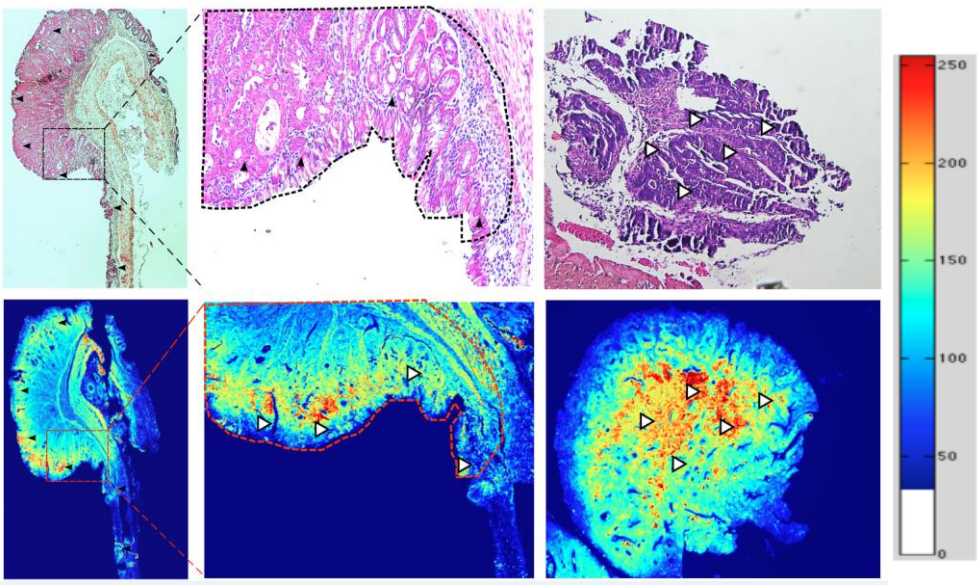

Figure 21. Binding preference of LS301 for an advanced cancerous stage in AOM-DSS model (recapitulates CAC). Arrows are shown to help visualize corresponding regions in H&E and NIR fluorescence images.

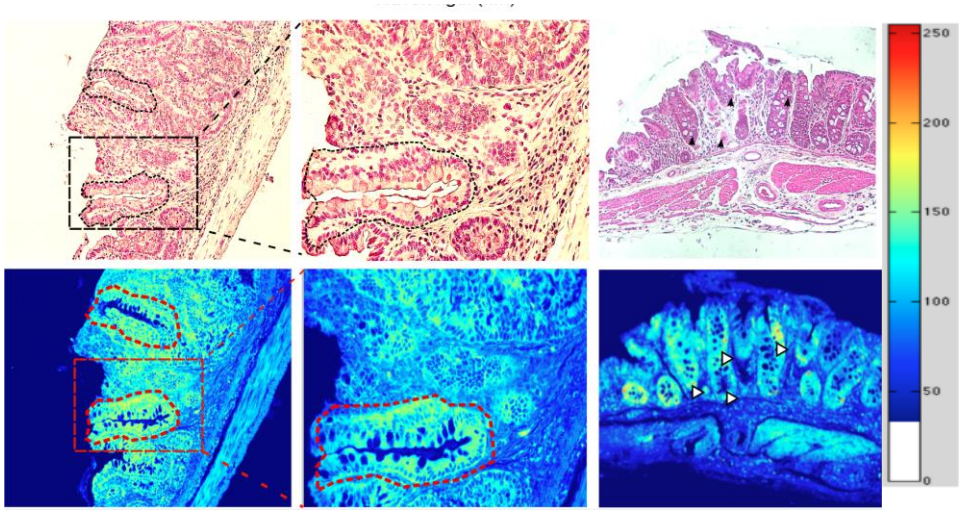

Figure 21. Binding preference of LS301 for a dysplastic stage in the AOM-DSS model (recapitulates CAC). Arrows are shown to help visualize corresponding regions in H&E and NIR fluorescence images.

To compare the specificity of our molecular probe for multiple stages of tumorigenesis with existing peptide based probes, we conjugated the VRPMPLQ sequence, identified by Contag et al. for its preferential binding to colonic dysplastic tissues, to cypate for binding studies[60]. This conjugated molecular probe was termed LS656. The molecular structure, along with the absorbance and emission spectra for LS656 and LS301, is presented in Figure 22. Consistent with the findings of Contag et al., LS656 demonstrated high specificity for precancerous lesions that exhibited features, such as aberrant crypt foci (Figure 22g, 22h). LS301 exhibited a very similar binding pattern, to that of LS656 producing higher fluorescence intensity at the aberrant crypt foci (Figure 22f). The molecular probes were topically administered at a 1uM concentration in a phosphate buffered saline (PBS) solution. LS301 (Figure 22c) exhibited a five-fold higher fluorescence intensity than LS656 (Figure 22d), demonstrating its potential as a diagnostic tool for multiple stages of tumorigenesis in colorectal cancer.

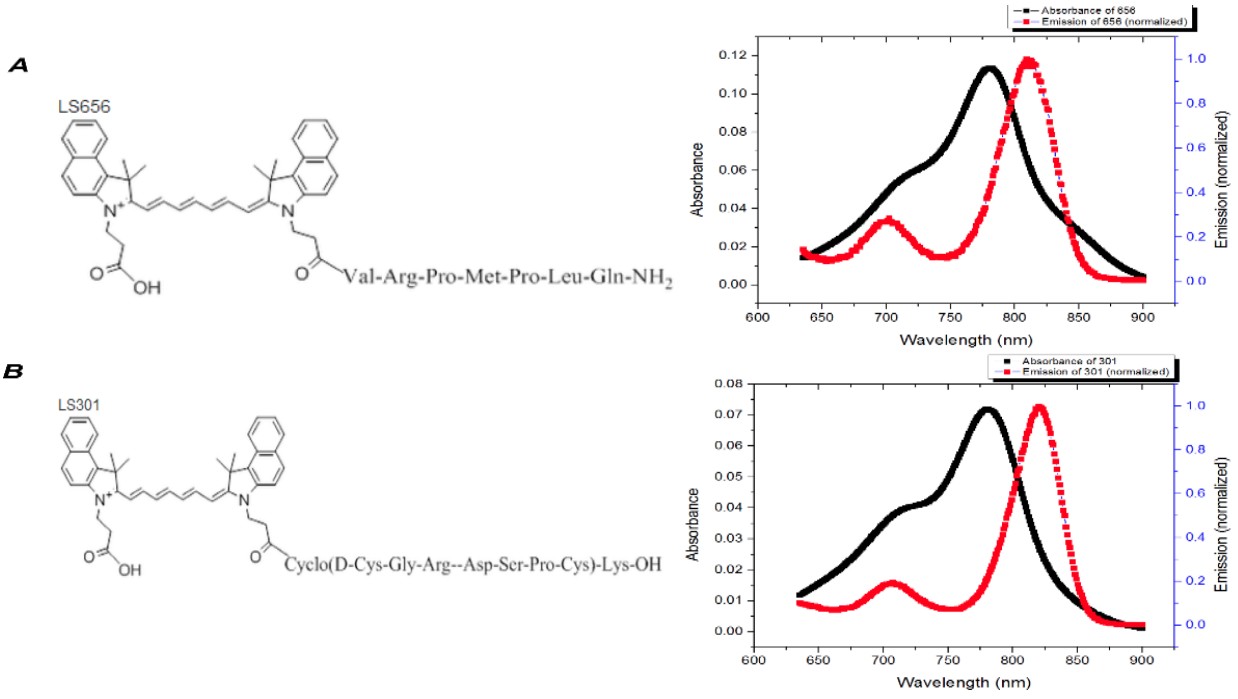

Figure 22. Comparison of binding preferences of LS301 and LS656 in an AOM-DSS model. (A) Molecular structure and emission spectra of LS656 and (B) LS301.

We demonstrated the use of LS301 in a murine sporadic colorectal cancer model as well as a spontaneous one (APC min). The sporadic colorectal cancer model was developed by using a human colon cancer patient-derived cell line (HT-29) and orthotopically implanting it in the cecal wall using a protocol that has been established before.[61] We demonstrated the efficacy of the molecular probe over time and investigated its binding preferences at an optimal time point, *in vivo* and ex vivo after exteriorizing the organs and sectioning the tissues. Furthermore, we compared the binding preferences of the molecular probe with established proliferation marker, Bromodeoxyuridine. This work has resulted in a manuscript, details of which can be found in Chapter 2 of this dissertation.

1.6.2 Administration routes for LS301

Having demonstrated the specificity of LS301 for both precancerous dysplastic lesions in colon tissue and cancerous tissue, we then explored the administration routes for LS301 for *in vivo* diagnosis of CAC. Current clinical practice for routine endoscopy requires the patient to be on a strict liquid diet one-three days prior to the procedure. Furthermore, they are sometimes even subjected to a barium enema solution to empty their bowel. The use of absorptive stains, such as methylene blue, during colonoscopy procedures has become an increasingly more standard practice to improve visualization during the procedure. These stains have been shown to identify specific epithelial cell types by preferential absorption or diffusion across the cell membrane. Contrast stains, such as indigo carmine, seep through mucosal crevices and highlight surface topography and mucosal irregularities. While these stains aid in visual identification of pit patterns, they are not specific towards precancerous and cancerous lesions. The additional time required for chromoendoscopy varies dramatically depending on the technique used and operator experience as it involves a brief incubation period of up to ten minutes on average[62].

Other administration routes that are also utilized in abdominal imaging include - but are not limited to - intravenous or oral administration. All three administration routes have been explored for LS301 and discussed in further detail in Chapter 3.

1.6.3 Developing the supporting instrumentation for color-fluorescence-polarization endoscope

To improve detection sensitivity for flat lesions in colorectal cancer, newer fluorescence endoscopic techniques, such as confocal laser endomicroscopy, have been developed. In conjunction with fluorescence contrast agents, these techniques allow visualization of molecular signatures of cancer, but they lack real-time validation strategy and provide only a limited field of view.[60,63,64]Although fluorescence endoscopy is a well-established method with targeted fluorescence imaging gaining more traction in CLE setting, to the best of our knowledge, this has been the first demonstration of a combined color-fluorescence-polarization endoscopy in vivo. Polarization imaging generally requires the use of complicated setups and multiple measurements, making its use in biomedical applications difficult.

Herein, we report a novel polarization sensor developed by the Gruev group at Washington University. A nanowire polarization filter was fabricated in close collaboration with Moxtek Inc. First, a 70 nm thin film of aluminum was deposited on doped Si substrate, followed by a 30 nm film deposition of SiO_2 by e-beam evaporation. A 100 nm thin layer of photoresist S-1805 was spin coated at 3000 rpm and baked at 115^{o}C for 60 seconds. A continuous-wave 532 nm Nd:YAQ laser was used with frequency-doubler to produce coherent light waves at 266 nm. Two continuous 266 nm waves were aligned to interfere at 110 degrees and produce an interference pattern with a

period of 140 nm. The interference pattern was transferred to the photoresist by exposing the sample for 40 seconds. After the photoresist was developed, the pattern was transferred to the SiO_2 using the standard RIE/ICP etching procedure for SiO_2. The SiO_2 is used as a hard mask for etching the aluminum. The aluminum was etched for 150 seconds using 30 sccm BCl_3, 15 sccm Cl_2, 10 mTorr pressure, 70^o C temperature, 100 W RIE power and 150W ICP power. The procedure was repeated four times and the sample was rotated by 45^o each time in order to produce nanowires with four different orientations[65].

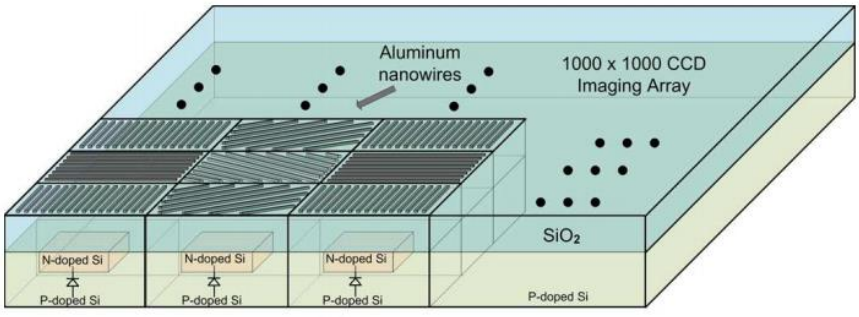

Figure 23. Block diagram of integrated CCD polarization imaging sensor[65]

Furthermore, we combined the polarization sensor and NIR-fluorescence-sensitive sensor that has the ability to also capture color images into endoscopic setup. This setup would allow the user to switch between polarization and fluorescence-color modes by simply switching light source and camera. Figure 24 demonstrates the setup of the endoscope that allows us to take color, fluorescence and polarization sensitive images of a given region of interest in the colon of murine models. The setup is fixed on a tripod to minimize movements when switching between fluorescence and polarization modes, and has been discussed in greater detail in Chapter 4 and in published manuscript[66].

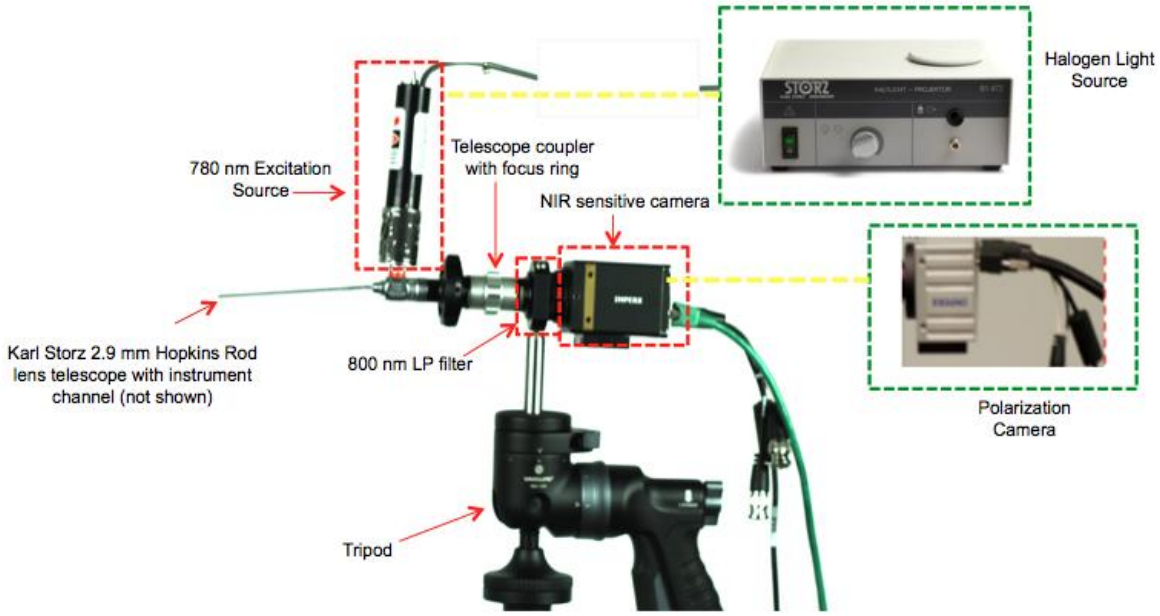

Figure 24. A color-fluorescence-polarization imaging setup for murine endoscopy

1.6.4 Demonstrating use in colitis-associated cancer, sporadic colorectal cancer for diagnosis and validation post-biopsy

Dysplasia in the colon in IBD and CAC develops as a result of repeated cycles of epithelial cell injury and repair while cells are bathed in chronic inflammatory cytokine enviornment[67]. While both, spontaneous and colitis-associated cancers share the adenocarcinoma consequence, the sequence of underlying molecular events differs, as discussed earlier. The azoxymethane-dextran sodium sulfate (AOM-DSS) model fills this void. Dextran sodium sulfate (DSS) is an agent that has direct toxic effects on colonic epithelium and can be administered in drinking water to mice in multiple cycles to create a chronic inflammatory state[68]. Tumor development can be hastened in this model if it is administered in a pro-carcinogenic setting such as using azoxymethane (AOM), a tumor-inducing agent. The AOM-

DSS model has been widely appreciated for its reproducibility, potency, and ease of use. Figure 25 demonstrates the outcome of this model 72 days post AOM-DSS treatment[69].

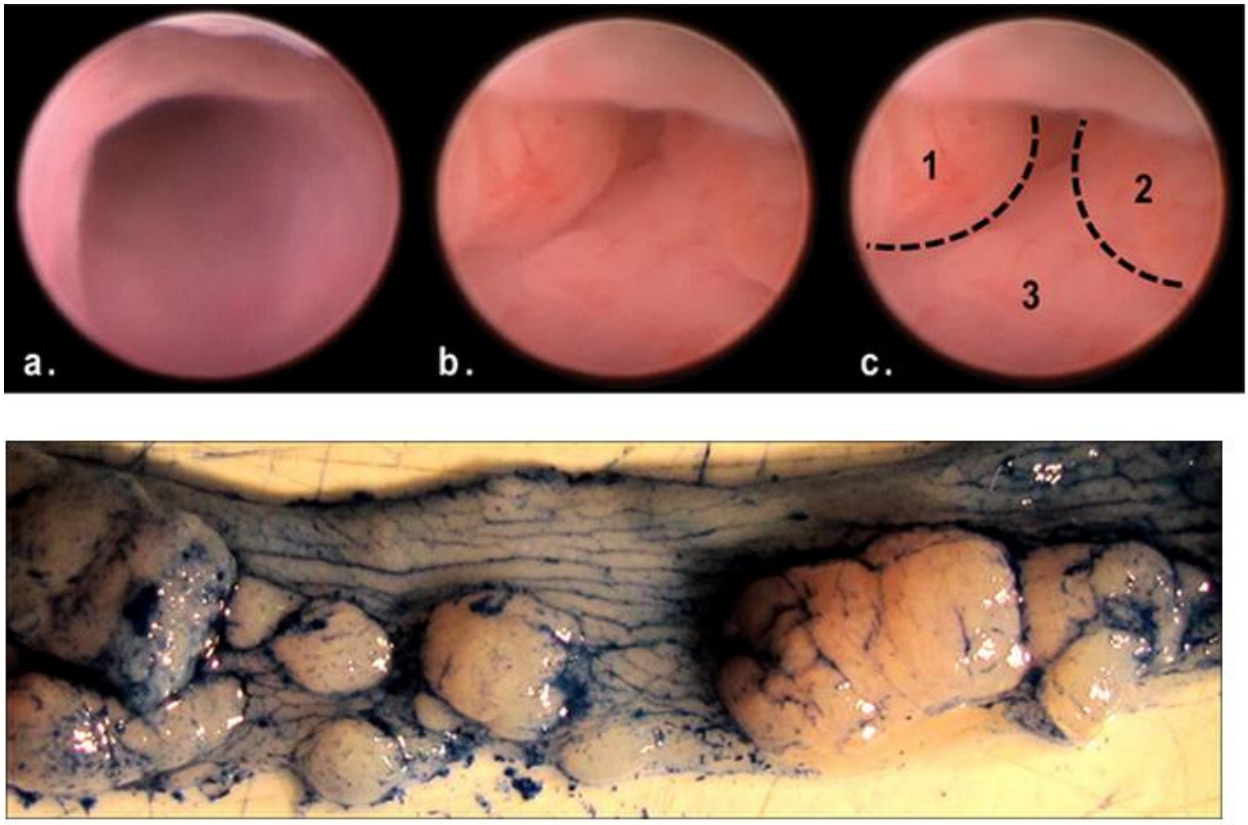

Figure 25. Use of AOM-DSS protocol in formation of adenocarcinoma along the distal and proximal colon. (a) normal colon, (b-c) adenomatous tumor highlighted as regions 1 ad 2. *Ex vivo* methylene blue staining staining of the dissected distal colon.

We demonstrated the color-fluorescence-polarization endoscope in the CAC model and further extended the application towards microscopy to fill the void between fluorescence-polarization-guided biopsy and H&E staining for validation. Currently, post-biopsy, the tissues get processed and stained with hematoxylin and screened by pathologists to ensure complete resection. In the case of incomplete resection, the patient is called upon again for a repeat surgery, thereby increasing hospitalization time, raising chances of complications arising from a second surgery, and increasing healthcare costs. We have developed a fluorescence-

polarization microscopy method (see Figure 26 for instrumentation setup) utilizing circular polarized light to quickly differentiate tumor margins from surrounding uninvolved regions such as muscle and subserosa in HT-29 xenograft colorectal cancer tumors implanted in mice. This has further been discussed in Chapter 4.

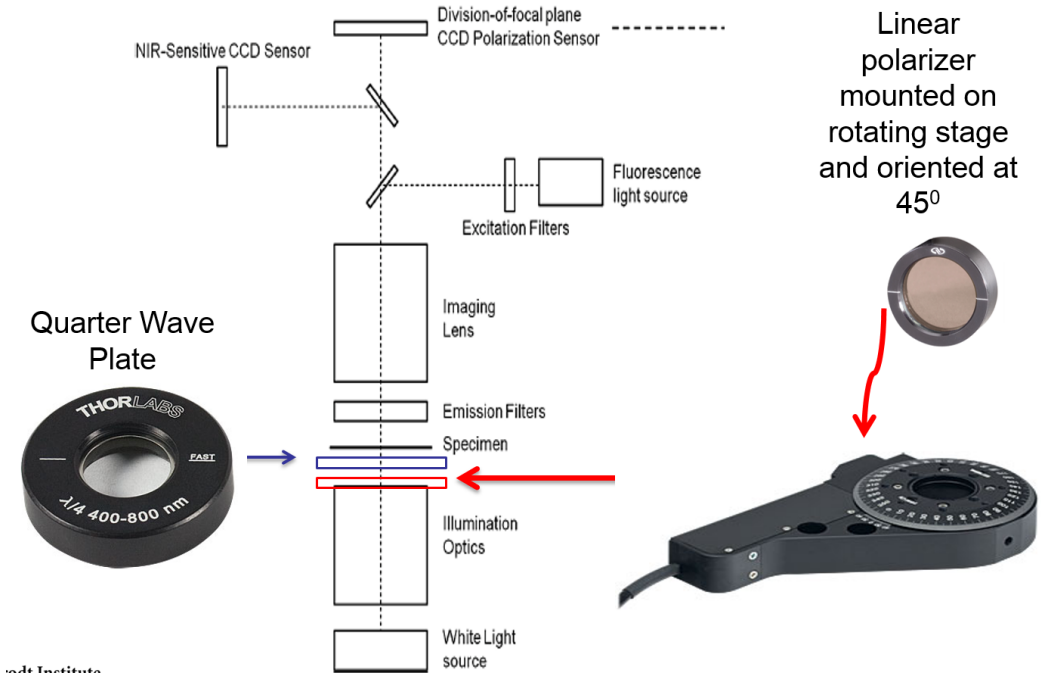

Figure 26. Optical setup for circular polarized light polarization-fluorescence microscopy in HT-29 post-biopsy tissue assessment

1.6.5 Expansion of targeted NIR Fluorescence probe towards other epithelial-based disease models

Lastly, we expanded the scope of our study to investigate use of targeted-NIR fluorescence probe towards early detection of pancreatic cancer. We further developed a platform for: (1) non-invasive fluorescence imaging using fluorescence molecular tomography (FMT) to

differentiate pancreatitis from pancreatic cancer followed by a (2) guided NIR-fluorescence laparoscopy procedure to ensure complete tumor resection. Also, we performed flow cytometry to further understand the binding characteristics of the molecular probe and conducted immunohistochemistry to compare binding preferences with existing probes for pancreatic cancer. Work on this front has resulted in a manuscript that is described in greater detail in Chapter 5.

References

1. Siegel, R., Ma, J., Zou, Z. & Jemal, A. Cancer statistics, 2014. *CA: a cancer journal for clinicians* **64**, 9-29 (2014).
2. Siegel, R., Desantis, C. & Jemal, A. Colorectal cancer statistics, 2014. *CA: a cancer journal for clinicians* **64**, 104-117 (2014).
3. Molodecky, N.A*., et al.* Increasing incidence and prevalence of the inflammatory bowel diseases with time, based on systematic review. *Gastroenterology* **142**, 46-54 e42; quiz e30 (2012).
4. Markowitz, S.D. & Bertagnolli, M.M. Molecular origins of cancer: Molecular basis of colorectal cancer. *The New England journal of medicine* **361**, 2449-2460 (2009).
5. Oshima, H., Oshima, M., Kobayashi, M., Tsutsumi, M. & Taketo, M.M. Morphological and molecular processes of polyp formation in Apc(delta716) knockout mice. *Cancer research* **57**, 1644-1649 (1997).
6. Brentnall, T.A*., et al.* Mutations in the p53 gene: an early marker of neoplastic progression in ulcerative colitis. *Gastroenterology* **107**, 369-378 (1994).
7. Rabinovitch, P.S*., et al.* Pancolonic chromosomal instability precedes dysplasia and cancer in ulcerative colitis. *Cancer research* **59**, 5148-5153 (1999).
8. Repici, A. & Tricerri, R. Endoscopic polypectomy: techniques, complications and follow-up. *Techniques in coloproctology* **8 Suppl 2**, s283-290 (2004).
9. Kiesslich, R*., et al.* Methylene blue-aided chromoendoscopy for the detection of intraepithelial neoplasia and colon cancer in ulcerative colitis. *Gastroenterology* **124**, 880-888 (2003).
10. Ullman, T., Croog, V., Harpaz, N., Sachar, D. & Itzkowitz, S. Progression of flat low-grade dysplasia to advanced neoplasia in patients with ulcerative colitis. *Gastroenterology* **125**, 1311-1319 (2003).
11. Libutti, S., Saltz, L. & Tepper, J. *Colon Cancer. DeVita, Hellman, and Rosenberg's Cancer: Principles & Practice of Oncology*, (Lippincott Williams & Wilkins, Philadelphia, 2008).
12. Skibber, J., Minsky, B. & Hoff, P. *Cancer of the colon*, (Lippincott Williams & Wilkins, Philadelphia, PA, USA, 2001).
13. Rosenberg, N. Submucosal saline wheal as safety factor in fulguration or rectal and sigmoidal polypi. *A.M.A. archives of surgery* **70**, 120-122 (1955).
14. Hirao, M*., et al.* Endoscopic resection of early gastric cancer and other tumors with local injection of hypertonic saline-epinephrine. *Gastrointestinal endoscopy* **34**, 264-269 (1988).
15. Ohkuwa, M*., et al.* New endoscopic treatment for intramucosal gastric tumors using an insulated-tip diathermic knife. *Endoscopy* **33**, 221-226 (2001).
16. Puli, S.R*., et al.* Meta-analysis and systematic review of colorectal endoscopic mucosal resection. *World journal of gastroenterology : WJG* **15**, 4273-4277 (2009).
17. Conio, M*., et al.* EMR of large sessile colorectal polyps. *Gastrointestinal endoscopy* **60**, 234-241 (2004).
18. Markle, B., May, E.J. & Majumdar, A.P. Do nutraceutics play a role in the prevention and treatment of colorectal cancer? *Cancer metastasis reviews* **29**, 395-404 (2010).
19. Muldoon, T.J*., et al.* Subcellular-resolution molecular imaging within living tissue by fiber microendoscopy. *Optics express* **15**, 16413-16423 (2007).
20. Chang, S.S*., et al.* High resolution microendoscopy for classification of colorectal polyps. *Endoscopy* **45**, 553-559 (2013).
21. Feldchtein, F*., et al.* In vivo OCT imaging of hard and soft tissue of the oral cavity. *Optics express* **3**, 239-250 (1998).
22. Bouma, B.E., Yun, S.H., Vakoc, B.J., Suter, M.J. & Tearney, G.J. Fourier-domain optical coherence tomography: recent advances toward clinical utility. *Current opinion in biotechnology* **20**, 111-118 (2009).

23. Gora, M.J.*, et al.* Tethered capsule endomicroscopy enables less invasive imaging of gastrointestinal tract microstructure. *Nature medicine* **19**, 238-240 (2013).
24. Leung, W.K.*, et al.* Detection of colorectal adenoma by narrow band imaging (HQ190) vs. high-definition white light colonoscopy: a randomized controlled trial. *The American journal of gastroenterology* **109**, 855-863 (2014).
25. Dinesen, L., Chua, T.J. & Kaffes, A.J. Meta-analysis of narrow-band imaging versus conventional colonoscopy for adenoma detection. *Gastrointestinal endoscopy* **75**, 604-611 (2012).
26. Nagorni, A., Bjelakovic, G. & Petrovic, B. Narrow band imaging versus conventional white light colonoscopy for the detection of colorectal polyps. *The Cochrane database of systematic reviews* **1**, CD008361 (2012).
27. Pasha, S.F.*, et al.* Comparison of the yield and miss rate of narrow band imaging and white light endoscopy in patients undergoing screening or surveillance colonoscopy: a meta-analysis. *The American journal of gastroenterology* **107**, 363-370; quiz 371 (2012).
28. Johnson, C.D. & Dachman, A.H. CT colonography: the next colon screening examination? *Radiology* **216**, 331-341 (2000).
29. Fidler, J.L.*, et al.* Detection of flat lesions in the colon with CT colonography. *Abdominal imaging* **27**, 292-300 (2002).
30. Tanaka, S.*, et al.* Detailed colonoscopy for detecting early superficial carcinoma: recent developments. *Journal of gastroenterology* **35 Suppl 12**, 121-125 (2000).
31. Jung, M. & Kiesslich, R. Chromoendoscopy and intravital staining techniques. *Bailliere's best practice & research. Clinical gastroenterology* **13**, 11-19 (1999).
32. Rembacken, B.J.*, et al.* Flat and depressed colonic neoplasms: a prospective study of 1000 colonoscopies in the UK. *Lancet* **355**, 1211-1214 (2000).
33. Lee, C.M., Engelbrecht, C.J., Soper, T.D., Helmchen, F. & Seibel, E.J. Scanning fiber endoscopy with highly flexible, 1 mm catheterscopes for wide-field, full-color imaging. *Journal of biophotonics* **3**, 385-407 (2010).
34. Kim, P., Puoris'haag, M., Cote, D., Lin, C.P. & Yun, S.H. In vivo confocal and multiphoton microendoscopy. *Journal of biomedical optics* **13**, 010501 (2008).
35. Wang, T.D.*, et al.* Functional imaging of colonic mucosa with a fibered confocal microscope for real-time in vivo pathology. *Clinical gastroenterology and hepatology : the official clinical practice journal of the American Gastroenterological Association* **5**, 1300-1305 (2007).
36. Achilefu, S. Lighting up tumors with receptor-specific optical molecular probes. *Technology in cancer research & treatment* **3**, 393-409 (2004).
37. Rao, J., Dragulescu-Andrasi, A. & Yao, H. Fluorescence imaging in vivo: recent advances. *Current opinion in biotechnology* **18**, 17-25 (2007).
38. Tromberg, B.J.*, et al.* Non-invasive in vivo characterization of breast tumors using photon migration spectroscopy. *Neoplasia* **2**, 26-40 (2000).
39. Frangioni, J.V. In vivo near-infrared fluorescence imaging. *Current opinion in chemical biology* **7**, 626-634 (2003).
40. Grosenick, D., Wabnitz, H., Rinneberg, H.H., Moesta, K.T. & Schlag, P.M. Development of a time-domain optical mammograph and first in vivo applications. *Applied optics* **38**, 2927-2943 (1999).
41. Shah, K. & Weissleder, R. Molecular optical imaging: applications leading to the development of present day therapeutics. *NeuroRx : the journal of the American Society for Experimental NeuroTherapeutics* **2**, 215-225 (2005).
42. Snoeks, T.J., Khmelinskii, A., Lelieveldt, B.P., Kaijzel, E.L. & Lowik, C.W. Optical advances in skeletal imaging applied to bone metastases. *Bone* **48**, 106-114 (2011).
43. Sima, P.D. & Kanofsky, J.R. Cyanine dyes as protectors of K562 cells from photosensitized cell damage. *Photochemistry and photobiology* **71**, 413-421 (2000).

44. Hamaoka, T*., et al.* Quantification of ischemic muscle deoxygenation by near infrared time-resolved spectroscopy. *Journal of biomedical optics* **5**, 102-105 (2000).
45. Nakayama, A., Bianco, A.C., Zhang, C.Y., Lowell, B.B. & Frangioni, J.V. Quantitation of brown adipose tissue perfusion in transgenic mice using near-infrared fluorescence imaging. *Molecular imaging* **2**, 37-49 (2003).
46. Herbort, C.P., LeHoang, P. & Guex-Crosier, Y. Schematic interpretation of indocyanine green angiography in posterior uveitis using a standard angiographic protocol. *Ophthalmology* **105**, 432-440 (1998).
47. Chen, S.J., Lee, A.F., Lee, F.L. & Liu, J.H. Indocyanine green angiography of central serous chorioretinopathy. *Zhonghua yi xue za zhi = Chinese medical journal; Free China ed* **62**, 605-613 (1999).
48. Haglund, M.M., Hochman, D.W., Spence, A.M. & Berger, M.S. Enhanced optical imaging of rat gliomas and tumor margins. *Neurosurgery* **35**, 930-940; discussion 940-931 (1994).
49. Haglund, M.M., Berger, M.S. & Hochman, D.W. Enhanced optical imaging of human gliomas and tumor margins. *Neurosurgery* **38**, 308-317 (1996).
50. Kusano, M*., et al.* Sentinel node mapping guided by indocyanine green fluorescence imaging: a new method for sentinel node navigation surgery in gastrointestinal cancer. *Digestive surgery* **25**, 103-108 (2008).
51. Evangelista, L*., et al.* Comparison between anatomical cross-sectional imaging and 18F-FDG PET/CT in the staging, restaging, treatment response, and long-term surveillance of squamous cell head and neck cancer: a systematic literature overview. *Nuclear medicine communications* **35**, 123-134 (2014).
52. Ren, B.X*., et al.* Magnetic resonance tumor targeting imaging using gadolinium labeled human telomerase reverse transcriptase antisense probes. *Cancer science* **103**, 1434-1439 (2012).
53. Achilefu, S*., et al.* Synergistic effects of light-emitting probes and peptides for targeting and monitoring integrin expression. *Proceedings of the National Academy of Sciences of the United States of America* **102**, 7976-7981 (2005).
54. Hackel, B.J*., et al.* 18F-fluorobenzoate-labeled cystine knot peptides for PET imaging of integrin alphavbeta6. *Journal of nuclear medicine : official publication, Society of Nuclear Medicine* **54**, 1101-1105 (2013).
55. Zhang, Y*., et al.* PET imaging of CD105/endoglin expression with a (6)(1)/(6)(4)Cu-labeled Fab antibody fragment. *European journal of nuclear medicine and molecular imaging* **40**, 759-767 (2013).
56. Chen, Z.Y*., et al.* Advance of molecular imaging technology and targeted imaging agent in imaging and therapy. *BioMed research international* **2014**, 819324 (2014).
57. McNichols, R.J. & Cote, G.L. Optical glucose sensing in biological fluids: an overview. *Journal of biomedical optics* **5**, 5-16 (2000).
58. Liu, Y*., et al.* Hands-free, wireless goggles for near-infrared fluorescence and real-time image-guided surgery. *Surgery* **149**, 689-698 (2011).
59. Neufert, C., Becker, C. & Neurath, M.F. An inducible mouse model of colon carcinogenesis for the analysis of sporadic and inflammation-driven tumor progression. *Nature protocols* **2**, 1998-2004 (2007).
60. Hsiung, P.L*., et al.* Detection of colonic dysplasia in vivo using a targeted heptapeptide and confocal microendoscopy. *Nature medicine* **14**, 454-458 (2008).
61. Tseng, W., Leong, X. & Engleman, E. Orthotopic mouse model of colorectal cancer. *Journal of visualized experiments : JoVE*, 484 (2007).
62. Nass, J.P. & Connolly, S.E. Current status of chromoendoscopy and narrow band imaging in colonoscopy. *Clinics in colon and rectal surgery* **23**, 21-30 (2010).

63. Foersch, S*., et al.* Molecular imaging of VEGF in gastrointestinal cancer in vivo using confocal laser endomicroscopy. *Gut* **59**, 1046-1055 (2010).
64. Neumann, H., Kiesslich, R., Wallace, M.B. & Neurath, M.F. Confocal laser endomicroscopy: technical advances and clinical applications. *Gastroenterology* **139**, 388-392, 392 e381-382 (2010).
65. Gruev, V., Perkins, R. & York, T. CCD polarization imaging sensor with aluminum nanowire optical filters. *Optics express* **18**, 19087-19094 (2010).
66. Charanya, T*., et al.* Trimodal color-fluorescence-polarization endoscopy aided by a tumor selective molecular probe accurately detects flat lesions in colitis-associated cancer. *Journal of biomedical optics* **19**, 126002 (2014).
67. Terzic, J., Grivennikov, S., Karin, E. & Karin, M. Inflammation and colon cancer. *Gastroenterology* **138**, 2101-2114 e2105 (2010).
68. Okayasu, I*., et al.* Dysplasia and carcinoma development in a repeated dextran sulfate sodium-induced colitis model. *Journal of gastroenterology and hepatology* **17**, 1078-1083 (2002).
69. Thaker, A.I., Shaker, A., Rao, M.S. & Ciorba, M.A. Modeling colitis-associated cancer with azoxymethane (AOM) and dextran sulfate sodium (DSS). *Journal of visualized experiments : JoVE* (2012).

Chapter 2
Surgical margin identification in colorectal cancer and in-situ validation using fluorescence-polarization imaging method

Chapter 2 is a reformatted version of a manuscript in submission: “Tauseef Charanya, Timothy York, Viktor Gruev, Samuel Achilefu et al. Surgical margin identification in colorectal cancer and in-situ validation using fluorescence-polarization imaging methods.” Under Dr. Samuel Achilefu’s supervision. My contributions to this work included designing the experiments, developing fluorescence-polarization microscopy using circular-polarized light, carrying out the imaging studies involving HT-29 orthotopic implantation and APC min mice, interpreting and analyzing data, and writing the manuscript. In this Chapter, I discuss my work in the identification of tumor margins in colon cancer models utilizing a NIR targeted probe developed and assessing the margins post-biopsy using a rapid, fluorescence-polarization microscopy method with the goal of serving as a substitution for gold standard H&E.

Abstract

Microscopic tumor cell invasion within the colon is known to complicate complete tumor resection and increase the risk of tumor metastasis. When assessing these margins, it is important to accurately delineate tumor margins and uninvolved tissues that are possibly infiltrated with tumor cells. We have developed a peptide based targeted near infrared (NIR) fluorescent molecular probe that can aid in accurate identification of tumor margins for surgical resection in colon cancer. The molecular probe was tested in an orthotopic, human derived colon cancer model and a mutant mouse model of colon cancer; adenomatous polyposis coli (APC*)* multiple intestinal neoplasia (min). Time-course in-vivo fluorescence imaging conducted using a small animal imaging system, along with ex-vivo corroboration studies using the proliferation marker BrdU, demonstrated the selectivity of this probe towards proliferating tumor edges. Fluorescence-polarization microscopy using circular polarized (CP) light was utilized as a supplementary tool for a quick assessment and validation of excised tissue to ensure complete tumor resection and to serve as a rapid intraoperative method for examining tumor margins prior to H&E-based pathological diagnosis.

1 Introduction

As many as 103,000 people are diagnosed with colon cancer every year in the United States and around 52,000 patients die of the disease annually, making it the second leading cause of death from cancer among adults.[1] By convention, staging of colon cancer is based on tumor size/invasiveness/histology by tumor node metastasis (TNM) staging. These invasive cancers can be completely curable by resection if they remain confined to the wall of the colon: mucosa-submucosa (T1-2, N0, M0 and T3-4, N0, M0). However, as the tumor invades past the muscle

layers and serosa, it spreads to nearby organs (T1-4, N1-2, M0) or to even distant organs (T any, N any, M1) through lymph node involvement, making it extremely difficult to resect and leading to possible recurrence.[2,3] Surgically resected neoplasia using widely accepted endoscopic mucosal resection (EMR) technique has yielded recurrence rates as high as 55% in some studies. [4,5] Lymph node metastasis with/without organ involvement in N0 is known to have a recurrence of 20%-30% and that of 50%-80% in T1-4, N1-2, M0 after surgery.[6] Mechanisms for local recurrence include and are not restricted to incomplete resection of transmural, mural, or lymphatic disease; tumor shedding; and local implantation.[7]

It is generally accepted that the colon cancer progression follows a benign adenomatous polyp - advanced adenoma – invasive cancer sequence. [8,9] APC mutations have been known to be the most common acquired mutation in sporadic colon cancer, occurring in 60% of all tumors. [10] The most common combination of mutations in the proto-oncogenes involved in the normal-adenoma-carcinoma progression includes p53 and APC (27.1%).[11] Subsequently, two clinically relevant models were chosen to best replicate the sequence of mutations for development of early adenoma and invasive cancer sequence. An APC min model was chosen to best recapitulate the molecular features associated with development of an early adenoma.[12] To establish a model for invasive colorectal cancer, an HT-29 colorectal cancer cell line (p53 mutant) was used to develop a tumor model via orthotopic implantation using a previously established method.[13] Together, the APC min and the orthotopic HT-29 models serve as ideal models for diagnosis and therapeutic efficacies of molecular probes in early and late stages of CRC development.

Conventional practice dictates diagnosis of colonic polyps to be governed by gold standard approaches such as endoscopic polypectomy that rely primarily on the trained eye of the physicians performing the procedure.[14] When compared to conventional colectomies, it has been shown that

laparoscopic methods aid in quality of life for the patient after surgery, although, have failed to improve the 5-year survival rate of CRC.[15] To improve resection, fluorescence-guided interventions emerge as a promising candidate especially when utilizing near infrared (NIR) light. Use of NIR light minimizes tissue auto-fluorescence and avoids absorption by hemoglobin (<650 nm) along with water and lipids (>900 nm), allowing for deeper tissue penetration and imaging. Furthermore, it takes advantage of molecular specific features of the diseased state when utilizing a molecular probe specific targeted approach.

With several developments made on the fluorescence-capable laparoscope end, a complimentary targeted molecular probe that reliably identifies adenomas in its earlier stage and invasive fronts of tumors in later stages with optimum specificity and sensitivity is still lacking. Studies utilizing an FDA approved NIR dye, indocyanine green (ICG) to detect tumors have demonstrated high background intensity in the subserosa around the tumor, resulting in unnecessary follow-up procedures.[16] For this reason, interest in developing tumor-specific optical contrast agents is rapidly growing. In order to address the shortcomings of surgical intervention for improved tumor removal, we report herein (i) a peptide-based integrin-targeting near infrared (NIR) fluorescent molecular probe (termed LS301) for CRC margin detection and (ii) subsequent, rapid tissue biopsy validation using fluorescence-polarization microscopy. The specificity of this molecular probe towards the margins of adenoma (APC min model) and invasive tumors (HT-29) was compared to that of a probe with its scrambled peptide sequence analog (termed LS340) *via* time-course in-vivo fluorescence imaging and ex-vivo validation studies using microscopy.

Furthermore, we extended the scope of the study by incorporating a multi-modal microscopy approach that provides both functional and structural information of biopsied tissue. The tumor-specific probe reports functional information *via* fluorescence, whereas polarization

imaging reports structural information of the biological tissue of interest *via* changes in degree of linear polarization and angle of polarization. Since muscle tissue is known to have higher birefringence due to the increased concentration of collagen fibers, it provides a unique, higher polarization signal when compared to the tumor tissue. On the other hand, tumor tissue has been shown to have a lower polarization signal compared to surrounding uninvolved tissue as reported previously.[17] We have further explored the potential of this technique to also identify and differentiate tumor tissue from uncompromised submucosal tissue in this study. We have recently demonstrated the use of this setup in a mouse mammary carcinoma model where this strategy delivers the same vital information as an H&E stain while providing the pathologists and surgeons a faster assessment of the tumor- surrounding muscle tissue as there is no staining procedure required.[18] The study demonstrates the potential feasibility of utilizing the targeted molecular probe and post-biopsy fluorescence-polarization validation strategy to assess diverse stages of colon cancer. Utilizing the specificity of the molecular probe to guide biopsies via fluorescence signature and instantly cross-validating biopsy sections using a dual, stain-free microscopy approach is expected to accelerate medical decision, and improve clinical outcomes with minimal recall rates.

2 Methods

2.1 Near-infrared (NIR) Contrast Agents

LS301 and its scrambled peptide analog, LS340, were synthesized by our lab by a modification of a previously described method.[19] In this case, a Gilson HPLC system and the microwave peptide synthesizer were used to prepare the peptide and purify the end product. LS301 consists of a near-infrared fluorescent dye, cypate (780 $_{ex}$/ 830 $_{em}$) and a cyclic peptide sequence D-Cys-Gly-Arg-

Asp-Ser-Pro-Cys-Lys (c($_D$CGRDSPC)K). LS340 contains cypate with a scrambled peptide analog Lys-Asp-D-Phe-Arg-Gly (c(KDfRG)).[20] LS340 was synthesized in a similar way to LS301. The conjugation of the dye and peptide sequence was characterized by spectroscopy methods, analytical HPLC, and electrospray ionization mass spectrometry.

2.2 Steady-state Optical Measurements

Absorption spectra were recorded on a DU 640 UV-Visible spectrophotometer (Beckman Coulter, Brea, CA), and fluorescence spectra were recorded on a Fluorolog-3 spectrophotometer (Horiba Jobin Yvon, Inc., Edison, NJ). All fluorescence measurements were conducted at room temperature and were recorded at excitation of 700 nm and emission scan from 740 to 900 nm.

The relative fluorescence quantum yields of the dye were determined using equation 1:

$$\Phi_{F(X)} = (A_S/A_x)(F_x/F_S)(n_x/n_s)^2\ \Phi_{F(S),}$$

Equation 1

where $\Phi_{F(X)}$ is the fluorescence quantum yield, A is the absorbance, F is the area under the emission curve, n is the refractive index of the solvents used in the measurement and the subscripts s and x represent the reference and unknown parameters respectively. Indocyanine green (ICG; Akorn, Inc. Decatur, IL) was used as a reference standard, which has a quantum yield of 0.09 in MeOH at 700 excitation.

2.3 Cell Line

HT-29 human colon cancer cell line was purchased from the American Type Culture Collection. These cells were maintained in Dulbecco's Modified Eagle Medium (DMEM) supplemented, with

10% fetal bovine serum (Hyclone). All cells were cultured in a humidified incubator at 37^0C with 5% CO_2.

2.4 HT-29 Orthotopic Model

All animal studies were performed according to protocols approved by at Washington University School of Medicine Animal Studies Committee for humane care and use of laboratory animals. The orthotopical implantation model has been previously described.[13] Briefly, six-week old athymic nude mice (NCr- nu/nu; NCI Fredrick National Laboratory) were anesthetized with ketamine (85 mg/kg) and xylazine (15 mg/kg) *via* an intraperitoneal injection (IP) prior to performing laparotomy. Isoflurane gas (2% v/v in 100% O_2) was delivered via nosecone for maintenance of anesthesia throughout the procedure. A 2-3 cm incision was made to expose the abdominal cavity and the cecum was identified and exteriorized. Warm saline was used to keep the cecum moist during this procedure. 1 x 10^6 cells suspended in 50 μL of phosphorus buffered saline were injected into the cecal wall from the serosal side. The lack of leakage of fluid from the cecal wall and the formation of a visible bulla between the subserosal and submucosal tissue were used as an indication of a successful injection. The cecum was returned to abdominal cavity and the mouse abdominal wall was closed using a simple running stitch. Mice were evaluated for tumors 4-6 weeks post implantation. They were randomly separated in two different groups (n = 3) for administration of LS301 or LS340. 100ul (in 20%DMSO and 80% saline) of 60 uM of imaging agent were injected per mouse via the lateral tail vein. Two hours prior to sacrificing the mouse, a thymidine analog, 5-bromo-2-deoxyuridine (BrdU) (Life Technologies, New York, USA) was injected intraperitoneally at a volume of 1 ml concentrated reagent per 100 grams of body weight.

2.5 APC min model

C57Bl/6J $APC^{min/+}$ male mice were obtained from Jackson Laboratory. Mice were fed a 10% fat diet (Harlan Teklad) and maintained as approved by Animal Studies Committee of Washington University School of Medicine. Six mice were separated in groups of 2; for administration of LS301 or LS340. Mice were fasted overnight to minimize fecal matter in their digestive tract and minimize interference with time-course fluorescence imaging. 24 hours prior to sacrifice, 100μL solution of 60μM concentration of molecular agent was administered intravenously. Once sacrificed, the colon was exteriorized, rinsed thoroughly, and imaged using small animal imaging system (described below). Post imaging, colons were carefully cut open and pinned to expose the polyps within. Sections were inspected using a Nikon SMZ800 dissection microscope.

2.6 Ex vivo APC min mice imaging

Colon sections with identified polyps were isolated for further microscopy studies. A clearing agent, 50μL glycerol was pipetted onto 8-10 mm of colon tissue sections to allow for microscopy. A ZEISS Axioskop 2 MOT microscope with full light capabilities was used to evaluate tissue morphology of adenomas and concurrently capture z-stack images of the identified tissue sections with polyps. Axiovision image analysis software was used for stacking the z-stack images prior to further processing using 3-D reconstruction using Matlab Image Analysis Software. For NIR microscopy, an Olympus BX51 upright epifluorescence microscope (Olympus America, Center Valley, PA, USA) using 775 +/-50 nm excitation, 810 nm long-pass dichroic, and 845 +/-55 nm emission filters was used.

2.7 Small Animal Imaging

The Pearl NIR fluorescence imaging system (LiCor Biosciences, Lincoln, Nebraska) was used to perform imaging of live mice, as reported previously.[21] Isoflurane gas (2% w/v in 100% O_2) was delivered via nosecone during the process of imaging nude mice bearing HT-29 tumors. Mice were positioned supine on the heated imaging platform. Pre-injection scans were performed to assess the autofluorescence signals. A 785 nm excitation wavelength and 830 nm emission was used to conduct in vivo imaging. Scans were obtained immediately, 1 hour, 4 hours, and 24 hours post administration of imaging agent. Colons exteriorized from APC min mice were placed in a petri dish prior to imaging and identifying regions of interest (ROI). For each selected region, the mean fluorescence intensity values for tumor and non-tumor tissue were selected and reported for analysis. Mean fluorescence intensity was determined for each tissue by ROI analysis and combined for each group for statistical analysis.

2.7 Bromodeoxyuridinen (BrdU) labeling and immunohistochemistry

Each mouse was injected with 1 ml/100g body weight BrdU labeling reagent (Life Technologies, New York, USA) intraperitoneally, two hours prior to sacrifice. Once sacrificed, both primary tumors from the cecum and secondary tumors from the distal colon were excised and frozen under OCT media. Tissues were sectioned in 10-μm thicknesses and used for fluorescence microscopic imaging and (Diaminobenzidine (DAB) BrdU staining. For BrdU staining, protocol provided by AbCam, Cambridge, USA was utilized while using DAB as the marker and tissues were counterstained hematoxylin and eosin.

2.8 Histology

After sacrificing the mice, the tumors were resected along with surrounding cecum and the tissue was frozen in OCT. The tissues were sectioned in the cryostat to 10 uM thickness. Slides were stained with BrdU antibody and counterstained with Hematoxylin for histological reference using a BrdU staining kit (Invitrogen) according to the manufacturer's protocol. Briefly, the slides were submerged in 3% H_2O_2 (in methanol) and rinsed with PBS. Slides were incubated with denaturing solution, rinsed, blocked with blocking solution and incubated with biotinylated mouse anti-BrdU reagent. After washing with PBS, streptavidin-peroxidase reagent was applied to each slide, followed by a brief incubation with antibody mixture and counterstaining with hemotoxylin. Slides were dehydrated in a graded series of alcohol and mounted with histomount.

2.9 Polarization Microscopy of Invasive HT-29 cancer

A complementary fluorescence and polarization microscope with division of focal plane (DoFP) polarimeter used for this portion of the study was described earlier.[18,22] For fluorescence microscopy, slides were taken directly from a -80 degree freezer and imaged with an Olympus BX51 upright epifluorescence microscope (Olympus America, Center Valley, PA, USA) using 775 +/-50 nm excitation, 810 nm longpass dichroic, and 845 +/-55 nm emission filters. For polarization microscopy, a DoFP sensor was utilized which uses a CCD monolithically integrated with aluminum nanowire polarization filters. The imaging array was arranged in blocks of four (two-by-two) superpixels. Each superpixel consists of four pixels that are composed of nano-wire polarization filters with the transmission axis oriented at 0^0, 45^0, 90^0, and 135^0. These nanowires are 70 nm wide, 140 nm tall, and spaced 140 nm from center to center. A detailed description of the fabrication procedure these polarization filters has been described before.[22] The raw data

obtained from the DoFP sensor is first calibrated [23] and interpolated [24] to obtain accurate and high spatial resolution polarization information about the imaged tissue.

Input circularly polarized light was generated by the combination of a achromatic quarter wave plate (Thorlabs AQWP05M-600) and a linear polarizer (Newport 10LPVISB), both designed for use in the visible (400nm to 700nm) spectrum. The quarter wave plate was aligned at 45 degrees with respect to the linear polarizer on a precision rotational stage. The circular polarizer was placed after the broadband illumination and transmitted through the sample. Using a Division-of-Focal-Plane polarimeter, the angle of polarization (AOP) and Degree of linear polarization (DoLP) was then measured for the sample. The DoLP is related to the retardance of the tissue while the AOP provides information in regards to the orientation of the muscle fiber.

2.10 Statistical Analysis

All data values are represented as mean ± SEM. A two-sided pairwise t test was applied for analysis. P values of <0.05 were considered statistically significant.

3 Results

3.1 Characterization of targeted molecular probes

We have made use of the unique ability of NIR light to image deeper in the tissue by conjugating the reporter molecule (cypate) to a targeting moiety comprising of peptide sequence D-(Cys-Gly-Arg-Asp-Ser-Pro-Cys-Lys conjugated to NIR dye, cypate (LS301). We have previously reported on the ability of this molecular probe to selectively accumulate in tumors as compared to surrounding tissues.[21] We further explored the specificity of the molecular probe towards a tumor-

front and tumor core and compared it with a negative control, scrambled peptide sequence (Lys-Asp-D-Phe-Arg-Gly) conjugated to cypate (LS340). In this process, we ensured the maintenance in size and hydrophobicity of the two compounds. A detailed description of the synthesis of such cypate based molecular probes has been reported earlier.[19] The chemical structure of both probes is shown in Fig. 1a and 1b. Their excitation and emission characteristics have been reported in Fig. 1c and 1d. Furthermore, we tested the quantum yield of both compounds with FDA approved NIR agent, indocardiogreen (ICG) in two different solutions; dimethyl sulfoxide (DMSO) and phosphate buffered saline with 1% bovine serum albumin (PBS/BSA) as illustrated in Fig. 1e. 1% BSA in PBS was utilized due to its ability to replicate a similar environment in solution as that of serum in vivo.[25] Both physical and chemical characteristics of the probe hint at the similarities that exist with current, FDA approved dye.

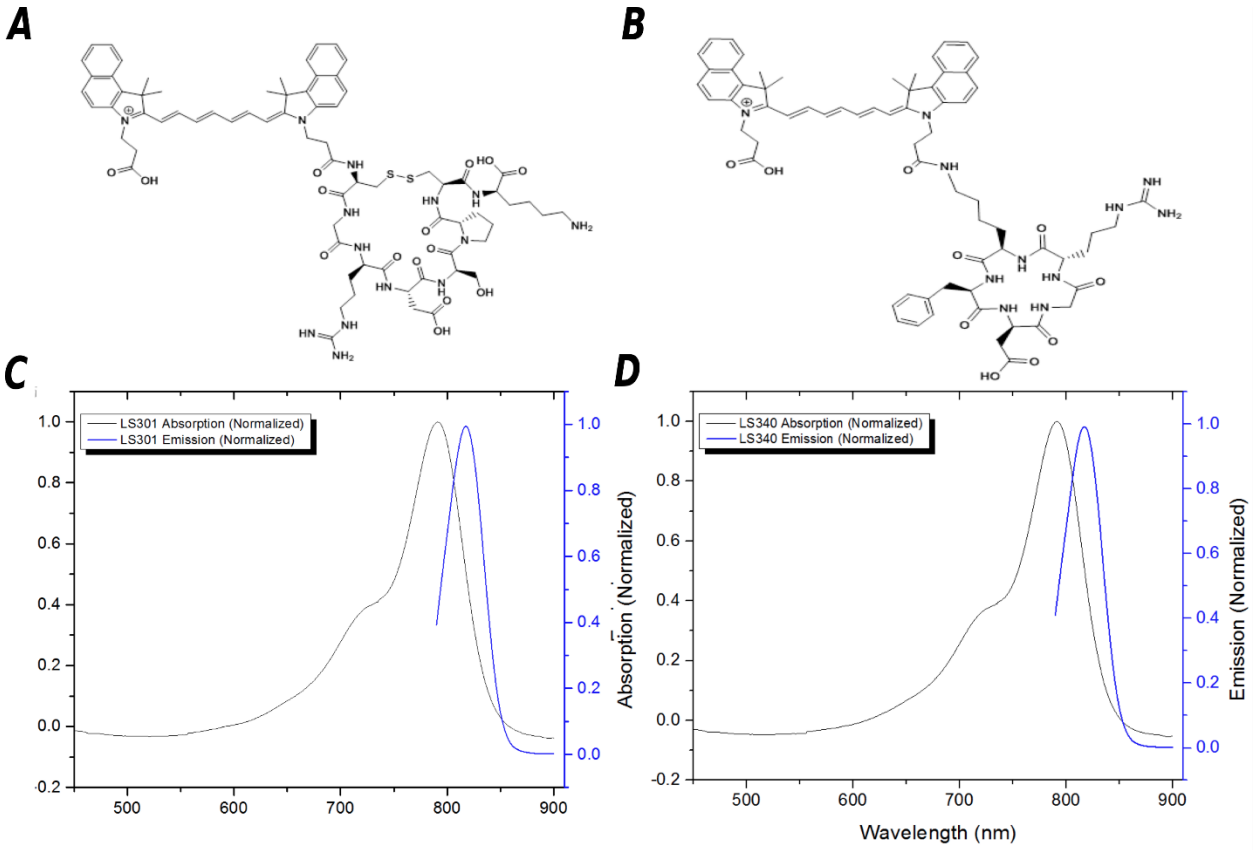

E

Table 1. Quantum Yield of studied cyanines in DMSO and PBS/BSA

Compound	QY (DMSO)	QY (BSA/PBS)
ICG	0.13	0.08
LS301	0.10	0.03
LS340	0.09	0.04

Figure 1. Physical and chemical characteristics of molecular probes, LS301 and LS340. (A) Chemical structure of LS301 (c($_D$CGRDSPC)K) and (B) LS340 (c(KDfRG)). Normalized absorption and emission spectra of (C) LS301 and (D) LS340. (E) Table detailing quantum yield of LS301, LS340 and FDA approved indocyanine green (ICG) dissolved in both dimethyl sulfoxide (DMSO) and phosphate buffered saline with bovine serum albumin (BSA).

3.2 Efficacy study in orthotopic colorectal cancer (HT-29) and APC min models

An orthotopic HT-29 colorectal cancer (CRC) model was first employed to compare the efficacy of the molecular probe in an advanced colorectal carcinoma model. Dosing of molecular probes was pre-established in study report previously[21] as 0.3mg/kg. Post administration, PearlCam software was used to analyze the images taken and report fluorescence intensity in arbitrary values. Values were normalized for both compounds over a 24-hour time period for *in vivo* and ex vivo imaging. Fig. 2a demonstrates the time-course fluorescence imaging using the NIR fluorescent probe LS301. It is able to highlight the ability of LS301 to maintain good tumor localization, with high contrast between the primary tumor and surrounding regions at 4 and 24 hours post administration. In contrast, LS340 demonstrated a very short-lived accumulation in the primary tumor at 4-hr time point and cleared via the primary clearance organ for hydrophobic dyes, the liver, by 24 hours. In order to quantify the dye retention in tumors *via* fluorescence signal, mean signal-to-noise ratio (SNR) was computed over time in regions identified as primary tumor based on site of administration and post-sacrifice primary tumor location verification. Using equation 2, the SNR computed demonstrated greater than five-fold retention of LS301 in primary tumor when compared to its scrambled peptide counterpart, LS340 at 24 hours as shown in Fig. 2b.

$$\text{Mean SNR} = \frac{\dfrac{\text{Total intensity from tumor}}{\text{Area of ROI containing tumor}} - \dfrac{\text{Total background intenisty}}{\text{Area of ROI containing background}}}{\text{Standard Deviation of background intensity}}$$

Equation 2

Furthermore, in 30% of the mice, the palpable tumor region was known to extend further to what was later identified as, a secondary, smaller, non-palpable, locally metastasized tumor in the distal colon. The region encompassing secondary tumors was identified and corresponding

fluorescence values were recorded at different time points and compared with fluorescence originating from surrounding uninvolved region to provide tumor-to-background ratios in mice treated with LS301 or LS340, as shown in Fig. 2b. A tumor-to-background ratio (TBR) of 4.5 was observed for primary tumors and that of 3 for secondary tumors in mice administered with LS301. Conversely, a TBR of 0.8 was observed for primary tumors and that of 0.95 for secondary tumors in mice administered with LS340.

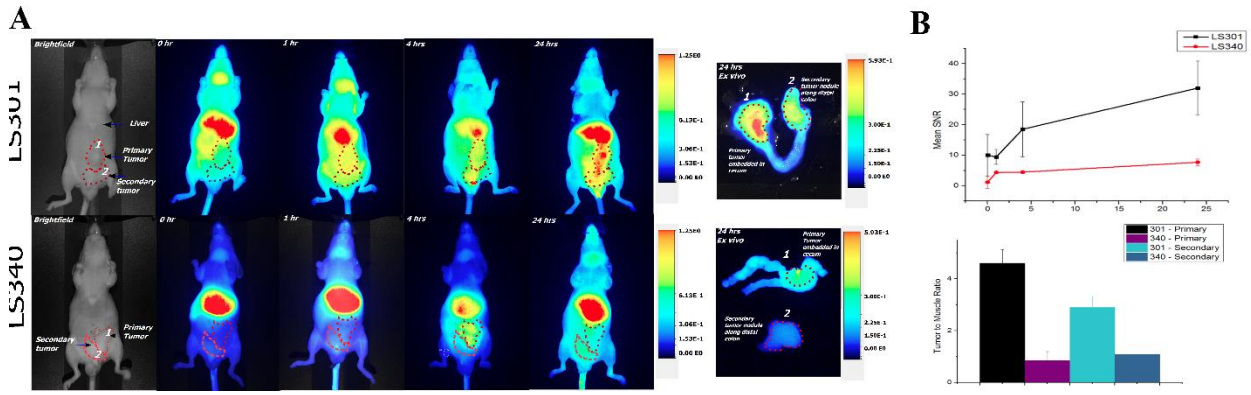

Figure 2. Time course fluorescence imaging in orthotopic HT-29 colorectal cancer model. (A) Images in the top row depict mice treated with LS301 and bottom row that with LS340. Both palpable and non-palpable tumors identified post-sacrifice are marked by a red dotted line. NIR fluorescence Images were acquired with the 800 nm channel over time (0 hr, 1hr, 4 hours, and 24 hours) after administration of 6 nanomoles of LS301 or LS340 solution. 24 hours post administration, animals were euthanized and tumors within the cecum along with locally invaded tumors along the distal colon (not palpable) were exteriorized and imaged *ex* vivo. (B) Mean signal to noise ratio (SNR) measured over time. Mean background intensity of the region of interest marking the exteriorized, visible tumors was compared to that of another region of interest in the same mouse marking surrounding uninvolved tissue and muscle. Error bars represent 95% confidence interval.

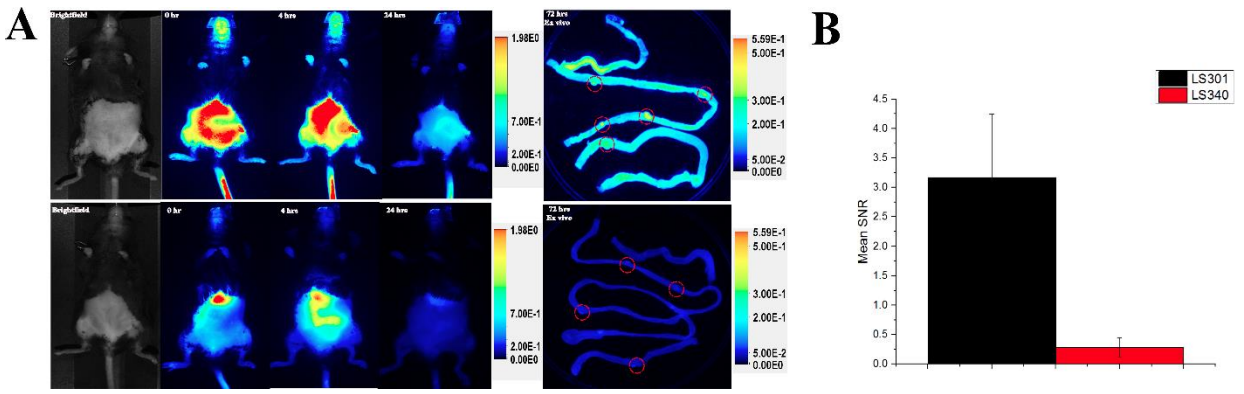

Figure 3. Time course fluorescence imaging in APC min model. (A) Images in the top row depict mice treated with LS301 and bottom row that with LS340. NIR fluorescence Images were acquired with the 800 nm channel over time (0 hr, 1hr, 4 hours, and 24 hours) after administration of 6 nanomoles of LS301 or LS340 solution. 24 hours post administration, animals were euthanized and the small and large bowel were exteriorized. Visible polyps were identified and later verified by microscopy. Polyps identified in the small and large bowel are both marked by a dotted red circle. (B) Mean fluorescence intensities for both LS301 and LS340 in regions identified as polyps was compared to surrounding uninvolved regions to provide Mean SNR values. Error bars represent 95% confidence interval.

Similarly, a time-course fluorescence imaging was conducted on APC min model as shown in Fig. 3a. Due to the presence of a significant number of <3mm polyps in the stomach and small bowel, a higher fluorescence intensity is observed in these regions with LS301 versus LS340, due to enhanced selectivity. A mean SNR of 3.38 ± 0.7 was observed with mice treated with LS301 as compared to 0.3 ± 0.15. To further confirm the presence of polyps, colonic segments were isolated based on regions exhibiting higher fluorescence and the presence/absence of polyps was later verified by *ex vivo* tissue microscopy studies as shown in Fig. 4a. SNR were obtained of regions identifying adenomas (later verified) and surrounding uninvolved colon tissue. Consistent with the ability of LS301 to demarcate the boundaries of the advanced staged tumors as in HT-29, Figure

4b presents a mean SNR of 45 ± 7.2 using LS301 as opposed to 3 ± 1.8 using LS340 amongst polyps arising in APC min model. Enhanced SNR and TBR ratios using LS301 in both HT-29 and APC min reaffirmed the specificity arising from GRD based targeting sequence in LS301.

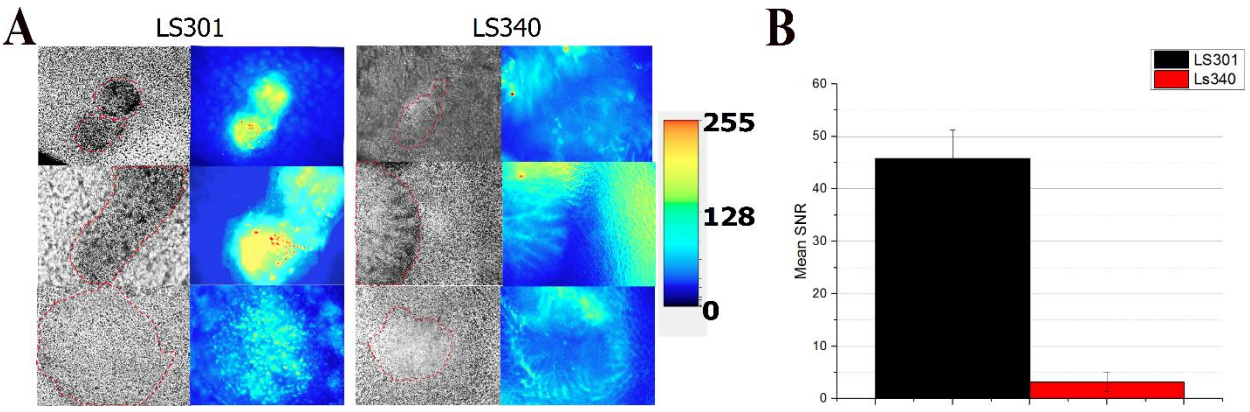

Figure 4. Ex vivo brightfield and fluorescence microscopy of polyps in APC min model using LS301 and LS340. (A) Boundaries of identified polyps are marked by a dotted red line in the brightfield image and corresponding NIR fluorescence images are presented alongside. (B) Mean signal intensities of regions identified and verified as polyps are compared to those of surrounding uninvolved regions.

3.3 Ex vivo fluorescence microscopy and corroboration with proliferation marker

To further investigate the binding preference of the molecular probes within tumor microenvironment, two primary regions within the tumor were selected; tumor core and boundaries. Regions with similar morphology within tumors treated with LS301 and LS340 were compared to identify differences in binding patterns between both molecular probes. BrdU, marker widely known to identify proliferative regions, was used as a standard for corroborating NIR fluorescence binding patters. When compared to LS340, the binding pattern of LS301 corroborated extremely well with BrdU, in both; tumor core as shown in Fig. 5a, and tumor-uninvolved

boundary, as shown in Fig. 5b. LS 301 localized to the edges of the tumor making it a potential tool for assessing tumor margins during tumor resection.

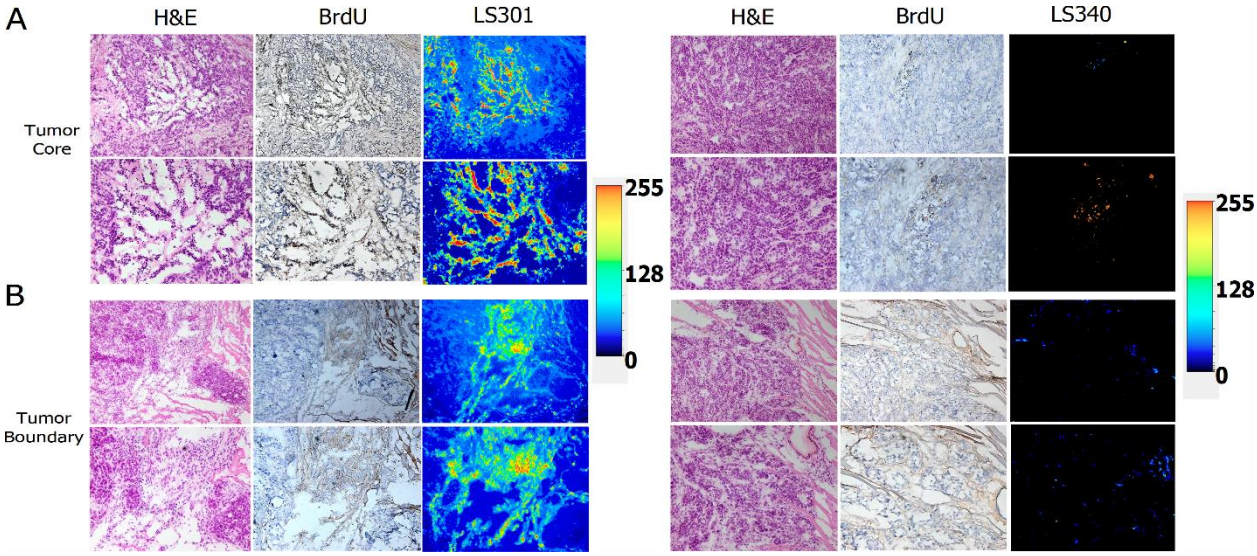

Figure 5. Comparing binding specificity of LS301 and LS340 with proliferation marker, BrdU (Dab counterstain) in HT29 tumor core and invasive boundaries. (A) H&E, BrdU counterstained with hematoxylin and NIR fluorescence image of tumor core region using LS301 and LS340. (B) H&E, BrdU counterstained with hematoxylin and NIR fluorescence image of tumor boundary using LS301 and LS340.

3.4 Using circular polarized (CP) light for polarization microscopy

Targeted fluorescence guided surgery utilizing molecular beacons that identify invasive tumor fronts is a strong first step towards diagnosis. To ensure complete resection, polarization and fluorescence microscopy were used in conjunction. A simple system of linear polarizer and quarter wave retarder was developed to convert the incident unpolarized light to circularly polarized (CP) incident light. Current methods utilize a specialized stage that consists of a 360 degree rotating specimen stage to facilitate orientation studies with centration of the objectives and stage with microscope optical axis to allow for center of rotation to coincide with the center of the

field of view. However, this system configuration does not allow for a real-time assessment of the tissue. We circumvented these challenges by developing an imaging configuration and sensor setup capable of reporting DoLP and AOP changes in the transmitted light.

Briefly, CP light that gets transmitted through a birefringent object, becomes elliptically polarized on the output where the ellipticity is directly dependent on how birefringent the tissue under investigation is. The more birefringent muscularis mucosa and subserosa regions alter the polarization state of light to a more linearly polarized state. Both; the Angle of Polarization (AOP) and Degree of Linear Polarization (DoLP), present varying information regarding the polarization state of transmitted light through the tissue. With incident CP light, the transmitted AOP reports the alignment of the dominant birefingent axis in the tissue. On the contrary, dense, tumor tissue has a two-fold effect on the polarization state of light. Firstly, the tumor tissue lacks birefringence, causing predominantly circularly polarized light transmitted through the tissue, causing a lack of detected light with a high degree of linear. Furthermore, the tumor tissue possesses differential properties such as greater radius and density of nuclei, higher absorption coefficients and higher order of back scattering of light[26,27] when compared to surrounding uninvolved tissue, contributing to a lower DoLP signature and a higher contrast with surrounding uninvolved tissue.

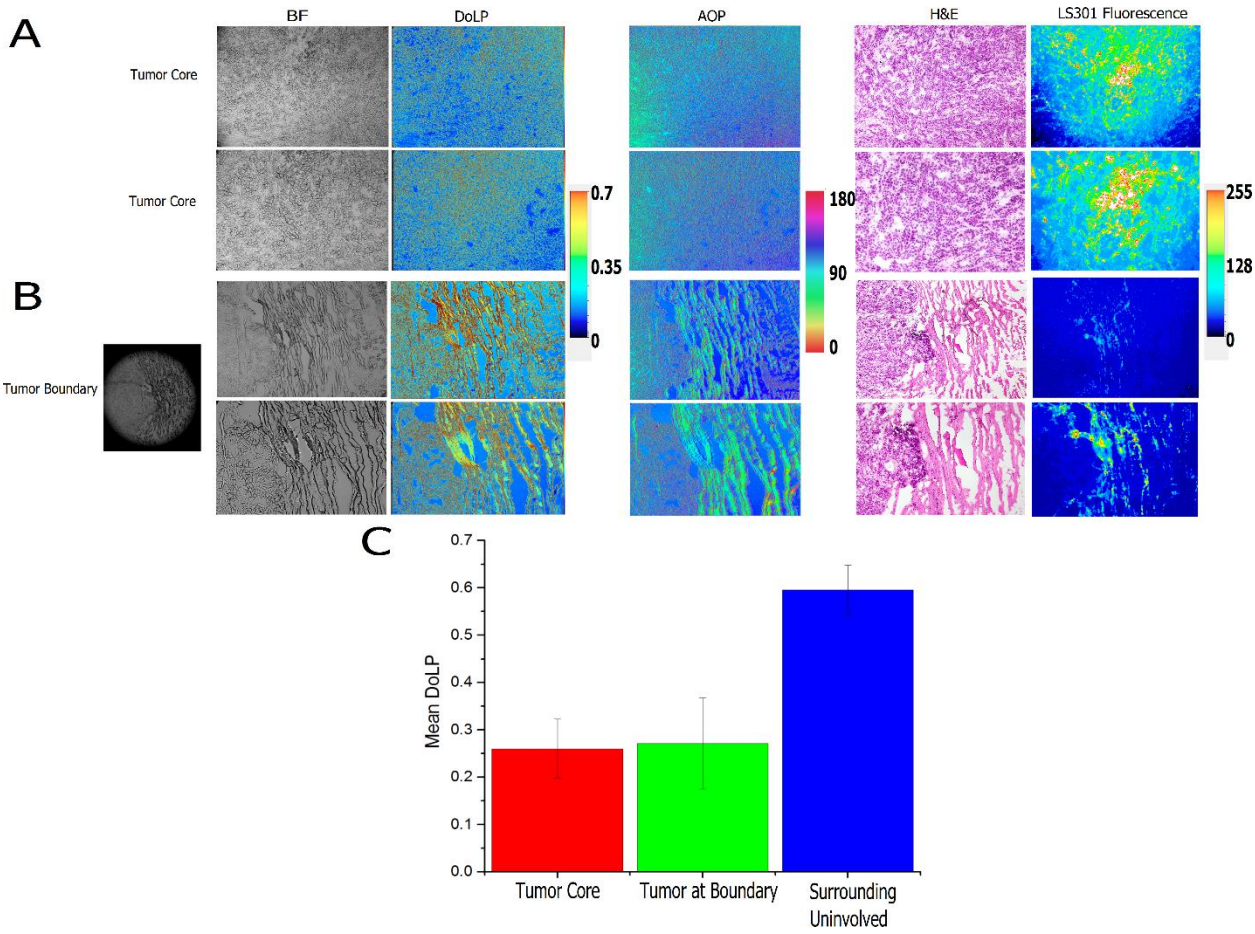

Figure 6. Polarization-Fluorescence microscopy of tumor core and tumor boundary in HT-29 orthotopic model. (A) BF image of tumor core alongside corresponding DoLP and AOP images using circularly polarized incident light. The same region is identified for NIR fluorescence and verified by H&E. (B) BF image of tumor boundary alongside corresponding DoLP and AOP images using circularly polarized incident light. The same region is identified for NIR fluorescence and verified by H&E. Tumor boundary inset illustrates the region at a lower magnification. (C) Mean DoLP values computed by selecting three different regions – tumor core, tumor at the boundary and surrounding uninvolved tissue. Statistically significant mean DoLP values obtained with $p<0.005$

3.5 Fluorescence-Polarization Microscopy of invasive HT-29 tumor front using incident circularly polarized light

Fluorescence microscopy was used as a first level assessment tool to identify the tumorous regions based on NIR readout sensitive to molecular-level based sensitivity. Polarization microscopy served as a label free, validation technique to present structural information needed to provide physical context to NIR image and to serve as an additional contrast tool based on tissue composition and orientation. Polarization data was captured in real-time in the form of two readouts; degree of linear polarization (DoLP) and angle of polarization (AOP). Readouts obtained for both tumor core and tumor-uninvolved surrounding tissue boundaries are presented in Figures 6a and 6b. Furthermore, corresponding NIR readouts of the same region are also presented to accentuate the complimentary nature of both modalities. Lack of morphological information provided by NIR image in Fig. 6b is compensated for by the DoLP and AOP image, as shown by its ability to identify birefringent muscle tissue and thereby provide morphological context. Regions identified by fluorescence-polarization microscopy were verified by histology *via* gold-standard H&E stain and presented in Figure 6a and 6b. Mean DoLP values were computed and are shown in Figure 6c. The core and the invading front of the tumor had similar mean DoLP values of 0.2603 +/- 0.0625 and 0.2715 +/- 0.0961. In comparison, surrounding uninvolved regions had mean DoLP values of 0.5959 +/- 0.0524. Due to lack of change in structural orientation of tissue composition, there was no change observed in AOP for tumor core. As for the tumor boundary and surrounding uninvolved tissue, presence of birefringent muscle fibers oriented normal to the tumor, resulted in a strong contrast. This method demonstrated its potential of serving as a definitive tool for distinguishing structural features that are non-tumor like in a label-free, real-

time fashion and complement molecular-sensitive information, obtained *via* a fluorescence readout.

4 Discussion

We have developed a targeted molecular probe to specifically identify invasive tumors fronts for improved tumor resection and an imaging strategy that would help validate complete tumor removal. Unlike current targeted-imaging approaches to interrogate molecular and structural signatures of CRC, the combined fluorescence and polarization contrasts create a new paradigm for identifying colonic lesions with high accuracy. An APC min model was chosen to best recapitulate the molecular features associated with development of an early adenoma while an orthotopic HT-29 colorectal cancer tumor model was used to best replicate an invasive cancer. The nature of the orthotopic implantation procedure, allows the tumor to start growing from the cecal wall and penetrate deeper into the serosa, helping us to better identify and report the invasion process. Optical imaging has already proven itself as a reporting strategy in the form of clinical endoscopy, laparoscopy amongst other constantly emerging optical-based methods including confocal laser endomicroscopy, utilizing targeted molecular imaging.[28]

Targeted-molecular imaging efforts to specifically identify polyps have come in the form of using a Cy 5.5 conjugated cathepsin B to identify polyps in APC mice[29] or even topically applying fluorescein conjugated peptide sequence (VRPMPLQ) to identify dysplastic mucosa.[28] However, such agents are limited by their shallow tissue penetration and their lack of specificity towards invading tumor boundaries, which limit their usefulness for guiding surgical resection. Use of NIR molecular probes bridges this gap by allowing for imaging through deeper tissue penetration while maintaining sensitivity. Furthermore, while efforts in this area over the last decade have been on identifying dysplastic lesions and polyps, there has been a lack of effort in developing probes

capable of specifically reporting invading tumor margins that have perforated deeper into the tissue.[28,29] We have utilized the unique ability of our targeted molecular probe LS301 to target invasive fronts of tumor specifically with high specificity and sensitivity in early and late stage colon cancer models.

Provided the application of invasive margin detection for improved resection, topical administration approach that is generally taken for improved visualization in colonoscopy screenings is deemed unsatisfactory due to insufficient penetration through the tumor mass. In order to capture the infiltrated tumor cells in the subserosa, past the initial mucosal boundary, an intravenous delivery approach was chosen. Time-course NIR fluorescence study highlighted the ability of LS301 to capture early adenomas as shown in Figure 3a, along with primary and secondary, locally invaded tumors, as presented in Figure 2a with preferential binding over its surroundings. This was evident by TBR values of 4.5 and 3 for primary and secondary tumors and that of 3.25 for polyps. Its counterpart, LS340 (scrambled peptide analog) demonstrated no such retention and selective localization within the tumors or polyps as shown in Figure 2a and Figure 3a. The specificity of targeting moiety in LS301 is highlighted, when comparing its binding preferences to that of, scrambled peptide counterpart, LS340.

Consistent with in-vivo findings, examination of ex-vivo tissue demonstrated the enhanced ability of LS301 to bind to tumor edges, which are reportedly proliferative in nature. To further validate our claim, we compared the binding preference of LS301 with BrdU. As a structural analog of thymidine, BrdU can get incorporated in the DNA during the synthesis phase of the cell cycle as a uridine derivative, thereby serving as a proliferation marker. By comparing various tumor tissue morphologies and surrounding uninvolved regions as shown in Figure 5b, LS301 emerges as a strong candidate for detecting the proliferating regions of the tumor with 100%

sensitivity and specificity. Furthermore, unlike existing molecular probes that are confined to identify only specific stages of tumorigenesis, LS301 offers the ability to determine multiple stages of cancer development. By demonstrating preferential binding towards proliferative regions within the tumor, LS301 has high potential to improve the management of colorectal cancer, by guiding complete tumor resection.

In order to resect the tumor completely, it is important for the surgeon to be able to judge the stage of the tumor, which is classified by the level of invasion. As tumors surpass the mucosa and submucosal layers towards the muscle and serosa (T1-4, N1-2, M0), it gets very close to spreading to nearby organs via lymph node involvement. With the HT-29 orthotopic model, we were able to simulate a T3-4, N0, M0 colorectal cancer type of tumor invasion. For a label free, quick assessment of resected tumor tissue, and to satisfy the diagnosis provided by a pathologist *via* H&E staining, there is a need to identify both, molecular and structural specific features. While LS301 has immense potential to satisfy the needs from molecular front, polarization imaging has the ability to provide this information reliably from the structural front. Ability of CP light to detect birefringence in samples under investigation was employed towards tumor boundary assessment using a polarization-sensitive imager. While readout AOP reports specifically on the orientation of birefringent tissue under investigation such as collagen fibers and muscle sarcomeres, DoLP reports on the fraction of transmitted light that is linearly polarized due to birefringence in the tissue. We have previously reported differences in DoLP signature in cancerous and surrounding uninvolved tissue using a similar polarization-sensitive imager coupled to an endoscope.[17] Cancerous tissue possesses distinct morphological features, such as increased nuclear size and increased nuclear/cytoplasmic ratio, which results in significant multiply scattered components of light and a corresponding decrease in DoLP signature. A mean DoLP ratio of 2.3 fold was observed

between cancerous and surrounding uninvolved tissues as shown in Figure 6c. The exceptionally high DoLP signal in surrounding uninvolved tissue stems from the formation of firmly matted fibrotic bands within the serosa and mesentery and the increase in concentration of linearly birefringent material such as actin. We demonstrated our ability to rapidly interrogate regions of interest in real time (at 40 frames per second) using this method.

The combination of an invasive tumor front-targeting molecular probe that has the potential to be easily integrated with a NIR-capable endoscope and the development of a microscopy based fluorescence-polarization tumor-boundary assessment strategy, provides a new paradigm for accurate complete resection of colorectal cancer. While NIR-based fluorescence endoscopy could serve as a strong first line of defense, polarization-fluorescence microscopy, in conjunction, has potential to verify and validate complete resection prior to a lengthy H&E staining and diagnosis process. The system and method described in this study are applicable to the assessment of other pathologic conditions, such as upper GI lesions, and melanoma.

References

1. Siegel, R.L., Miller, K.D. & Jemal, A. Cancer statistics, 2015. *CA: a cancer journal for clinicians* **65**, 5-29 (2015).
2. Libutti, S., Saltz, L. & Tepper, J. *Colon Cancer. DeVita, Hellman, and Rosenberg's Cancer: Principles & Practice of Oncology*, (Lippincott Williams & Wilkins, Philadelphia, 2008).
3. Skibber, J., Minsky, B. & Hoff, P. *Cancer of the colon*, (Lippincott Williams & Wilkins, Philadelphia, PA, USA, 2001).
4. Puli, S.R., *et al.* Meta-analysis and systematic review of colorectal endoscopic mucosal resection. *World journal of gastroenterology : WJG* **15**, 4273-4277 (2009).
5. Conio, M., *et al.* EMR of large sessile colorectal polyps. *Gastrointestinal endoscopy* **60**, 234-241 (2004).
6. Markle, B., May, E.J. & Majumdar, A.P. Do nutraceutics play a role in the prevention and treatment of colorectal cancer? *Cancer metastasis reviews* **29**, 395-404 (2010).
7. Landmann, R.G. & Weiser, M.R. Surgical management of locally advanced and locally recurrent colon cancer. *Clinics in colon and rectal surgery* **18**, 182-189 (2005).
8. Markowitz, S. & Bertagnoli, M. Molecular Basis of Colorectal Cancer. *The New England Journal of Medicine* **361**, 2449-2460 (2009).
9. Kanwar, S.S., Poolla, A. & Majumdar, A.P. Regulation of colon cancer recurrence and development of therapeutic strategies. *World journal of gastrointestinal pathophysiology* **3**, 1-9 (2012).
10. Powell, S.M., *et al.* APC mutations occur early during colorectal tumorigenesis. *Nature* **359**, 235-237 (1992).
11. Smith, G., *et al.* Mutations in APC, Kirsten-ras, and p53--alternative genetic pathways to colorectal cancer. *Proceedings of the National Academy of Sciences of the United States of America* **99**, 9433-9438 (2002).
12. Su, L.K., *et al.* Multiple intestinal neoplasia caused by a mutation in the murine homolog of the APC gene. *Science* **256**, 668-670 (1992).
13. Tseng, W., Leong, X. & Engleman, E. Orthotopic mouse model of colorectal cancer. *Journal of visualized experiments : JoVE*, 484 (2007).
14. Repici, A. & Tricerri, R. Endoscopic polypectomy: techniques, complications and follow-up. *Techniques in coloproctology* **8 Suppl 2**, s283-290 (2004).
15. Lujan, H.J., Plasencia, G., Jacobs, M., Viamonte, M., 3rd & Hartmann, R.F. Long-term survival after laparoscopic colon resection for cancer: complete five-year follow-up. *Diseases of the colon and rectum* **45**, 491-501 (2002).
16. Kusano, M., *et al.* Sentinel node mapping guided by indocyanine green fluorescence imaging: a new method for sentinel node navigation surgery in gastrointestinal cancer. *Digestive surgery* **25**, 103-108 (2008).
17. Charanya, T., *et al.* Trimodal color-fluorescence-polarization endoscopy aided by a tumor selective molecular probe accurately detects flat lesions in colitis-associated cancer. *Journal of biomedical optics* **19**, 126002 (2014).
18. Liu, Y., *et al.* Complementary fluorescence-polarization microscopy using division-of-focal-plane polarization imaging sensor. *Journal of biomedical optics* **17**, 116001 (2012).

19. Achilefu, S., *et al.* Synthesis, in vitro receptor binding, and in vivo evaluation of fluorescein and carbocyanine peptide-based optical contrast agents. *Journal of medicinal chemistry* **45**, 2003-2015 (2002).
20. Edwards, W.B., *et al.* Multimodal imaging of integrin receptor-positive tumors by bioluminescence, fluorescence, gamma scintigraphy, and single-photon emission computed tomography using a cyclic RGD peptide labeled with a near-infrared fluorescent dye and a radionuclide. *Molecular imaging* **8**, 101-110 (2009).
21. Achilefu, S., *et al.* Synergistic effects of light-emitting probes and peptides for targeting and monitoring integrin expression. *Proceedings of the National Academy of Sciences of the United States of America* **102**, 7976-7981 (2005).
22. Gruev, V., Perkins, R. & York, T. CCD polarization imaging sensor with aluminum nanowire optical filters. *Optics express* **18**, 19087-19094 (2010).
23. Powell, S.B. & Gruev, V. Calibration methods for division-of-focal-plane polarimeters. *Optics express* **21**, 21039-21055 (2013).
24. Gilboa, E., Cunningham, J.P., Nehorai, A. & Gruev, V. Image interpolation and denoising for division of focal plane sensors using Gaussian processes. *Optics express* **22**, 15277-15291 (2014).
25. Berezin, M.Y., *et al.* Rational approach to select small peptide molecular probes labeled with fluorescent cyanine dyes for in vivo optical imaging. *Biochemistry* **50**, 2691-2700 (2011).
26. Backman, V., *et al.* Detection of preinvasive cancer cells. *Nature* **406**, 35-36 (2000).
27. Gurjar, R.S., *et al.* Imaging human epithelial properties with polarized light-scattering spectroscopy. *Nature medicine* **7**, 1245-1248 (2001).
28. Hsiung, P.L., *et al.* Detection of colonic dysplasia in vivo using a targeted heptapeptide and confocal microendoscopy. *Nature medicine* **14**, 454-458 (2008).
29. Marten, K., *et al.* Detection of dysplastic intestinal adenomas using enzyme-sensing molecular beacons in mice. *Gastroenterology* **122**, 406-414 (2002).

Chapter 3

Intravenous, topical and oral administration routes for targeted molecular probe in colon cancer

Chapter 3 is primarily based on the administration routes that were explored utilizing the targeted molecular probe identified in Chapter 2. Under Dr. Samuel Achilefu's supervision, the routes that were explored include intravenous, a novel topical administration strategy and oral gavage. My contributions to this work included designing the experiments, developing the novel topical administration approach, carrying out the imaging studies involving the various administration routes, interpreting and analyzing data, and writing the manuscript. In this chapter, I discuss my work on the efficacy of administration strategies in identifying tumor along with the advantages and disadvantages associated with the various approaches. The chapter begins discussing the (i) intravenous approach, (ii) topical sol-gel approach, and (iii) oral gavage approach along with the shortcomings associated with each of them.

The effectiveness of contrast agents in probing molecular processes and functions in the cell depend on their efficiency of delivery to target tissues. Delivery of optical probes to the tissues have been known to be dictated by nonspecific mechanisms[1-4], specific mechanisms as well as nonspecific-followed by a secondary activated mechanism[5,6].

As for non-specific delivery, molecular probes primarily rely on differential accumulation of the probe in pathological tissue based on disrupted tissue capillary permeability or other structural aberrations. The retention of non-specific contrast agents in tumor is usually restricted in the cases of advanced tumor stages. Indocyanine green (ICG) has been shown in several occasions to be used as a blood-pool agent by imaging tumor vasculature in tumor xenografts[7], however it has been shown that ICG demonstrates sporadic uptake in different tumor xenografts, thereby making it a non-specific contrast agent[4]. Generally speaking, the low specificity and sensitivity of nonspecific optical contrast agent such as ICG limit their use as blood-pool agents for optical imaging of tumors.

Site-specific delivery mechanism takes advantage of optical molecular probes that can incorporate essential features of tumor pathogenesis to induce specific response in tumors. This takes advantage of specific characteristics of the tumor such as up-regulation of factors specific to tumor allowing to deliver contrast agent to specific target. Some characteristics that can be used for specific delivery include overexpressed receptors on tumor cell membranes, adhesion factors during angiogenesis, and tissue-specific markers for cancer to name a few. To achieve this, several carriers can be used including macromolecules, peptides, antibodies, and proteins that can mediate delivery of optical probes to tumors.

1. Intravenous approach

The peptide-based targeted molecular probe that has be identified by Achilefu et al.[8] makes an excellent blood-pool agent allowing for optimal tumor to muscle ratio at the 24-hour time point when injected intravenously. In order to demonstrate efficacy of the molecular probe towards colon cancer application using the intravenous, we developed an orthotopic HT-29 orthotopic model and utilize a spontaneous APC min model of colon cancer.

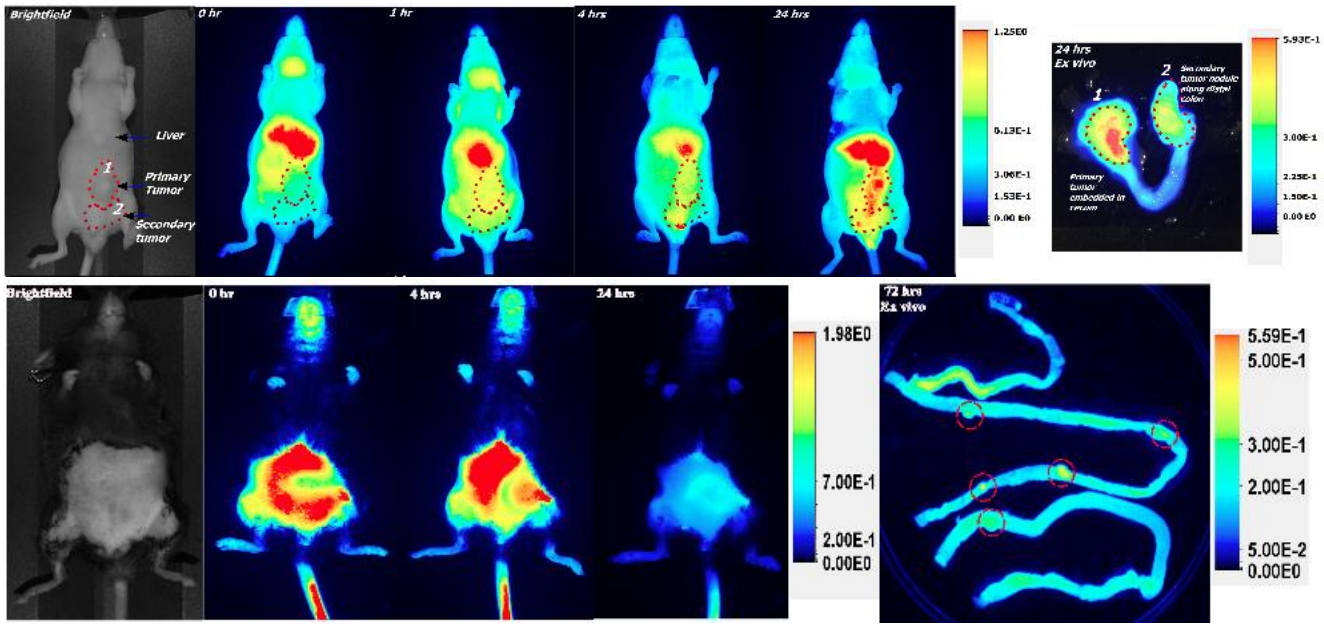

Figure 1. LS301 efficacy in HT-29 orthotopic model (top) and APC min model (bottom) *via* intravenous administration approach.

The intravenous approach demonstrated enhanced tumor-to-background ratio in both models 24 hours post administration when using a planar imaging system with high sensitivity. This served as an impetus to test intravenous approach in a more invasive, endoscopy setting for colitis-associated cancer. We developed an azoxymethane-dextran sodium sulfate (AOM-DSS)

model that best recapitulates colitis-associated cancer sequence. A NIR capable endoscope was developed (Figure 2) for carrying out endoscopy on AOM-DSS treated mice. Mice were administered with six nanomoles of LS301 24 hours prior to the procedure to provide optimal contrast.

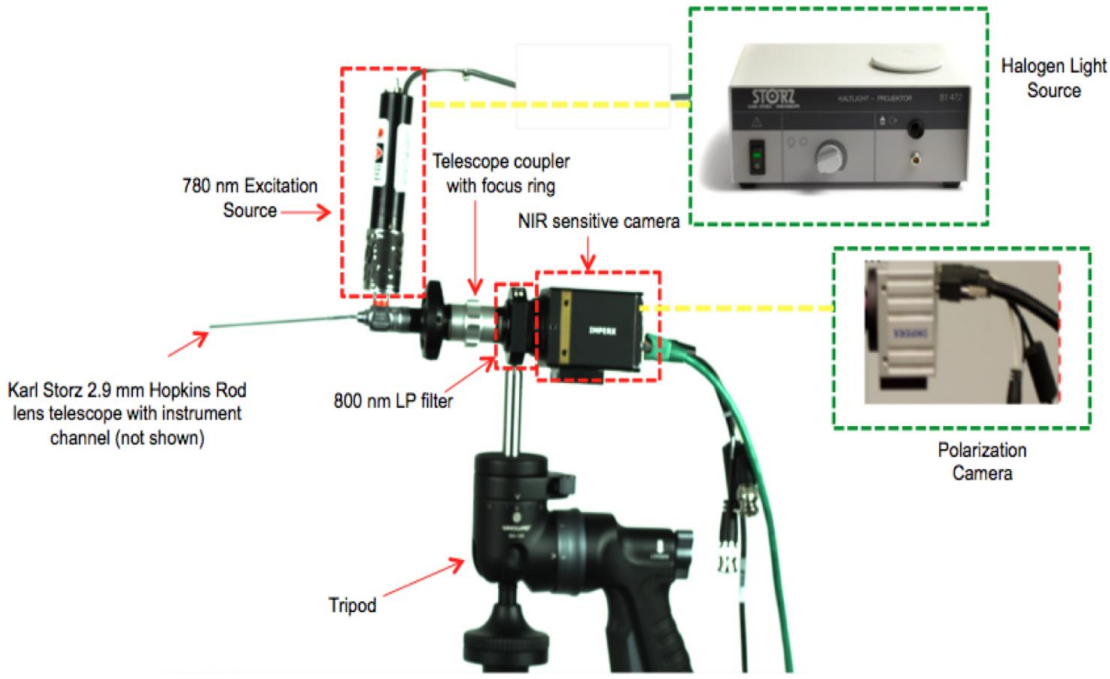

Figure 2. Endoscope setup used for color-fluorescence-polarization imaging of CAC lesions. The setup is fixed on a tripod to allow for minimal movements while switching modes. NIR Fluorescence mode requires a 780 nm excitation source and a NIR sensitive sensor at the distal end of the endoscope to capture images. Polarization mode requires a white light source and a polarization capable sensor that is discussed further in Chapter 4.

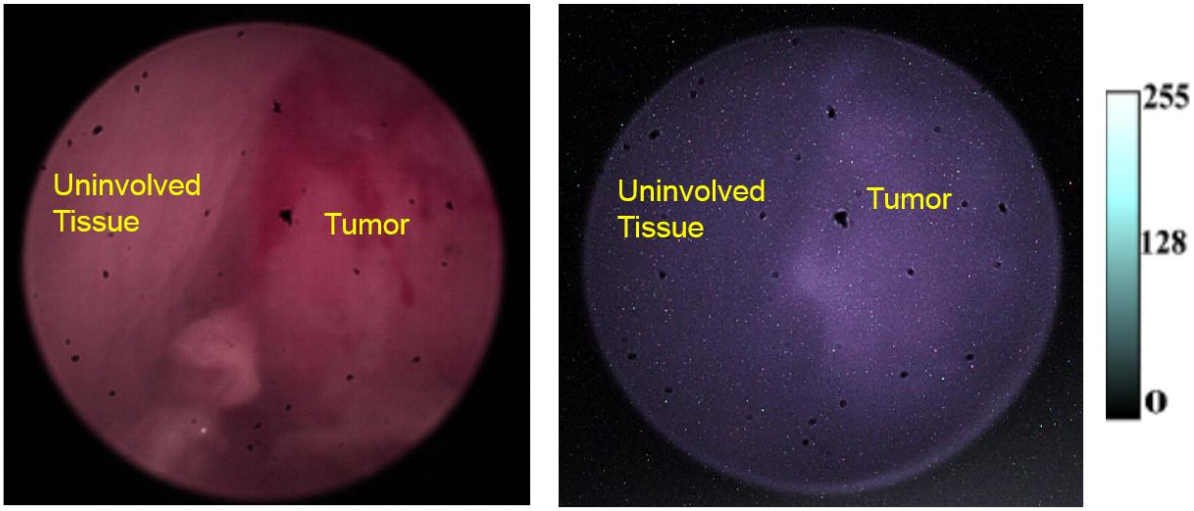

Figure 3. NIR endoscopy in AOM-DSS model captured at 5 frames per second. Tumor and surrounding uninvolved tissue are identified in both color (left) and NIR (right) images. Note that breathing artifacts integrated over five seconds result in imperfect co-registration.

LS301 demonstrated retention in the tumor with a tumor-to-background ratio (TBR) of 3.2 ± 0.4 as shown in Figure 3. The high integration time is attributed to utilizing a NIR sensitive camera that only has a quantum efficiency of 25% at 800 nm and using a light source that allows less than 5 mW/cm^2 of incident light at 780 nm. In order to demonstrate the real-time capability of the NIR endoscope system, we utilized a Karl Storz SPIES ICG system. The endoscope operates in color, auto fluorescence and NIR modes allowing for seamless transition between the modes. It provides 1920 x 1080 HD resolution scan with integrated parfocal zoom lens (focal length f = 15-31 mm). The three-chip camera head allows seamless integration of the three modes offered with the ability to provide HD resolution images. Furthermore, the D-light source developed by Karl Storz allows different excitations for color, autofluorescence and NIR modes. Excitation light in the NIR mode was however > 30 mW/cm^2 (over six fold greater than FDA

allowance for human use). Figure 4 presents the fluorescence spectra of the excitation source in various modes.

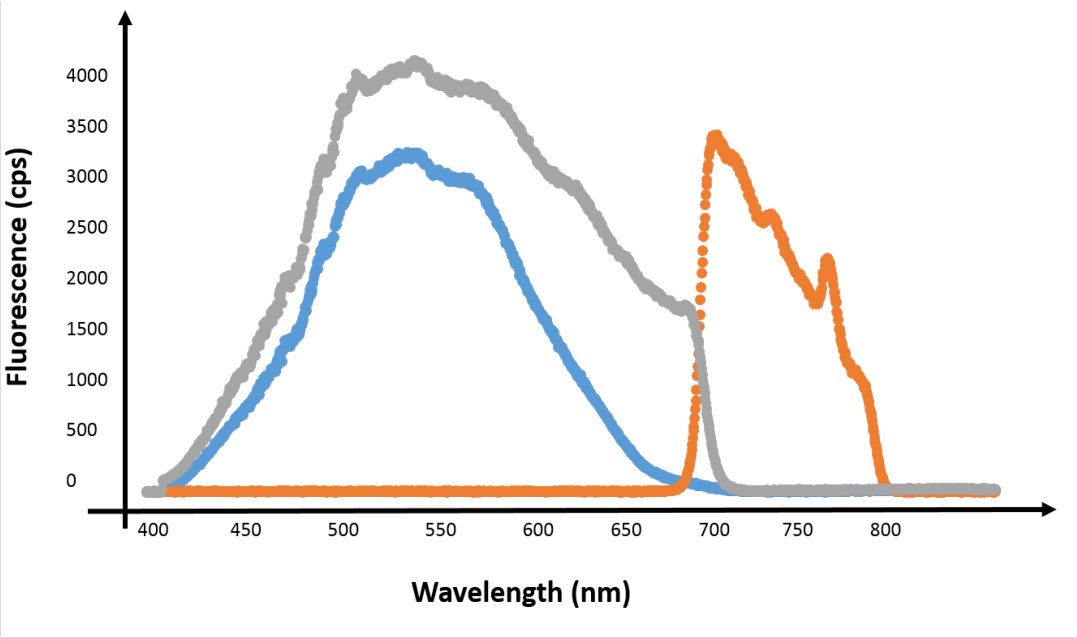

Figure 4. Fluorescence spectra in autofluorescence (blue), white (grey) and NIR (orange) modes.

The Karl Storz SPIES system was applied towards a subcutaneous prostate cancer model generated by implanting 10 million PNEC cells in the hind limb of the mouse. The tumor was allowed to grow for a week to form a small mass of 0.5 mm prior to imaging using the system. A simple skin-flap technique in the region of interest was sufficient to expose the hind limb site of implantation. Images were obtained in color and NIR modes where the two modes were swapped *via* a easy-to-use toggle switch. NIR images obtained provided an impressive TBR of 6.2 ± 1.2 as shown in Figure 4.

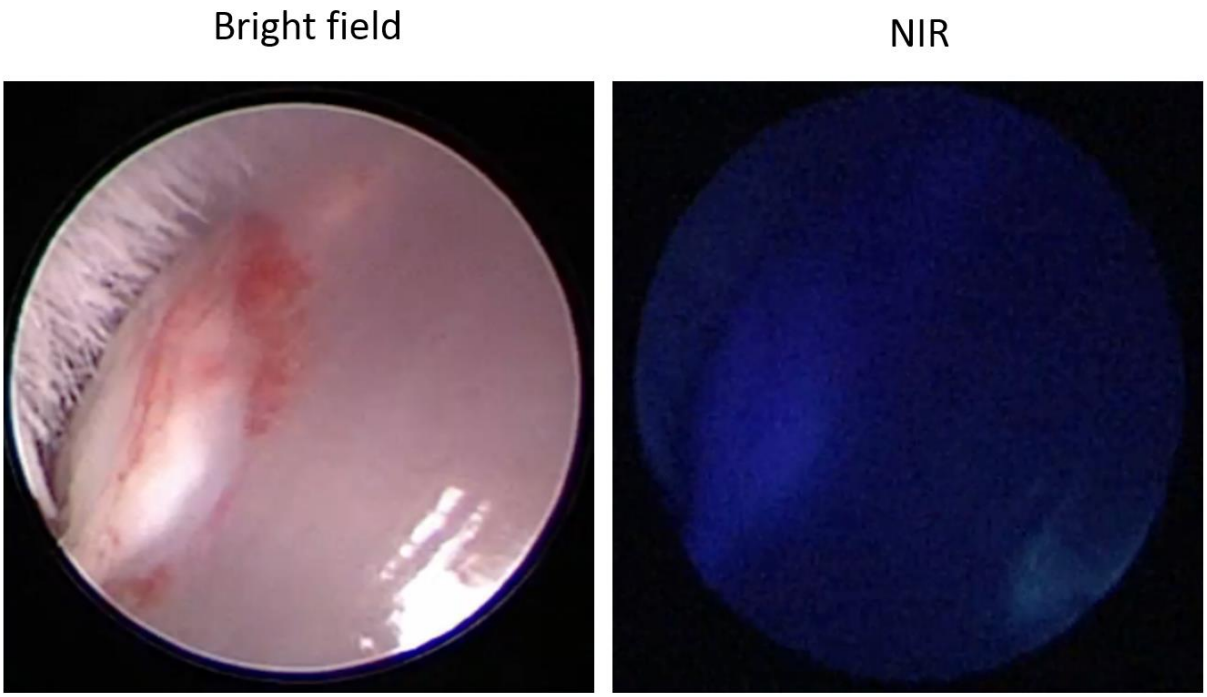

Figure 4. Real-time NIR endoscopy in subcutaneous prostate cancer model using Karl-Storz SPIES system

For detection of precancerous and cancerous lesions in CAC and SCC, the lesions are extremely small in size <0.5 mm usually and the probe accumulation in tumors is fairly minimal in volume and concentration (< 1 µM). Although the contrast between tumor and background is high, in order to do real-time NIR endoscopy, there is a need for a system with high detection sensitivity, high quantum efficiency sensor in the NIR regime and a powerful light source to illuminate with sufficient number of photons to withstand the transmission losses from within the rigid optics of the endoscope.

While the intravenous approach takes the greatest advantage of the dynamics associated blood-pool contrast agents, it does have some downsides. Intravenous administration of molecular probes leads to distribution in all organs in the body, making toxicity of the molecular probe a

valid concern. Furthermore, 24 hours for optimal contrast, would require the patient to come into the clinic a day before the procedure, increasing healthcare costs in the process.

2. Topical administration approach

With translatability in mind for colonscopy application, we explored the topical administration strategy. The inclusion of topical administration approach such as in the case of chromoendoscopy (CE) for diagnosis of lesions in ulcerative colitis has been widely debated[9]. CE using methylene blue has demonstrate potential in being able to identify pit patterns that are typically associated with low and high grade dysplasia[10].

We first explored the topical administration approach using LS301 on various stages of AOM-DSS induced colorectal cancer. Frozen tissue sections obtained from resected tumors were incubated with LS301 for an hour prior to being washed three times by PBS and imaged. Both carcinoma and dysplastic stages in CAC were investigated.

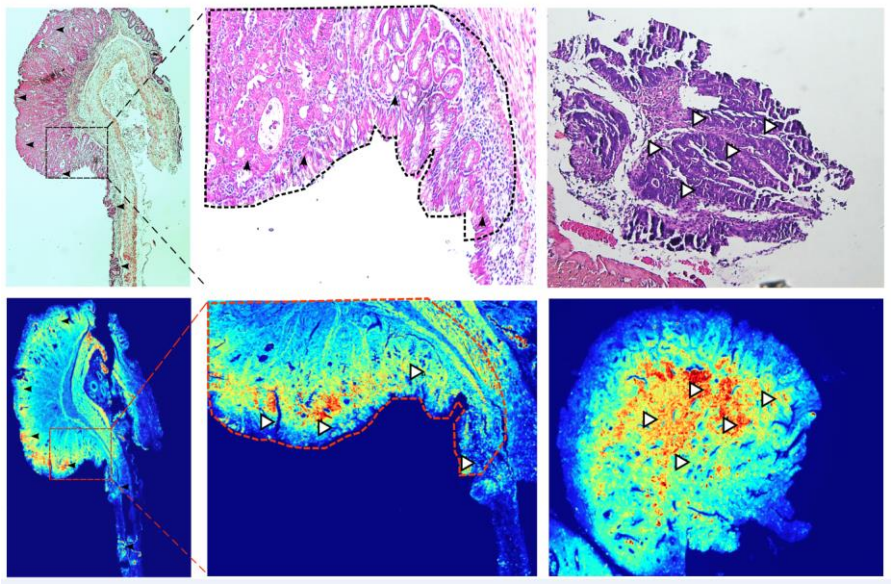

Figure 5. *Ex vivo* NIR fluorescence and corresponding H&E imaging of cancerous tissue from AOM-DSS model

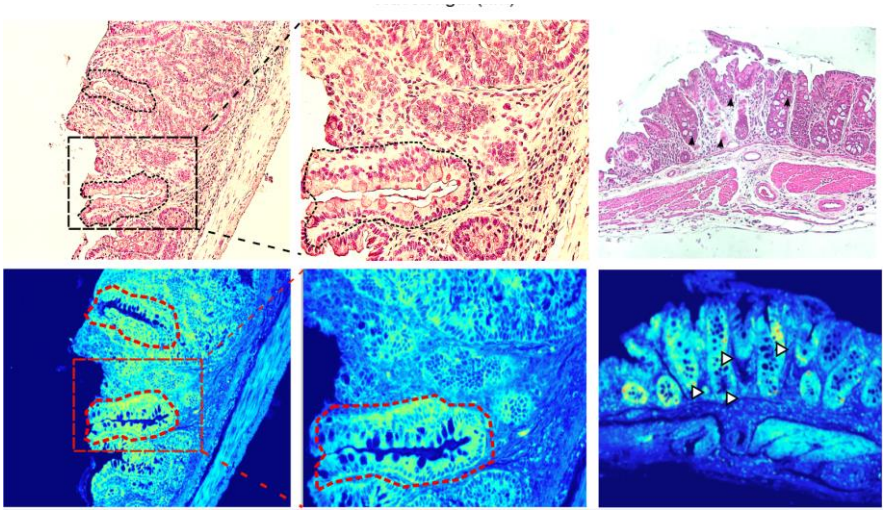

Figure 5. *Ex vivo* NIR fluorescence and corresponding H&E imaging of dysplastic tissue from AOM-DSS model

Preferential uptake of LS301 is observed in both dysplastic and cancerous tissues when compared to surrounding uninvolved tissue. Based on the selective uptake, we administered a formulation similar to intravenous administration described previously, topically. 60µM formulation of LS301 in PBS was injected *via* the instrument channel of the endoscope in the distal colon during an endoscopy procedure and post three washes, color and NIR imaging was conducted. Images obtained provided uneven uptake of LS301 throughout the colon and low NIR signal overall possibly due to two reasons; uneven distribution of LS301 sprayed on, and lack of "incubation time" with tissues which would allow for internalization and retention of LS301 in precancerous and cancerous tissues as shown in intravenous approach.

There was a clear need for an administration strategy that allowed even distribution of administered molecular probe and ample "incubation time" with all the surrounding tissue due to the serendipity associated with flat lesions. To address these concerns, we employed a sol-gel approach that allows the LS301 formulation to stay liquid at under a critical transition temperature and turn into a gel at room temperature or higher. Furthermore, in order to flush out the formulation from the colon post-incubation, we took advantage of its reversible nature of the sol-gel by flushing the colon with cold PBS, thereby allowing for the gel to transition back to liquid and exit the colon. Figure 6 demonstrates the overall process of topical administration that was used and Figure 7 demonstrates results obtained *via* this method in AOM-DSS model.

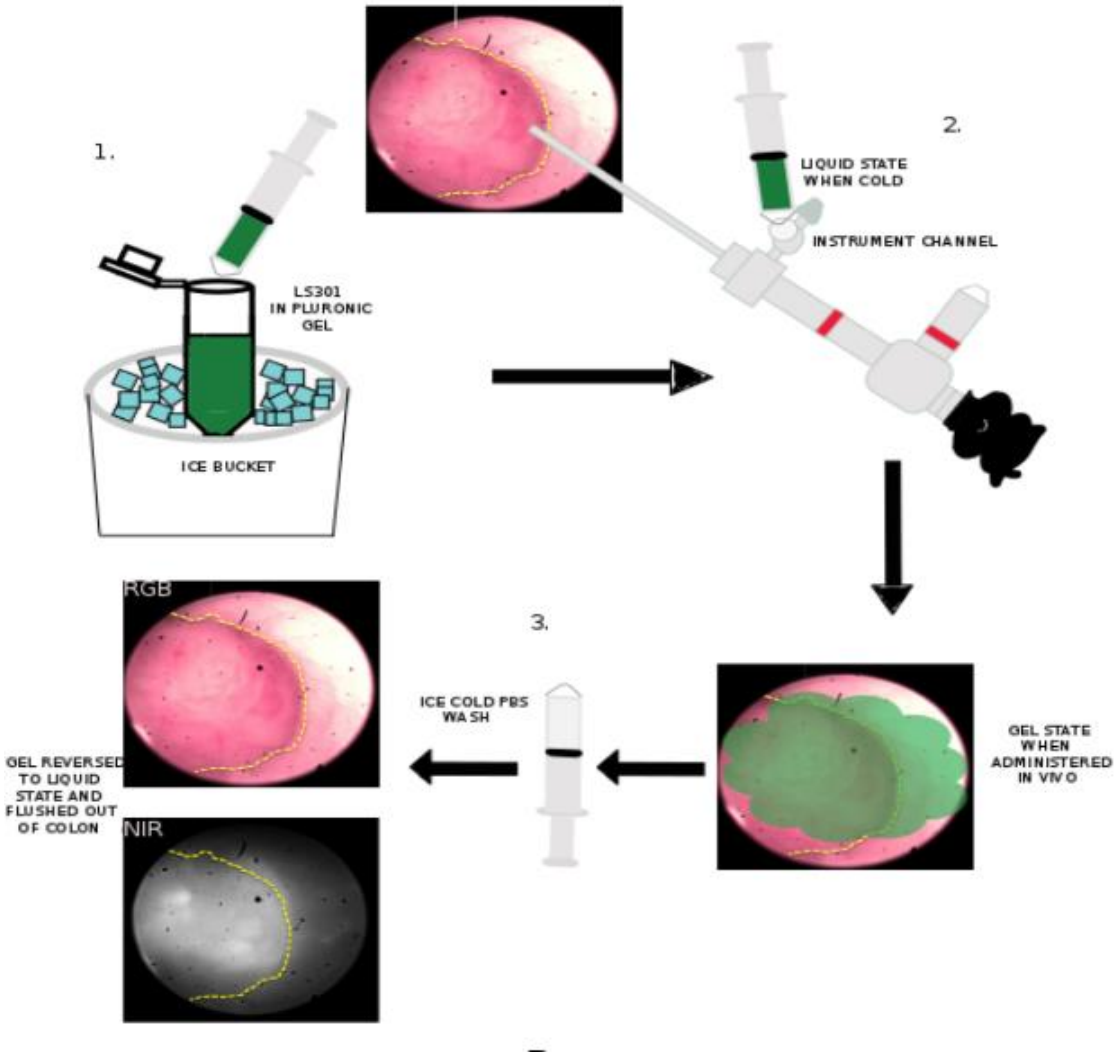

Figure 6. Topical administration strategy for colonscopy on live AOM-DSS treated mice. 1) Briefly a 25% w/v formulation of Poloxamer f127 (Sigma Aldrich, St. Louis) was used to dissolve 60uM LS301 solution and kept on ice at 4^0C to maintain liquid state prior to administering. 2) Solution was administered via instrument channel and allowed to incubate for ten minutes. 3) Cold PBS was used to flush the distal colon three times in order to reverse the phase of sol-gel formulation and wash out of colon prior to imaging.

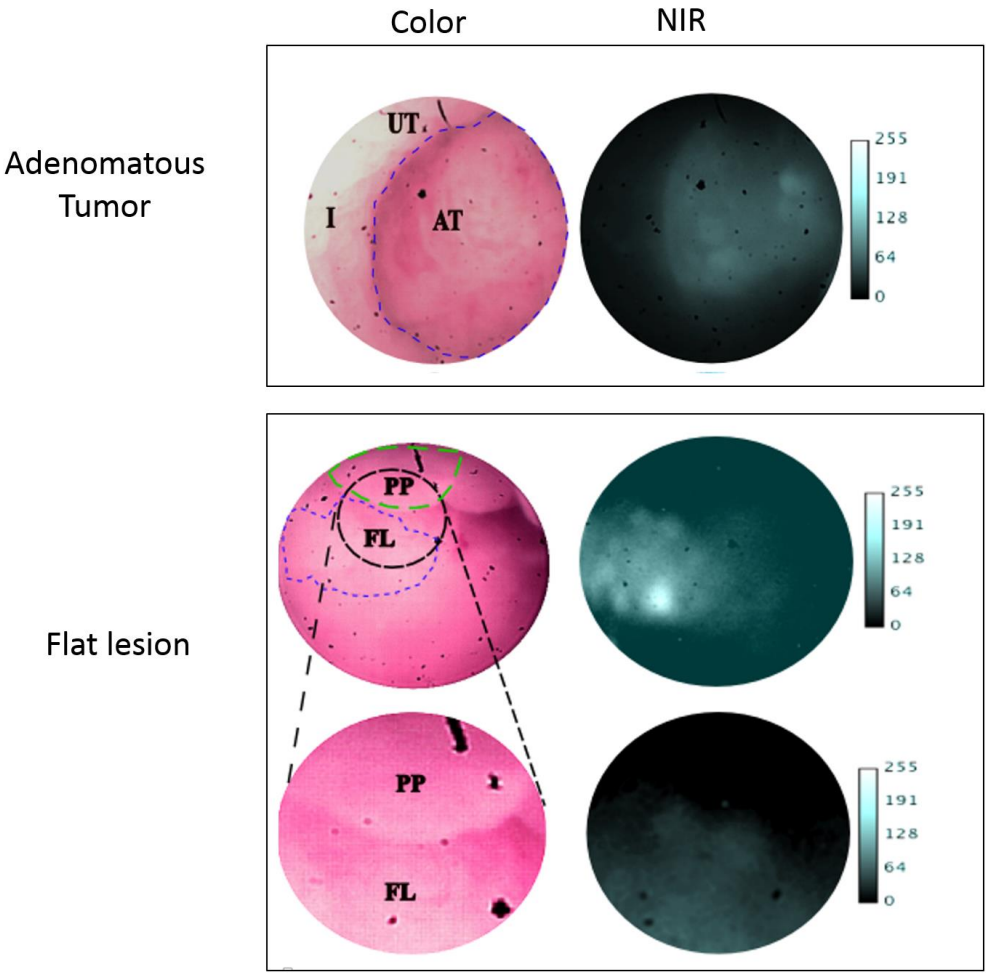

Figure 7. *In vivo* color-NIR endoscopy in AOM-DSS model of adenomatous tumor (top) and (flat lesion identified) and later verified *via* H&E (Chapter 4).

In vivo topical administration of sol-gel formulation provided a high contrast to noise ratio (CNR) in adenomatous tumors (20.6±1.65) and flat lesions (12.1±1.03) versus surrounding uninvolved colon tissue versus CNR of inflamed tissues (1.62±0.41). However, the sol-gel topical administration approach has its own limitations when considering translatability. The low transition temperature of 20^0C requires cold PBS (<15^0C) flushes to reverse the temperature and

allow for exit from the colon potentially resulting in great discomfort to the patient. That said, the sol-gel method allows us to fine tune the transition temperature based on the concentration of Pluronic f-127 used as shown in Figure 8. Furthermore, due to its viscous nature, the incubation time required could exceed that of a formulation composed of LS301 and PBS. Also, the topical administration approach has been known to increase the procedure time considerably given the need to repeatedly spray the formulation as the endoscopist moves along the colon in search for precancerous and cancerous lesions.

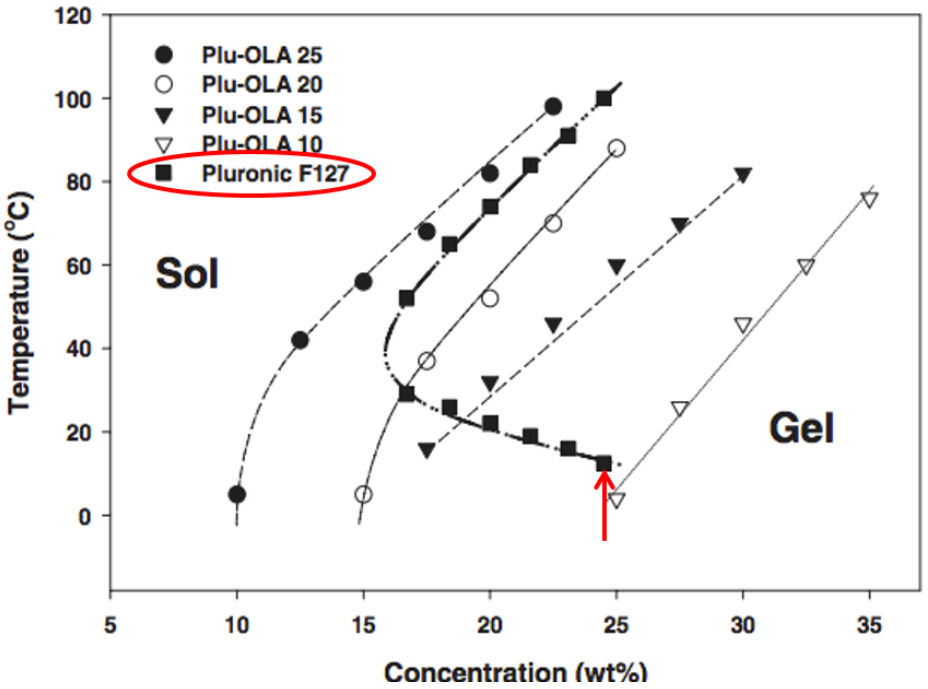

Figure 8. Transition temperature versus concentration relationship of pluronic F-127 (adapted from Lee et al.[11]

3. Oral gavage administration

The goal of exploring the oral gavage administration approach was to allow for a faster colonscopy procedure (major shortcoming of topical administration) while allowing for minimal change in routine colonscopy preparation. The formulation employed would be fairly easy-to-use as it could be simply incorporated into the dye mixture in the enema solution prior to the procedure. Also, compared to the intravenous approach, the oral gavage approach is semi-targeted, restricting the probe distribution strictly to the digestive system.

In order to test this approach, we developed an orthotopic colon cancer model by injecting 500,000 Ht-29 tumor cells in the cecal wall of nude mice. The tumors were allowed to grow for two weeks to give us a small lesion. The diet is altered in these mice to increase the likelihood of fecal matter-free colon and provide minimal obstruction for the administered dye to interact with the tissue. Figure 9 shows a general schematic explaining the timing of dietary changes introduced during the procedure. We administered 120 μM of LS301 orally using a gavage syringe and imaged the mice over a 72 hour period to test clearance prior to sacrificing the mice and exteriorizing the intestine and cecum. Figure 10 shows a general schematic explaining the different time points the mice were imaged in relation to the diet.

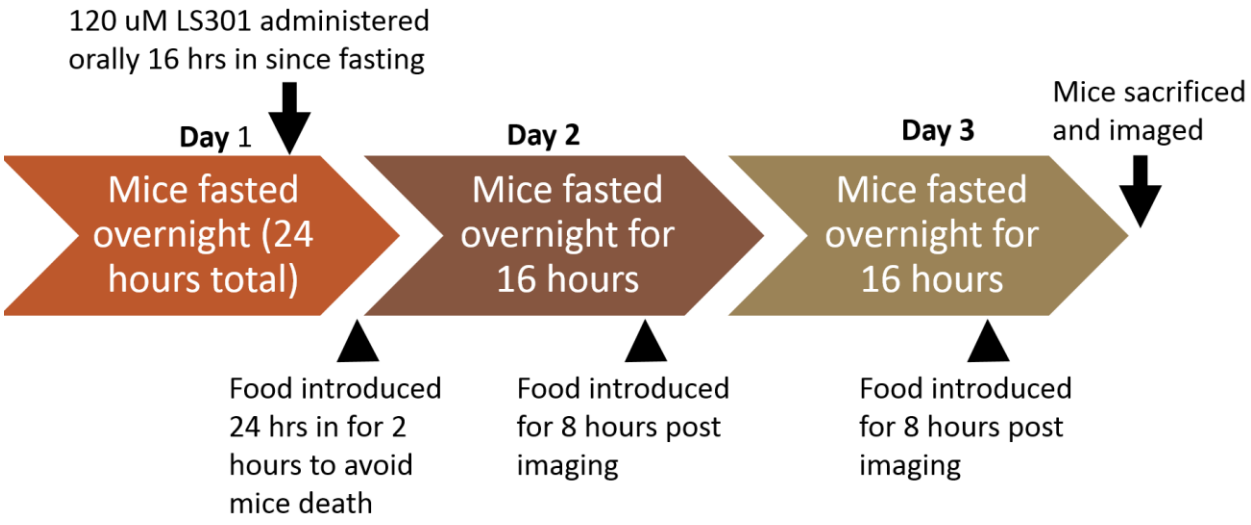

Figure 9. Diet pattern followed prior to and after the administration of LS301

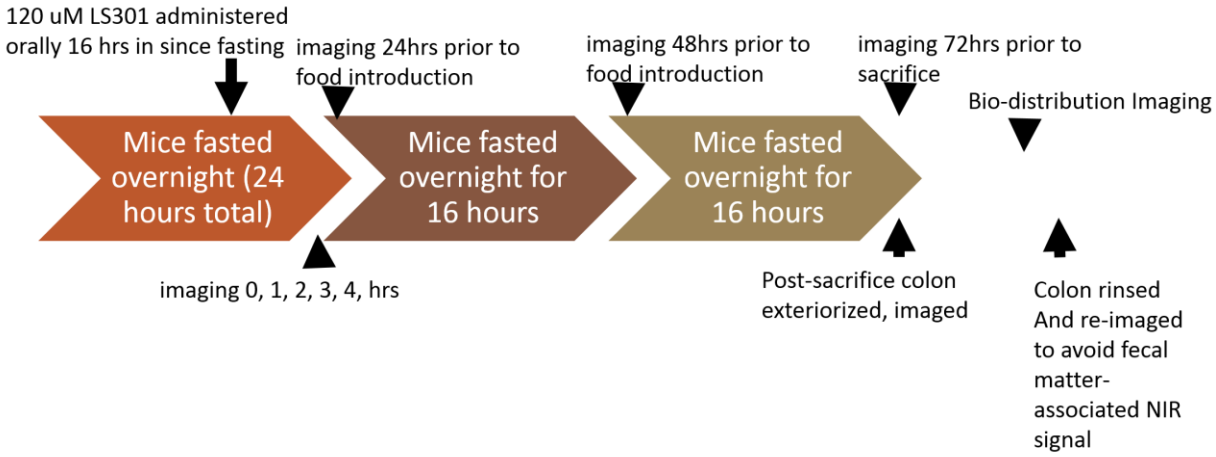

Figure 10. Administration and imaging time points post administration

Mice (with no tumors) were used as controls for this experiment and were imaged over a course of 72 hours prior to exteriorizing the cecum and imaging the inoculated sites as shown in Figures 11 and 12.

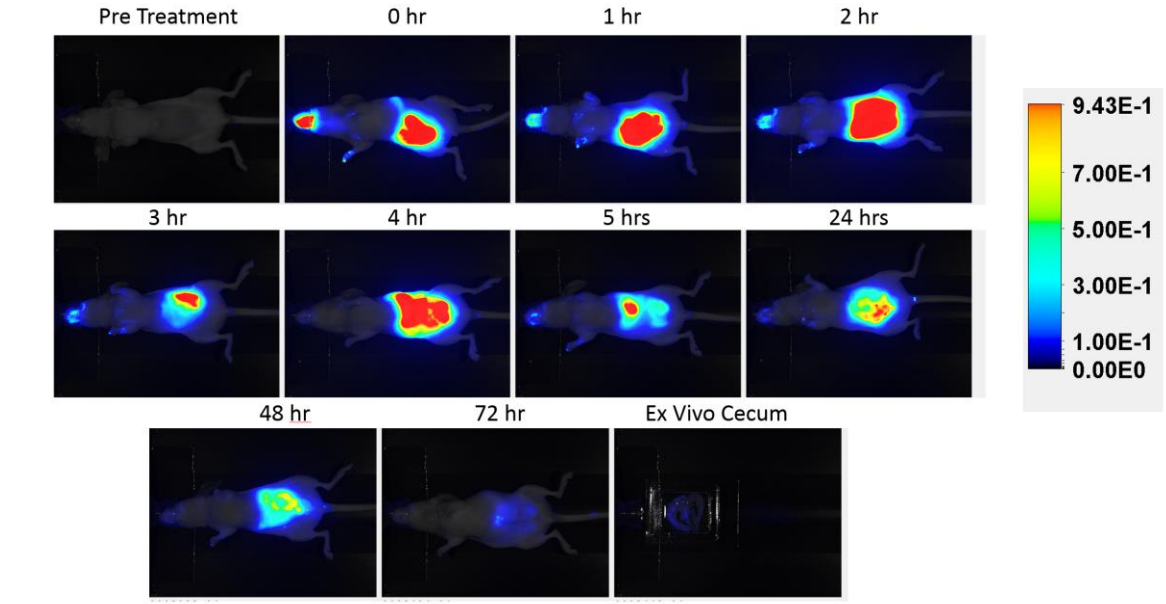

Figure 11. *In vivo* imaging in control (no-tumor) mice over 72 hours. Cecum is exteriorized 72 hours post administration and associated fluorescence intensity was examined.

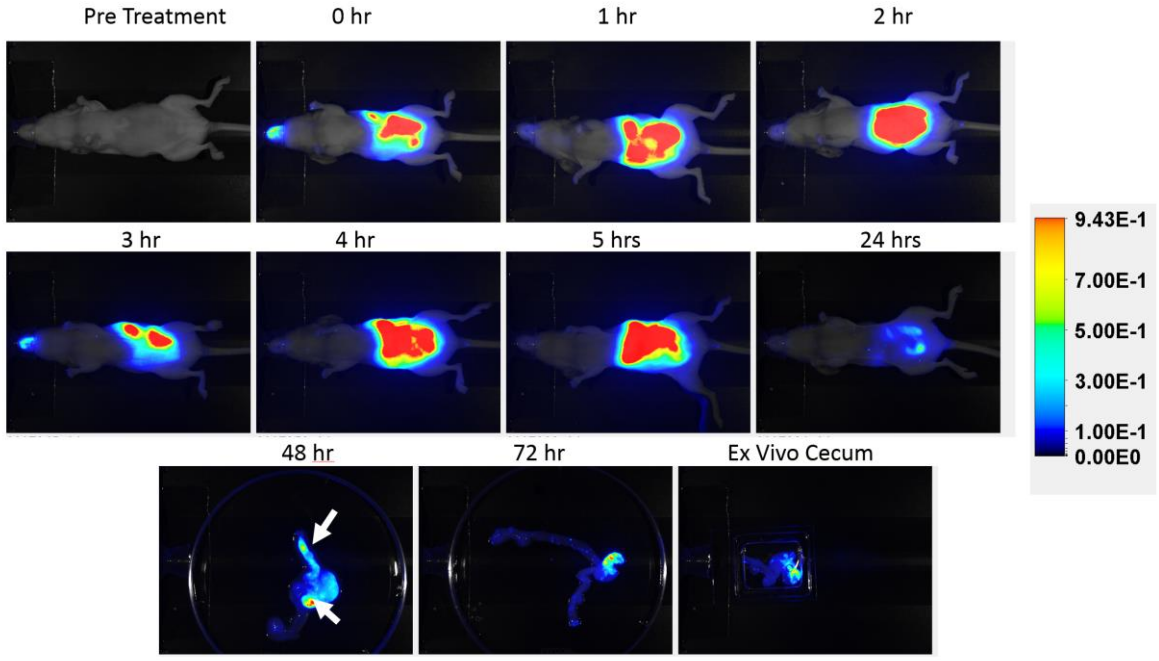

Figure 12. *In vivo* imaging in tumor mice over 72 hours. Cecum is exteriorized 72 hours post administration and associated fluorescence intensity was examined.

The implantation sites of tumor demonstrate an enhanced LS301 uptake as shown by the arrows in Figure 12. Furthermore, to ensure the LS301 distribution stays restricted to the digestive tract, we conducted a biodistribution study post-sacrifice where we measured the fluorescence intensity associated with various organs in the body such as skin, muscle, brain, blood, heart, lungs, spleen, kidney and liver (as shown in Figure 13).

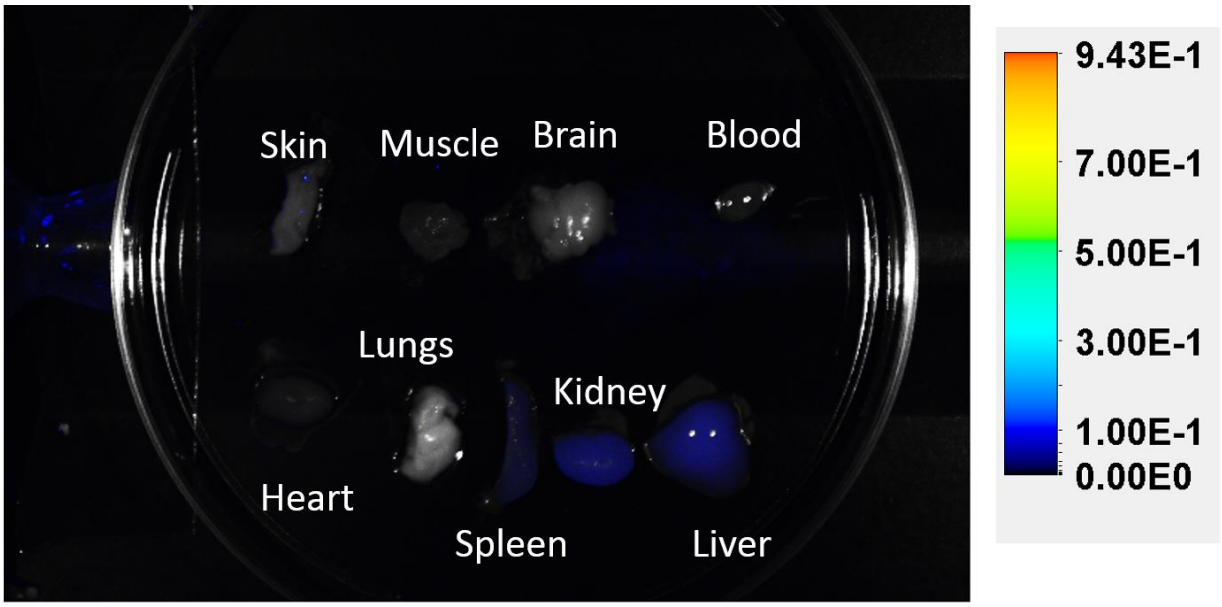

Figure 13. A bio-distribution study 72 hours post administration demonstrating clearance of LS301 from all the major organs

Although we observed enhanced specificity towards tumor in the cecum, we further validated stability of our peptide-based molecular probe under different pH conditions that it would be subjected to while passing through the stomach. Figure 14 demonstrates stability results of LS301 obtained under three different conditions, pH = 1.0, 4.0, and 7.4.

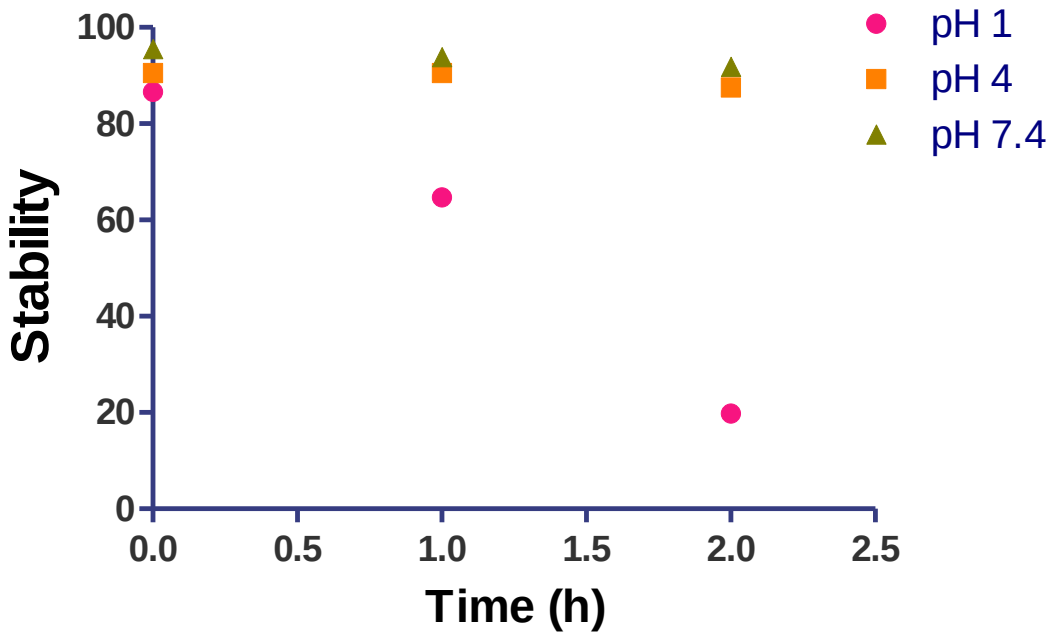

Figure 14. pH stability test of LS301 over time

References

1. Hawrysz, D.J. & Sevick-Muraca, E.M. Developments toward diagnostic breast cancer imaging using near-infrared optical measurements and fluorescent contrast agents. *Neoplasia* **2**, 388-417 (2000).
2. Ntziachristos, V., Yodh, A.G., Schnall, M. & Chance, B. Concurrent MRI and diffuse optical tomography of breast after indocyanine green enhancement. *Proceedings of the National Academy of Sciences of the United States of America* **97**, 2767-2772 (2000).
3. Sevick-Muraca, E.M., Houston, J.P. & Gurfinkel, M. Fluorescence-enhanced, near infrared diagnostic imaging with contrast agents. *Current opinion in chemical biology* **6**, 642-650 (2002).
4. Achilefu, S., Dorshow, R.B., Bugaj, J.E. & Rajagopalan, R. Novel receptor-targeted fluorescent contrast agents for in vivo tumor imaging. *Investigative radiology* **35**, 479-485 (2000).
5. Bremer, C., Tung, C.H., Bogdanov, A., Jr. & Weissleder, R. Imaging of differential protease expression in breast cancers for detection of aggressive tumor phenotypes. *Radiology* **222**, 814-818 (2002).
6. Weissleder, R., Tung, C.H., Mahmood, U. & Bogdanov, A., Jr. In vivo imaging of tumors with protease-activated near-infrared fluorescent probes. *Nature biotechnology* **17**, 375-378 (1999).
7. Chen, L.H. & Guan, J. [Three-dimensional conformal radiation therapy for malignant tumors (report of 1,024 cases)]. *Di 1 jun yi da xue xue bao = Academic journal of the first medical college of PLA* **22**, 853-855 (2002).
8. Achilefu, S., *et al.* Synergistic effects of light-emitting probes and peptides for targeting and monitoring integrin expression. *Proceedings of the National Academy of Sciences of the United States of America* **102**, 7976-7981 (2005).
9. Ullman, T.A. Should chromoendoscopy be the standard of care in ulcerative colitis dysplasia surveillance? *Gastroenterology & hepatology* **6**, 616-620 (2010).
10. Jung, M. & Kiesslich, R. Chromoendoscopy and intravital staining techniques. *Bailliere's best practice & research. Clinical gastroenterology* **13**, 11-19 (1999).
11. Lee, S.Y., Tae, G. & Kim, Y.H. Thermal gellation and photo-polymerization of di-acrylated Pluronic F 127. *Journal of biomaterials science. Polymer edition* **18**, 1335-1353 (2007).

Chapter 4

Trimodal color-fluorescence-polarization endoscopy aided by a tumor selective molecular probe accurately detects flat lesions in colitis-associated cancer

Chapter 4 is a reformatted version of a published manuscript: “Tauseef Charanya, Timothy York, Viktor Gruev, Samuel Achilefu et al. Trimodal color-fluorescence-polarization endoscopy aided by a tumor selective molecular probe accurately detects flat lesions in colitis-associated cancer.” Under Dr. Samuel Achilefu’s supervision, my contributions to this work included designing the experiments, developing fluorescence-polarization endoscope, carrying out the imaging studies involving AOM-DSS model, interpreting and analyzing data, and writing the manuscript. In this Chapter, I discuss my work in the development of a fluorescent-polarization endoscope for identification of flat and adenomatous tumors in a CAC murine model utilizing a NIR targeted probe.

Abstract

Colitis-associated cancer (CAC) arises from premalignant flat lesions of the colon, which are difficult to detect with current endoscopic screening approaches. We have developed a complementary fluorescence and polarization reporting strategy that combines the unique biochemical and physical properties of dysplasia and cancer for real time detection of these lesions. Using azoxymethane-dextran sodium sulfate (AOM-DSS) treated mice, which recapitulates human CAC and dysplasia, we show that an octapeptide labeled with a near infrared (NIR) fluorescent dye selectively identified all precancerous and cancerous lesions. A new thermoresponsive sol-gel formulation allowed topical application of the molecular probe during endoscopy. This method yielded high contrast-to-noise ratios (CNR) between adenomatous tumors (20.6±1.65) and flat lesions (12.1±1.03) and surrounding uninvolved colon tissue versus CNR of inflamed tissues (1.62±0.41). Incorporation of nanowire-filtered polarization imaging into NIR fluorescence endoscopy shows high depolarization contrast in both adenomatous tumors and flat lesions in CAC, reflecting compromised structural integrity of these tissues. Together, the real-time polarization imaging provides real-time validation of suspicious colon tissue highlighted by molecular fluorescence endoscopy.

1 Introduction

Inflammatory Bowel Diseases (IBDs) consist of ulcerative colitis and Crohn's disease, which are characterized by uncontrolled inflammation of the gastrointestinal tract in genetically susceptible individuals exposed to environmental risk factors.[1] The incidence and prevalence of IBD has increased in recent years, affecting 1.4 million Americans in 2012 alone.[2] Moreover, peak onset of this disease occurs in the second and third decades of life, subjecting these patients to a two-fold or greater lifetime risk of developing colorectal cancer (CRC) than normal subjects.[2] A meta-analysis of colorectal cancer risk suggests a cumulative incidence of malignancy of 2% by 10 years, 8% by 20 years and 18% by 30 years post diagnosis.[1] Sporadic CRC and colitis-associated cancer (CAC) together account for 52,000 mortalities every year in the United States alone, making them the second leading causes of death from cancer among adults.[3]

Unlike sporadic CRC, which develops from an adenomatous polyp, CAC follows a dysplasia-carcinoma sequence where the inflamed mucosa gives rise to flat and polypoid dysplasia that lead to invasive cancers.[4, 5] The lack of an elevated growth component, as exists in polyps, creates an enormous challenge to detect these flat lesions during surveillance colonoscopy. For example, 50-80% of the lesions that are missed during surveillance colonoscopy are flat.[6, 7] Several murine models have been developed to recapitulate human CAC.[8] In particular, the azoxymethane-dextran sodium sulfate (AOM-DSS) model has been used to demonstrate that advanced cancers develop from flat lesions without transitioning through a polypoid intermediate.[9] Although dysplasia could serve as a marker for malignancy in colitis patients, current surveillance protocols fail to reliably identify early stages of CAC.[10]

Recent advances in biomarker and imaging platforms have focused on either morphological or molecular features of these flat lesions, neither of which is sufficient to aid diagnosis of these pathologies in-real time during colonoscopy. Efforts to identify polyps and cancerous lesions using chromoendoscopy, virtual chromoendoscopy, narrow-band imaging, and post processing algorithms such as i-SCAN and FICE have failed to reliably delineate flat lesions from surrounding uninvolved tissue.[11-14] In particular, chromoendoscopy is currently recommended for routine surveillance of IBD patients. Although this technique has improved the detection rates of flat lesions from 28% to 56%,[15] the fraction of undetected lesions remains unsatisfactory. Similarly, optical coherence tomography (OCT) has been used to differentiate diseased from normal esophageal tissue, but the inhomogeneous back scattering of signal in high-grade dysplasia limits the diagnostic information derived from this approach.[16, 17] To improve detection sensitivity, newer fluorescence endoscopic techniques such as confocal laser endomicroscopy, have been developed. In conjunction with fluorescence contrast agents, these techniques allow visualization of molecular signatures of cancer but lack a real-time validation strategy and provide only a limited field of view.[18-20]

The overarching goal for this study is to develop and validate a tri-modal endoscopic system consisting of fluorescence, polarization, and color modules for colonoscopy. The color imaging module provides conventional visual feedback of the anatomical structures of tissue. Utilizing a NIR fluorescent molecular reporter of flat lesions, the fluorescence module highlights underlying pathologies that are not visible by conventional color imaging method. Complementary polarization signal highlights tissue that is largely opaque to both fluorescence and color modules,

thereby facilitating full characterization and instant cross-validation of suspicious lesions. An unprecedented high sensitivity and specificity approaching 100% were obtained by combining these three imaging modalities.

2 Materials and Methods

2.1 Using unpolarized light for polarization endoscopy

Both incident and reflect light are fully described by the Stokes vectors, which contain four parameters; S_0, S_1, S_2, and S_3. The first Stokes parameter, S_0, describes the intensity of the light; the second Stokes parameters, S_1, describes the difference between horizontal and vertically polarized light; the third Stokes parameter, S_2, describes the difference between 45 and 135 degree polarized light; and the fourth Stokes parameter, S_3, describes the difference between left and right circularly polarized light. The polarization of light changes upon reflection from a surface, with the change based on the reflection geometry and the medium and surface materials. The Mueller matrix in Equation 1 mathematically describes the change in polarization for a reflection from a tissue,

$$\mathrm{M}_{ref} = \frac{1}{2}\left(\frac{\tan\Theta_x}{\sin\Theta_y}\right)^2 \begin{bmatrix} \cos^2\Theta_x + \cos^2\Theta_y & \cos^2\Theta_x - \cos^2\Theta_y & 0 & 0 \\ \cos^2\Theta_x - \cos^2\Theta_y & \cos^2\Theta_x + \cos^2\Theta_y & 0 & 0 \\ 0 & 0 & -2\cos\Theta_x\Theta_y & 0 \\ 0 & 0 & 0 & -2\cos\Theta_x\Theta_y \end{bmatrix}$$

where Θ_x is difference in the incident and refracted angles ($\Theta_x = \theta_i - \theta_r$), and Θ_y is the sum of the incident and refracted angles ($\Theta_y = \theta_i + \theta_r$). Snell's Law (Equation 2) relates the incident and refracted angles

$$n_1 \sin\theta_i = n_2 \sin\theta_r$$

where θ_i is the incident angle, θ_r as the refracted angle, and n_1 and n_2 are the indexes of the media and object, respectfully. Multiplying the incident Stokes vector with the Mueller matrix for reflection (Equation 3) results in the Stokes vector for light reflected off of the surface.

$$\begin{bmatrix} S_0 \\ S_1 \\ S_2 \\ S_3 \end{bmatrix}_{REF} = \mathrm{M}_{ref} \begin{bmatrix} S_0 \\ S_1 \\ S_2 \\ S_3 \end{bmatrix}_{INPUT}$$

The reflected Stokes vector contains all information needed to compute the Degree of Linear Polarization (DoLP) for the reflected light (Equation 4). The DoLP measures how linearly polarized the light becomes after reflection, from 0 (no linear polarization) to 1 (completely linearly polarized).

$$DoLP_{REF} = \frac{\sqrt{S_{1,REF}^2 + S_{2,REF}^2}}{S_{0,REF}}$$

The Angle of Polarization (AoP) measures the orientation of the reflected light with respect to the detector, and is computed from S_1 and S_2 (Equation 5).

$$AoP_{REF} = \frac{1}{2}\arctan\left(\frac{S_{2,REF}}{S_{1,REF}}\right)$$

If the input Stokes vector is unpolarized light [1,0,0,0], the DoLP of the reflected light becomes (Equation 6)

$$DoLP_{REF} = \frac{\cos^2 Q_x - \cos^2 Q_y}{\cos^2 Q_x + \cos^2 Q_y}$$

and the reflected AoP is zero, as the reflected S_2 component is zero. This applies only to a planar reflection. On a three dimensional surface, the azimuthal angle is modeled as a rotation of the axis of the planar reflection of a microfacet of the surface into the axis of the sensor by a rotation angle ϕ. Using the Mueller matrix of a rotation (Equation 7),

$$\mathrm{M}_{rot}(2\phi) = \begin{bmatrix} 1 & 0 & 0 & 0 \\ 0 & \cos 2\phi & \sin 2\phi & 0 \\ 0 & -\sin 2\phi & \cos 2\phi & 0 \\ 0 & 0 & 0 & 1 \end{bmatrix}$$

the reflection equation becomes (Equation 8)

$$\begin{bmatrix} S_0 \\ S_1 \\ S_2 \\ S_3 \end{bmatrix}_{REF} = \mathrm{M}_{rot}(-2\phi)\mathrm{M}_{ref}\mathrm{M}_{rot}(2\phi)\begin{bmatrix} S_0 \\ S_1 \\ S_2 \\ S_3 \end{bmatrix}_{INPUT}$$

The reflected DoLP remains unchanged, however, the AOP becomes equal to the amount of curvature (Equation 9).

$$AOP = \frac{1}{2}\arctan\left(\frac{\frac{1}{4}\left(\cos^2\Theta_x - \cos^2\Theta_y\right)\csc^2\Theta_y \sin 2\phi \tan^2\Theta_x}{\frac{1}{4}\left(\cos^2\Theta_x - \cos^2\Theta_y\right)\csc^2\Theta_y \cos 2\phi \tan^2\Theta_x}\right) = \frac{1}{2}\arctan\left(\frac{\sin 2\phi}{\cos 2\phi}\right) = \phi$$

$$DOLP = \frac{4\ n_2 \sin^2(\Theta_i)cos(\Theta_i)\sqrt{1-\frac{\sin^2(\Theta_i)}{n_2^2}}}{n_2{}^2\cos(2\Theta_i)+2\ sin^4\Theta_i - 2sin^2\Theta_i cos^2\Theta_i + n_2^2}$$

2.2 *Synthesis of Polarization filter*

The fabrication of the nanowire polarization filter was conducted at the fabrication facilities at Washington University in St. Louis in collaboration with Moxtek Inc. (Orem, UT). The nanofabrication of the optical nanowire polarization filter was achieved by first depositing a

70 nm thin film of aluminum, followed by a 30 nm thin film deposition of SiO_2 using e-beam evaporation. A 100 nm thin layer of photoresist S-1805 was spun coated at 3000 rpm and baked at 115^oC for 60 seconds. A continuous-wave single frequency Nd:YAQ laser with 532 nm wavelength was used together with a frequency-doubler to produce coherent light waves at 266 nm wavelength. Two continuous-wave 266 nm wavelengths were aligned to interfere at 110^o and produce an interference pattern with a period of 140 nm. The interference pattern was transferred to the photoresist by exposing the sample for 40 seconds. After developing the photoresist, the pattern was transferred to the SiO_2 using the standard RIE/ICP etching recipe for SiO_2. The SiO_2 was used as a hard mask for etching the aluminum. The aluminum was etched for 150 seconds using 30 sccm BCl_3, 15 sccm Cl_2, 10 mTorr pressure, 70^oC temperature, 100 W RIE power and 150 W ICP power. The procedure was repeated four times and the sample was rotated by 45^o each time to produce nanowires with four different orientations. The nanowire polarization filters were flip chip bonded to a commercially available CCD imaging sensor (Kodak KAI 2020).

2.3 *Fluorescence and Polarization Endoscope*

The new endoscopic device shown in Fig. 2a is capable of imaging in three different modes: RGB, fluorescence, and polarization. In the RGB mode, an endoscopic cold light fountain (Xenon Nova 175; Karl Storz, Tuttlingen, Germany) with adjustable light intensity was used as the light source. The light cable was coupled to the illumination channel on a 0^0 Hopkins (1.9 mm x 10 cm) straightforward telescope (Karl Storz, Tuttlingen, Germany), as shown in Fig. 2a. Images were captured by an NIR-sensitive CCD camera (Fluorvivo; INDEC Biosystems) with an RGB Bayer filter. A telescope coupler with a focus ring (Karl Storz, Tuttlingen, Germany) focused the CCD camera on the image formation plane at the back of the telescope.

In the fluorescence mode, the cold light fountain source was replaced by a 100 mW, 780 nm excitation source (Lasermax, New York, USA). An 800 nm long-pass emission filter (ThorLabs, Newton, New Jersey) was placed behind the telescope in a slit of a custom-made adapter designed to couple the macro lens to the telescope. Images were captured using the Fluorvivo CCD camera equipped with a Sony ICX285 sensor (quantum efficiency of 30% at 800 nm).

In the polarization mode, the same endoscopic cold light fountain used as the light source for the RGB imaging was utilized here. Images were captured using the camera housing the polarization sensor described earlier.

2.4 *Polarization Endoscopy Calibration*

Since the endoscope is composed of a series of optical elements, the polarization state of the input light can be modified as the light travels though the endoscope. Every optical element in the endoscope will perturb the Stokes vector of the incident light and these perturbations need to be carefully examined to ensure that the endoscope preserves the polarization signatures of the incident light. We created an optical setup to evaluate the polarization properties of the endoscope as depicted in Figure 4a. The setup is composed of a polarization state generator and a polarization state analyzer.

The polarization state analyzer for the light emerging from the endoscope is measured using a division of time polarimeter. The polarimeter is composed of a zero-order precision wave plate (Newport 20RP34-514.5) with a quarter wave retardance at 514.5 nm, a precision linear polarizer (Newport 20LP-VIS-B) with a wavelength range of 400 – 700 nm and a USB controlled optical

power meter (Thorlabs PM100D) with visible spectrum calibrated photodiode (Thorlabs S120V). This instrument quantifies the Stokes vector as described by equations (1) through (4):[23]

$$S_0 = \frac{1}{2}\left(I(0^\circ, 0^\circ) + I(45^\circ, 0^\circ) + I(90^\circ, 0^\circ) + I(135^\circ, 0^\circ)\right) \quad (1)$$

$$S_1 = I(0^\circ, 0^\circ) - I(90^\circ, 0^\circ) \quad (2)$$

$$S_2 = I(45^\circ, 0^\circ) - I(135^\circ, 0^\circ) \quad (3)$$

$$S_0 = S_0 - 2I(45^\circ, 90^\circ) \quad (4)$$

In these equations, $I(\theta, \phi)$ is the intensity of the optical beam, θ describes the linear polarizer transmission axis angle in degrees and ϕ describes the wave plate retardance, which is 90º for the wave plates. To measure $(45^\circ, 90^\circ)$, the light beam passes through a waveplate with the fast axis along the *x*-axis and then through a linear polarizer with transmission axis rotated at 45º; to measure $I(\theta, 0)$ the beam passes through a linear polarizer with its transmission axis rotated θ degrees and then through waveplate with its fast axis along the x-axis. Hence, all measurements are done with both linear polarization filter and a quarter wave plate to take into account any optical losses that can occur in either optical element.

2.5 *Formulation of LS301*

The near-infrared dye LS301, which was reported previously,[21] was synthesized in our lab via modification of a previously described method.[24] LS301 consists of a near-infrared fluorescent dye, cypate (780 $_{ex}$/ 830 $_{em}$), and a cyclic peptide sequence, D-Cys-Gly-Arg-Asp-Ser-Pro-Cys-Lys (c($_D$CGRDSPC)K). Fig. 3a shows the molecular structure, absorption, and emission spectra of LS301.

To formulate LS301 in sol-gel mixture for topical administration, Pluronic F-127 (1 g; Sigma Aldrich, St. Louis, MO) was dissolved in phosphate buffered saline (10 mL; PBS) to obtain a 10% (w/v) stock solution. A solution of LS301 (0.5 mL; 60 μM) was dissolved in 10% w/v aqueous Pluronic solution to form the sol-gel system, which was stored on ice prior to administration to maintain its liquid state.

2.6 *In vivo Small Animal Endoscopy*

Mice were anesthetized via intraperitoneal injection of a solution of ketamine (85 mg/kg) and xylazine (15 mg/kg). They were then placed supine on a z-translation stage prior to the procedure. To avoid unnecessary movements of the endoscope during mode switches and to assess a region of interest within the same field of view, the imaging setup was immobilized on a tripod. To obtain 1 mm translation inside the colon, the endoscope was set on an x-y translation stage. The rigid endoscope could reach as far as 4 cm into the mouse colon, at which point it encountered the splenic flexure.

Prior to topical administration of the LS301 solution, the mouse colon was rinsed with PBS to remove debris and mucous. A novel administration technique enabled interaction of the mouse tissue with our molecular agent for a longer incubation time than would otherwise be achievable. A cold solution of the LS301 in Pluronic F127 sol-gel (0.5 mL) was injected carefully via the examination sheath of the endoscope. The solution turned into a gel instantaneously along the distal colon. After 10 minutes of incubation, cold PBS was flushed through the examination sheath to reverse the gel into a liquid state. After thorough rinsing of the colon with 3-5 PBS washes, fluorescence and polarization endoscopy were performed. Steps involved in this process are illustrated in Fig. 2b.

2.7 In situ fluorescence-polarization imaging

Post endoscopy, mice were sacrificed and the distal colon was isolated from the peritoneum without dislodging it from the animal to locate tumors that were identified during fluorescence-polarization endoscopy. A 780 nm excitation source illuminated the sample for fluorescence imaging and an 800 nm long pass filter was placed in front of the image capture device. Images were captured with an exposure time of 0.5 seconds. Polarization imaging was obtained using the system described above.

3 Results

3.1 Simulating unpolarized light in reflectance polarization endoscopy

3.1.1 Simulating reflectance imaging using unpolarized light source for polarization endoscopy

Most polarization methods typically use a polarization filter to illuminate a tissue and an orthogonal polarization filter placed at the detector side to measure polarization contrast information. This imaging modality requires careful optical alignment of the polarization filters and is applicable for microscopy or ex-vivo imaging. Due to space constraints in an endoscope, polarization contrast imaging is challenging. In this study, we allowed the intrinsic properties of tissue to linearly polarize the incident unpolarized light and back scattering to depolarize the reflected light, which is captured by our polarization sensor as shown in Fig. 1a. To ensure that this polarization technique is sensitive to differences in tissue properties, simulations using Muller calculus for reflection and Monte Carlo simulations for back scattering were performed (see below) using tissue refractive index values previously reported in literature. Diseased tissues have lower refractive index (1.39) than healthy tissue (1.46), thereby serving as an imaging biomarker for polarization imaging platform. Given the importance of angle of incidence, DoLP signature

arising from healthy and diseased tissues was plotted against the incidence angle using both Frenel's reflectance and Monte Carlo simulations as shown in Fig. 1b and an imaging angle of 15^{o} for *in vivo* endoscopy. At 15^{0}, we obtained ~4% DoLP difference between healthy and diseased tissue, which is sufficient to delineate normal from diseased tissue. While standard endoscopy procedures range in angles of imaging between 15-35^{0}, our *ex vivo* imaging setup utilized a 35^{0} angle, which results in a DoLP change of 20% between healthy and diseased tissue according to Fig. 1b. Based on differences in tissue refractive indexes, radius and density of nuclei, absorption coefficient between healthy and diseased tissue[25, 26] and back scattering of light, we illustrate the propagation of light in the two stages of CAC development: adenomatous polyp and flat, depressed lesions, respectively This simulation demonstrates that the polarization method is capable of cross-validating CAC and associated flat lesions in real time, guided by enhanced fluorescence in pathologic tissue.

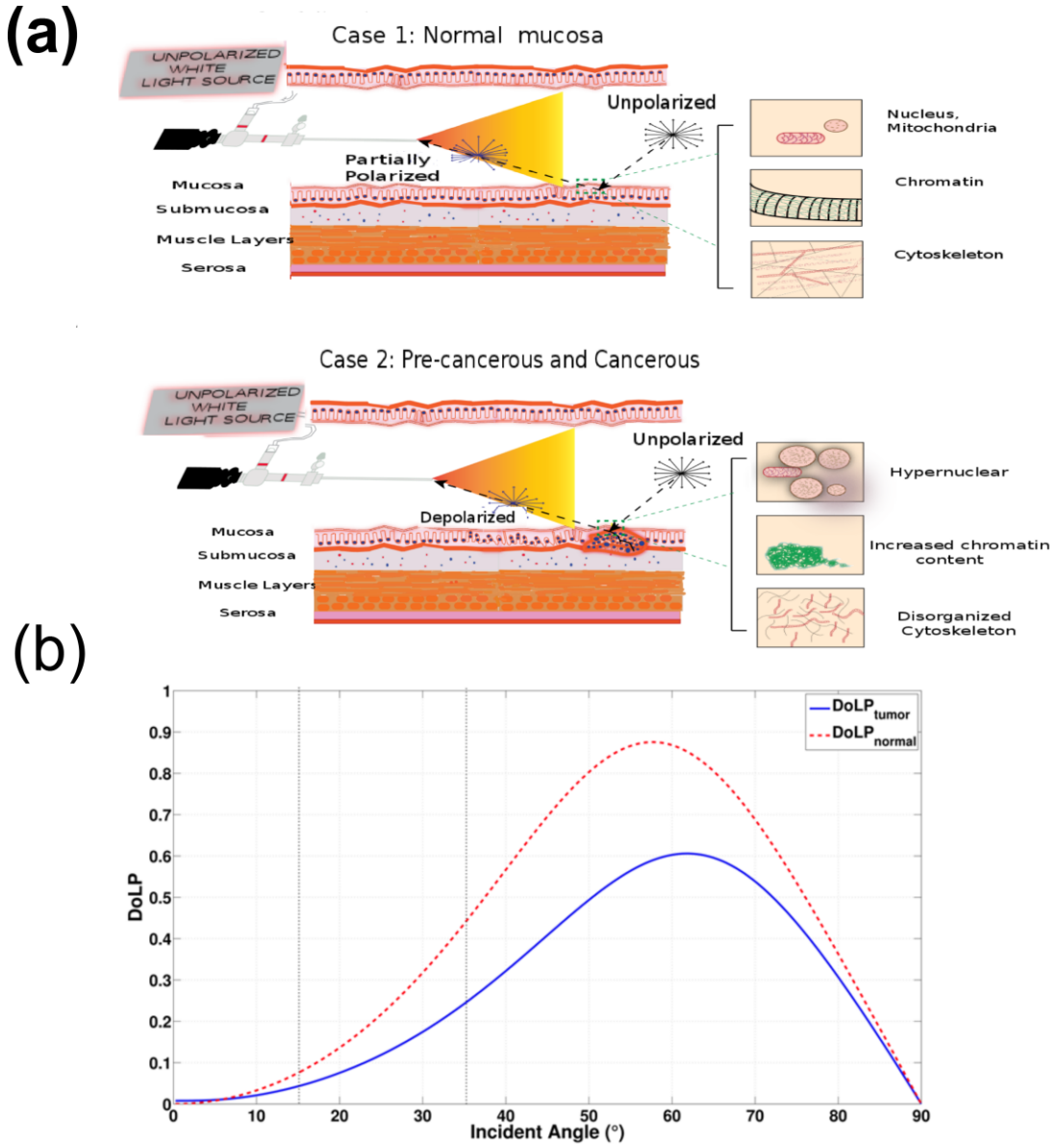

Fig. 1. Concept of reflectance imaging using unpolarized light. (a)Case 1 illustrates the propagation of light in healthy mucosa. Unpolarized light illuminates the region of colon under investigation. Light returning back from the wall of the colon interacts with the healthy mucosa as shown, and gets partially polarized prior to detection in a tissue composition dependent manner. Cytoskeletal organized actin fibers partially polarize the light. Case 2 illustrates the propagation of light in a flat, depressed lesion. Unpolarized light reflected from the wall of the colon interacts with pathologic tissue, which depolarizes the light. Larger and denser nuclei serve as source of scatterers in cancer cells, which favors depolarization. (b) A plot of Degree of Linear Polarized (DoLP) light versus incident angle of 0^0 straightforward endoscope. Reflected light from tumor tissue (blue) and healthy tissue (red) is modeled using both

Frenel's reflectance and Monte Carlo simulations. Dotted vertical black lines serve as a comparative tool for DoLP signature at 15^0 (*in vivo* studies) and 35^0 (*ex vivo* studies).

3.1.2 Simulating unpolarized light for polarization endoscopy

To ensure that this polarization technique is sensitive to differences in tissue properties, simulations using Muller calculus for reflection and Monte Carlo simulations for back scattering were performed. The difference in polarization signatures is due to a combination of Fresnel reflectance and backscattered intensity from the unpolarized source. The incident, unpolarized light becomes partially polarized upon reflection as shown in Fig. 1a. The partially polarized light mixes with the backscattered intensity from the tissue and further depolarizes the incident light, due to the optical parameters of the tissue. Assuming that scattering comes mostly from the nucleus, backscatter is simulated as a dispersion of spheres with optical properties similar to those of the nucleus, performed using the algorithm reported previously.[27] In tumor tissue, scattering comes mostly from the large sized, dense nuclei, whereas in uninvolved tissue, scattering arises primarily from scatterers associated with the mucosa and submucosa regions. Verification is done using polarized Monte Carlo simulation software with a poly-disperse set of scatterers drawn from a uniform distribution. In order to simulate the differential optical parameters arising from tumor versus unhealthy tissue, differences in nuclear radii, density of nuclei, index of refraction of nuclei, and absorption coefficient were considered and obtained from literature.[28-31] Perelman et al. have successfully extracted valuable information about the density and size distribution of mucosal cells and used them as indicators of disease state (neoplastic precancerous changes in biological tissue). Increase in size and density of nucleus is associated with a later diseased state in these studies. Furthermore, this is supported by Backman, et al. Studies conducted illustrate the higher level of backscattered light associated with a denser and larger nuclei concentration. This leads the

polarization state of reflected light to be more depolarized when compared to healthy tissue comprising of uniformly distributed, less dense, smaller nuclei.

We took a similar approach in modeling backscattered intensity as the combination of backscatter from the mucosa added to the backscatter from the submucosa after propagation back through the mucosa.[26] Since the light used was a 6000K Xenon source, the simulations take place at wavelengths between 400nm and 700nm in 25nm increments, normalized to the intensity of the bulb at these wavelengths. Increase in backscatter from the tumor tissue effectively depolarizes the Fresnel reflected DoLP, resulting in a lower measured DoLP for tumor when compared to the surrounding uninvolved region**.**

3.2 *Development of trimodal color, fluorescence, and polarization endoscope*

The goal of the instrument development was to retain the features of widely used clinical endoscopes while incorporating new reporting strategies for enhanced diagnosis of endoscope-accessible organs. Toward this goal, we developed a novel endoscope that is capable of presenting imaging data in color (RGB), NIR fluorescence, and polarization modes. Color colonoscopy is the standard of care, while NIR fluorescence and polarization provide new reporting signals for a molecularly targeted imaging agent and tissue pathophysiology, respectively. A detailed description of the endoscopy procedure is available in *Methods (In vivo small animal endoscopy)***.** Briefly, a rigid Hopkins endoscope fitted with a xenon lamp and a 780 nm laser served as RGB/polarization and NIR light sources, respectively, as shown in Fig. 2a and Fig. 2b. We used a visible/NIR-sensitive CCD camera with an RGB Bayer filter and 25% quantum efficiency at 800 nm to capture both color and NIR images.

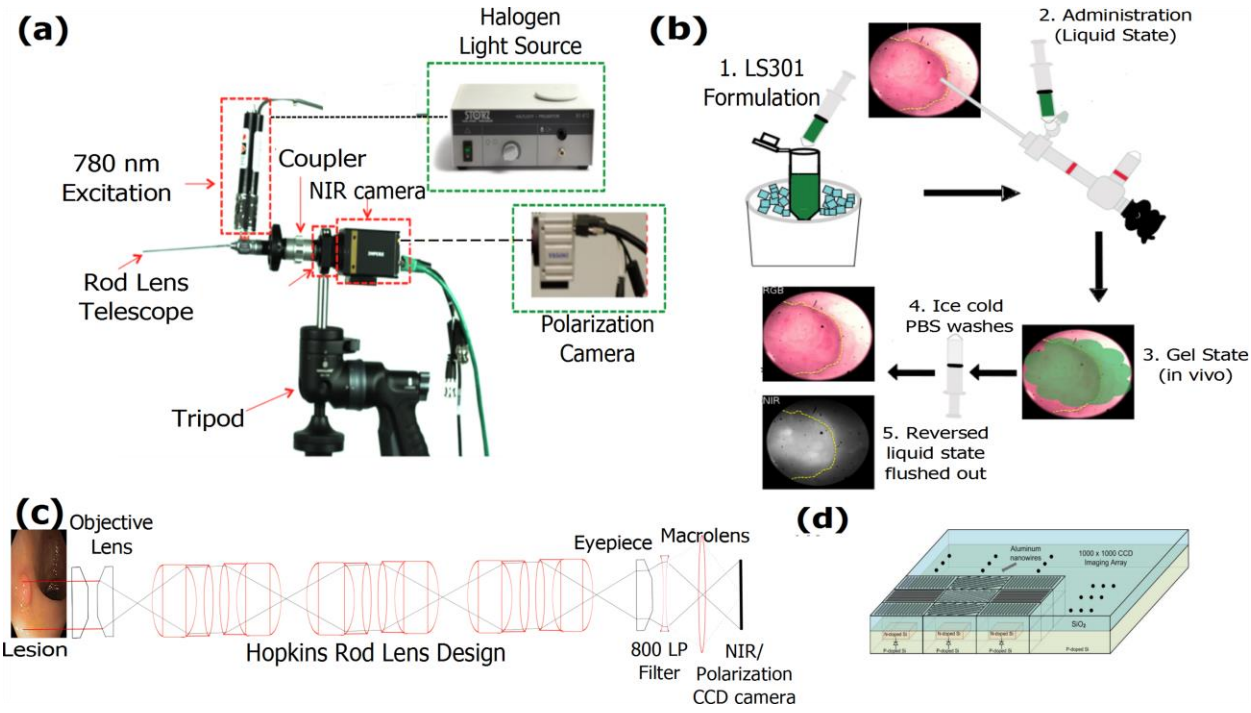

Fig. 2: Trimodal color-fluorescence- polarization endoscopy utilizing a novel molecular probe administration approach. (a) Endoscope setup used to perform white light, fluorescence and polarization endoscopy. A telescope coupler with a focus ring was used to focus the image onto the image formation plane located at the back of the Karl Storz telescope lens. For white light endoscopy, Xenon Nova 175 was used as a light source and a CCD camera (Fluorvivo) with an RGB Bayer filter was used. In NIR- fluorescence mode, a 100 mW 780 nm laser excitation source (inset I) was coupled to the light source channel on the endoscope. An 800 nm long pass emission filter was placed behind the telescope, as shown in the figure. A CCD camera with NIR capabilities (Fluorvivo) was utilized to capture images in NIR-fluorescence mode. In polarization mode, the Xenon broadband light source was used along with a custom made polarization camera, as shown in inset II. The entire setup was fixed on a tripod and an X-Y translation stage was utilized for finer adjustments to avoid causing damage to the walls of the colon. (b) Steps involved in the dye administration method utilizing Pluronic F127 gel formulation. (c) Schematic of the light path associated with the endoscopy setup presented in (A). (d) Polarization sensor consisting of an imaging array arranged in blocks of four (two-by-two) superpixels. Each superpixel consists of four pixels that are composed of nano-wire polarization filters with the transmission axis oriented at 0^0, 45^0, 90^0, and 135^0. These nanowires are 70 nm wide, 140 nm tall, and spaced 140 nm from center to center.

3.2.1 Real time polarization imaging

To capture the light polarization information, a division of the focal plane polarization imaging sensor was developed, where the incoming light was filtered *via* a polarization filter array consisting of four nanowire polarization filters offset by 45^0 prior to absorption by a silicon photodiode as shown in Fig. 2d.[32, 33] The amplitude of the filtered light wave was recorded by photodetectors underneath the aluminum nanowire polarization filters. The tissue was illuminated with unpolarized light *via* the light port of a Karl Storz rigid endoscope and the reflected light was collected *via* our custom-built polarization sensor. The polarization state of the reflected light from the tissue was determined by both the relative position of the camera and the index of refraction of the imaged tissue, (Equation 4). The use of an unpolarized light source simplified the imaging setup and allowed the intrinsic morphological and physiological properties of the tissue to dictate the captured polarization signature. This imaging method differs from typical polarization contrast imaging, where linear polarized illumination is used to illuminate a tissue and a detector with cross linear polarization is used to record the reflected light. Due to complex alignment requirements of the polarization filters on both the illumination and detection components, application of traditional polarization contrast imaging is limited for *in vivo* endoscopy.

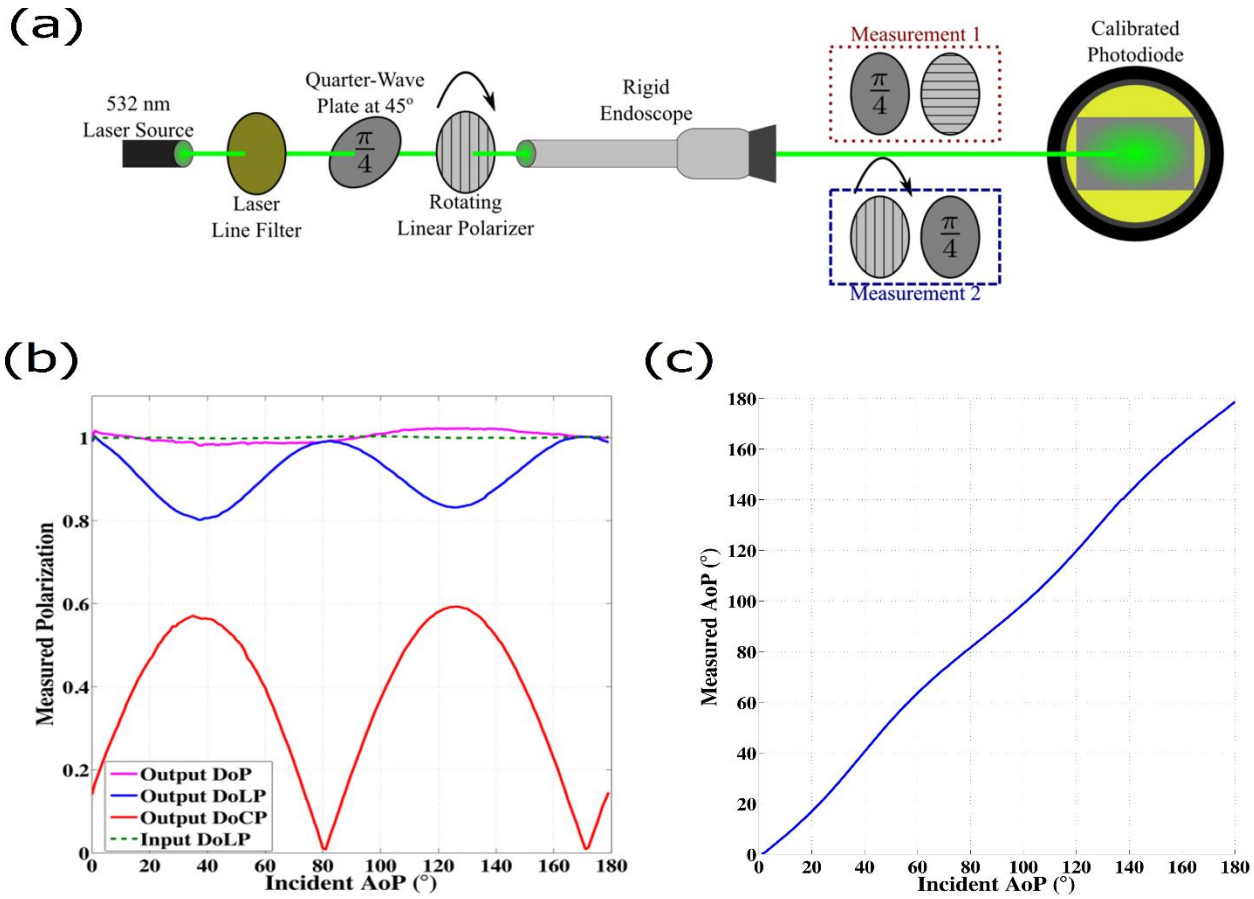

Fig. 4 Optical setup and characterizations involved for evaluating the performance of the endoscope. (a) A polarization state generator is used to illuminate the endoscope and a polarization state analyzer is used to evaluate the polarization performance of the endoscope. (b) Measurements of the polarization performance of the endoscope. The endoscope is illuminated with linearly polarized light between 0 and 180 degrees. While the DoLP decreases by ~20% due to retarder elements in the endoscope, DOP remains at 100%, indicating involvement of circular polarization component. (c) Measured angle of polarization for the light emerging from the endoscope. The endoscope is illuminated with linearly polarized light between 0 and 180 degrees. The endoscope does not affect the angle of polarization of the incident light.

3.2.2 Polarization performance of the endoscope: calibration study

In order to examine how the polarization state of the input light is modified as the light travels through the endoscope, we created an optical setup as shown in Fig. 4a. The polarization properties of light emerging from the endoscope when illuminated with linearly polarized light between 0 and 180 degrees are presented in Fig. 4b, 4c.

Figure 4b presents the measured degree of linear polarization, degree of circular polarization and degree of polarization of the light exiting the endoscope. As light is transmitted through the endoscope, the degree of linear polarization drops to around 80% and the circular polarization equally increases. Hence the degree of polarization remains around one, which indicates that there are very low optical losses, scattering events and sources of depolarization in the endoscope. We believe that the introduction of elliptically polarized light in the endoscope is probably due to retarders that are placed inside the probe. Once the retardance of the endoscope is known, calibration routines can provide the correct input Stokes vector.[34] Furthermore, Fig. 4c represents the angle of polarization of the output Stokes vector that is not affected by the optical elements of the endoscope.

3.3 *Targeting adenomatous tumor and dysplasia in AOM-DSS tissue sections with NIR fluorescent dye-labeled octapeptide (LS301)*

Some colon lesions lie below the mucosa, requiring imagining techniques with depths beyond a few millimeters. Capitalizing on the ability of NIR light to penetrate deeper into tissue with low background autofluorescence compared to visible light, we used a NIR fluorescent dye-labeled octapeptide, LS301; see a and 3b, which has been shown to selectively accumulate in

malignant tumors.[21] We explored the feasibility of using LS301 to detect inflammation-driven colon carcinogenesis using the clinically relevant AOM-DSS murine model. Precancerous and cancerous lesions from AOM-DSS mouse colons were identified and sectioned before incubation with LS301, and the slides were imaged by fluorescence microscopy. Fig. 3c demonstrates that LS301 uptake was highly specific for adenomatous tumor, with minimal fluorescence from the surrounding uninvolved regions. The contrast between adenomatous tumor and surrounding uninvolved tissue was 56 ± 9 (standard error of the mean, s.e.m. was used in this study) with an average contrast-to-noise-ratio (CNR) of 7 ± 1.13. This impressive level of specificity of LS301 was maintained when evaluating tissues exhibiting features sensitive to pre-cancerous lesions, such as aberrant crypt foci as illustrated in Fig. 3d. For example, the contrast between dysplastic lesions and the surrounding uninvolved region as shown in Fig. 3e was 37.4 ± 3.6 with an average CNR of 8.72 ± 0.88. In contrast, the dye cypate alone did not show any selective uptake in the colon lesions. Therefore, we used LS301 for subsequent *in vivo* studies of the AOM-DSS model.

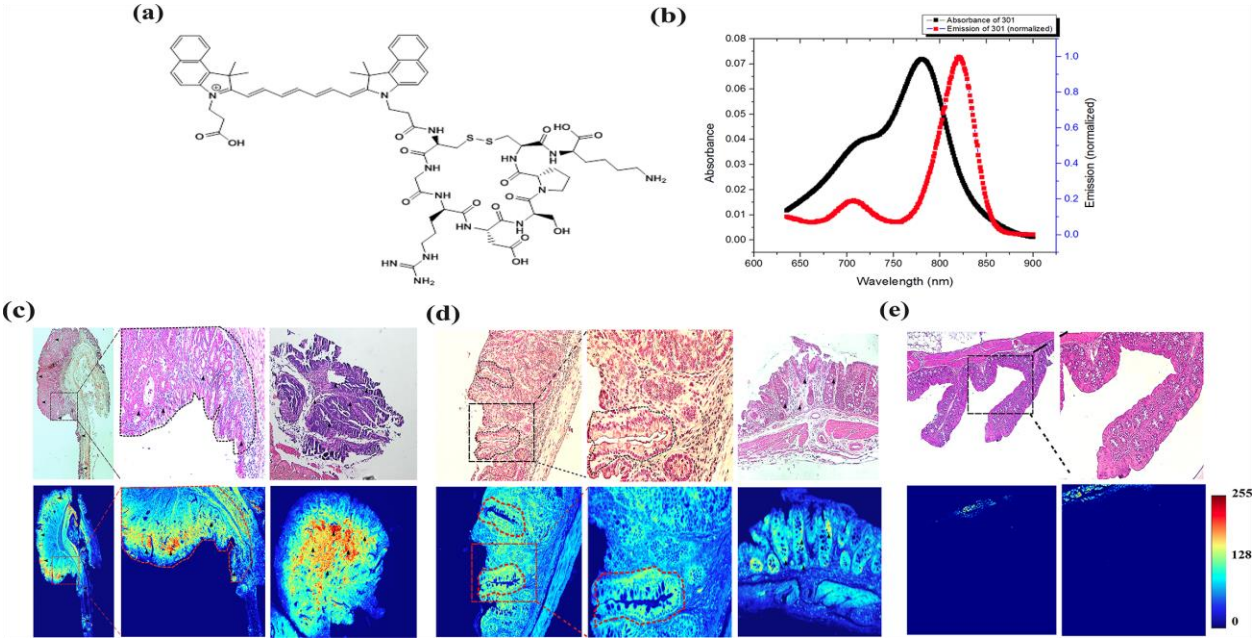

Fig. 3 *Ex-vivo* fluorescence imaging using LS301 on AOM-DSS tissue sections. (a) Molecular structure of LS301. (b) Absorption and emission spectra of LS301. (c) H&E and corresponding NIR fluorescence stains of tumors identified along the distal colon of a mouse treated with AOM-DSS. Arrow points the regions of the tumor that exhibit enhanced binding of LS301. Black and red dotted lines identify the region that marks the initiation of adenomatous tumor. (d) H&E and corresponding NIR fluorescence stains of dysplastic lesions identified along the colon of mice treated with AOM-DSS. Regions marked by red dotted lines mark the boundaries of the crypts. Arrows point to regions along the aberrant crypts towards which LS301 demonstrates preferential binding. (e) H&E and corresponding NIR fluorescence stains of normal ascending colon of mice treated with AOM-DSS displaying minimal non-specific probe binding towards muscularis mucosa.

3.4 In vivo fluorescence and polarization endoscopy

3.4.1 NIR fluorescence endoscopy utilizing novel topical administration method in AOM-DSS and wound-healing models

Having demonstrated the feasibility of detecting CAC and dysplasia by fluorescence imaging and established the polarization contrast between diseased and normal tissues, we next assessed the use of these combined techniques for *in vivo* imaging. Previous small animal imaging of tumors with LS301 have relied on the intravenous administration of the molecular probe.[21] Typically, a wait time of 24 hours is needed to obtain excellent contrast between tumors and uninvolved surrounding tissue. While this imaging time point is acceptable for many clinical applications, a fast-acting approach would be preferred for colonoscopy. Toward this goal, we explored a topical delivery method in which the molecular probe is sprayed on the colon during screening endoscopy. We found that poloxamer (Pluronic F127), which is approved for human use, can solubilize LS301 (see Fig.2B; *Methods, Formulation of LS301*). More importantly, the formulation undergoes reversible thermoresponsive sol-gel transition, with a critical transition temperature of 20^{o}C. This previously unexplored topical application of NIR molecular probes allowed endoscope-mediated spraying of the cold formulation, resulting in a rapidly formed thin layer of gel around the colon tissue. With this method, we observed a mean CNR of 20.64 ± 1.65 between the adenomatous tumor and surrounding uninvolved tissue, and 12.1± 1.03 between flat lesions and surrounding uninvolved regions as displayed in Fig. 5a and 6a respectively. These outcomes represent a six-fold and three-fold increase in mean fluorescence intensity from the adenomatous tumor and flat lesions, respectively, relative to surrounding uninvolved tissues.

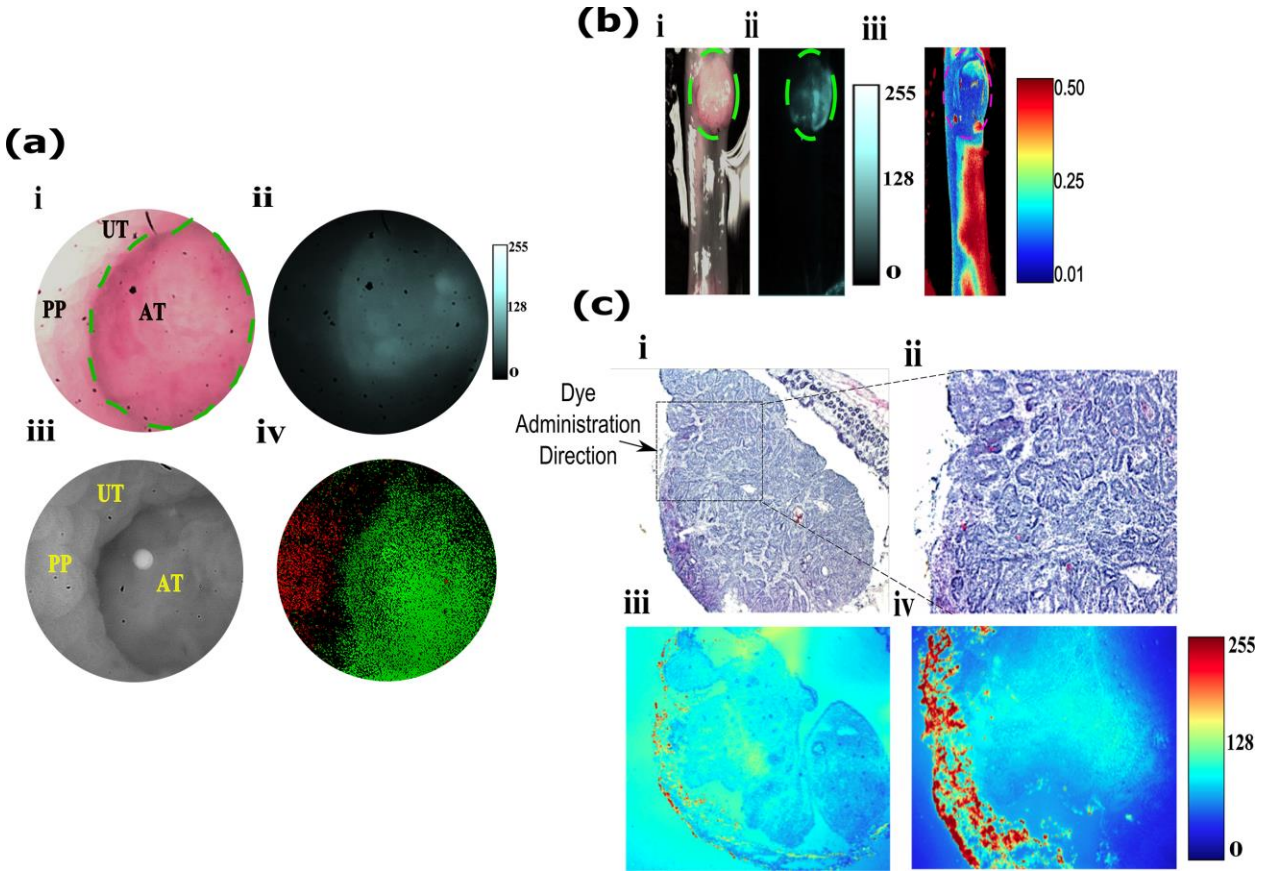

Fig. 5 *In vivo* and *in situ* fluorescence and polarization endoscopy of adenomatous tumor-surrounding un-involved boundary. (a) *In vivo* fluorescence and polarization endoscopy. (i) RGB color image of the tumor identified in the distal colon of an AOM-DSS treated mouse. (ii) Fluorescence image clearly identifies boundaries of the tumor. (iii) Grayscale image consisting of DoLP and AOP information in the polarization mode at 30 frames per second. Bright spot in image is from the light source. (iv) Thresholded DoLP mask image identifies inflamed regions (reported as DoLP value above 10%; red color) and cancerous regions (DoLP value under 5%; green color). (b) *Ex-vivo* (i) RGB, (ii) NIR fluorescence, and (iii) polarization images of tumor identified in (a). Dotted yellow lines in (i) and (ii) indicate the boundary of the tumor. Thresholded DoLP mask image identifies cancerous regions (DoLP value under 10%; green color) (c) Histological validation of adenomatous tumor identified in (b), along with corresponding NIR fluorescence intensity. Dotted rectangle identifies the region under investigation in (ii and iv). Arrow indicates the direction of molecular probe administration. **UT:** Uninvolved Tissue, **PP:** Peyer's patch, **AT:** Adenomatous Tumor

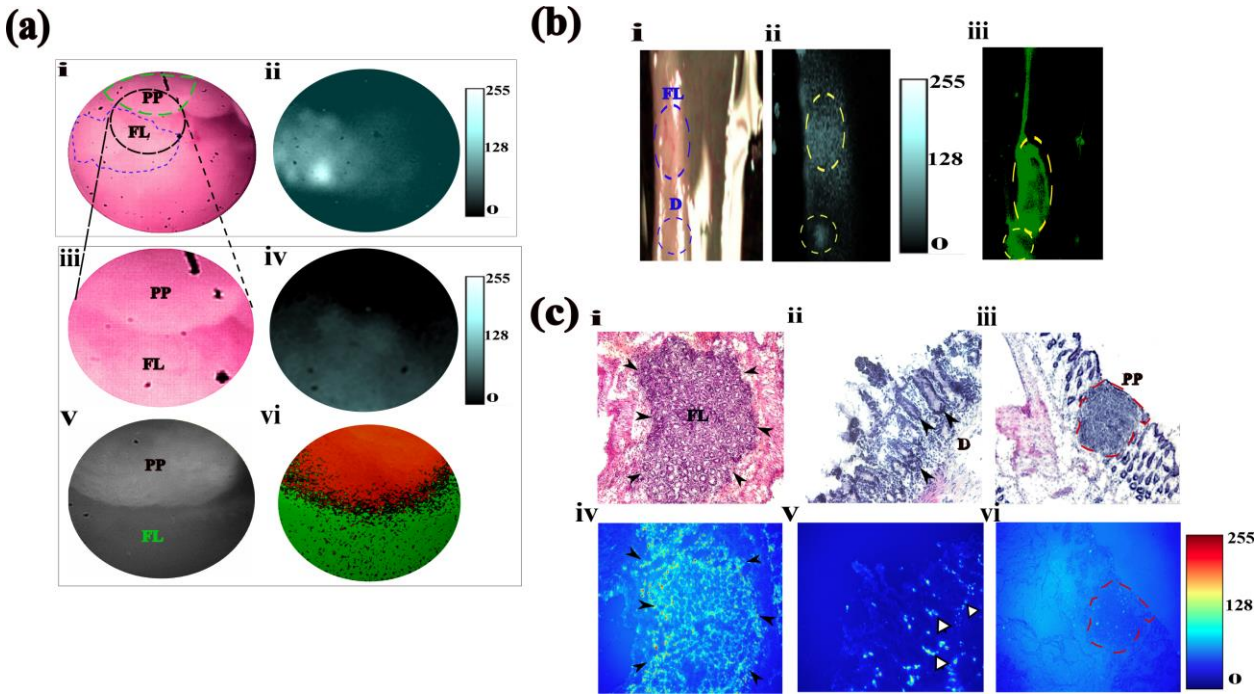

Fig. 6 *In vivo* and *ex vivo* fluorescence and polarization endoscopy of flat lesion-surrounding un-involved boundary. (a) *In vivo* fluorescence and polarization endoscopy. (i) RGB color image of the flat lesion identified in the distal colon of an AOM-DSS treated mouse. Dotted green line outlines the boundary of the Peyer's patch. Dotted blue line outlines the boundary of the flat lesion biopsied in accordance to corresponding fluorescence image. Dotted black circle identifies the region that was investigated more closely (iii) and serves as the field of view region for the remaining *in vivo* images. Grayscale image consisting of DoLP and AOP information in the polarization mode at 30 frames per second. (v) Corresponding region to (iii) identified by polarization camera in grayscale (vi) Thresholded DoLP mask image identifies Peyer's patch (reported as DoLP value above 10%; red color) and flat lesion (reported as DoLP value less than 5%; green color). (b) *Ex-vivo* RGB (i), NIR fluorescence (ii), and DOLP (iii) images of flat lesion identified in (a). Dotted blue line indicates the boundary of the flat lesion (FL) and dysplastic tissue (d). (ii) Corresponding NIR fluorescence image demonstrates fluorescence signal from flat lesions and dysplastic tissue. (iii) Dotted red lines indicate the corresponding flat lesion and dysplastic tissue. Thresholded DoLP mask image identifies cancerous regions (DoLP value under 10%; green color) (c) Histological validation of flat lesion, dysplastic tissue and Peyer's patch identified in (a) and (b) along with

corresponding NIR fluorescence intensity, respectively. For the flat lesion, black solid arrows indicate the boundary of tumor in the H&E and NIR fluorescence images. For dysplastic tissue, black solid arrows indicate the aberrant crypts identified by LS301 in the H&E image and white solid arrows in the NIR fluorescence image. A dotted red line indicates the boundary of the Peyer's patch in the H&E and NIR fluorescence image. **PP:** Peyer's patch, **FL:** Flat Lesion

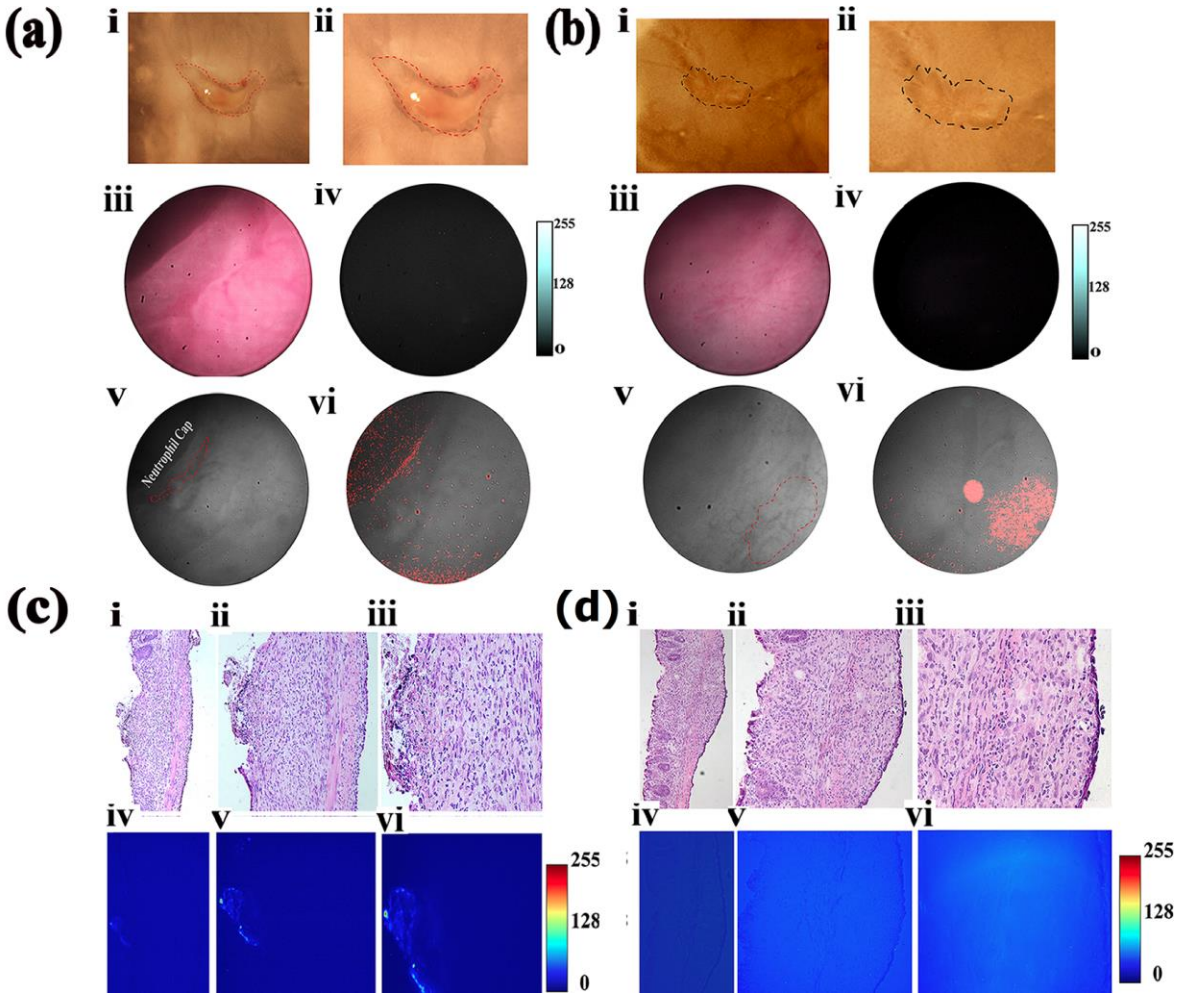

Fig. 7 In vivo and ex vivo fluorescence and polarization endoscopy of wound healing inflammation model. (a) Ex vivo brightfield images of wounds created via endoscopy procedure in vivo. (i,ii) Wound bed at day 4 post endoscopic injury. Dotted red line marks the neutrophil cap formed as a result of inflammation. (iii) RGB color image of the corresponding wound bed identified in (i) within the distal colon of an injury mouse. (iv) Corresponding NIR

fluorescence image demonstrates very minimal binding of the probe towards the proliferative cells in the neutrophil cap. (v) Grayscale image captured using the polarization camera. Dotted red line marks the neutrophil cap region. (vi) Corresponding thresholded DoLP mask image identifying regions higher than established value of 10.6%. (b) Ex vivo brightfield images of wounds created via endoscopy procedure in vivo. (i,ii) Wound bed at day 4 post endoscopic injury. Dotted red line marks the boundary of the wound bed. (iii) RGB color image of the corresponding wound bed identified in (i) within the distal colon of an injury mouse. (iv) Corresponding NIR Fluorescence image demonstrates minimal binding of the probe towards the wound bed (v) Grayscale image captured using the polarization camera. Dotted red line marks the boundary of the wound bed. (vi) Corresponding, thresholded DoLP mask image identifying regions higher than established value of 10.6%. (c) Ex vivo fluorescence binding pattern and histologic validation. (i,ii,iii) H&E images of disrupted epithelium in the inflamed wound region identified in (a). (iv,v,vi) Corresponding NIR fluorescence microscopy images identify proliferative cells in the wound bed. (d) Ex vivo fluorescence binding pattern and histology validation. (i,ii,iii) H&E images of wound bed in (a). (iv,v,vi) Corresponding NIR fluorescence microscopy images identify proliferative cells in the wound bed.

Inflamed tissues generally retain optical contrast agents by several mechanisms, including non-specific retention or entrapment by activated macrophages. Peyer's patches are sites of the host defense system where macrophages, dendritic cells, B-lymphocytes, and T-lymphocytes reside. We observed that LS301 did not accumulate in Peyer's patches in the mucosa as shown by Fig. 6c. The lack of LS301 fluorescence in this tissue indicates the high selectivity of the imaging agent for cancer-associated lesions. To further assess the feasibility of distinguishing wound-repair associated inflammation from colon cancer and dysplasia, we induced colon injury in mice by removing single full thickness areas of the mucosa and submucosa using a flexible biopsy needle. The leading edge of injured epithelium is known to form cables of actin filaments extending from cell-to-cell, forming a ring around the wound circumference and facilitating wound closure.[35] Topical administration of LS301 resulted in a barely detectable mean CNR of 1.62±0.41

between inflamed regions and surrounding uninvolved regions in this wound-healing model using our current fluorescence endoscope as shown in Figure 7. *Ex-vivo* sections of exteriorized colon from the tumor and inflamed regions were examined as shown in Fig. 5b and 6b. Consistent with *in-vivo* results, identified adenomatous tumor and flat lesions showed high fluorescence intensity as seen in Fig. 5c and 6c. A graded fluorescence intensity pattern was observed within the adenomatous tumor mass as shown in 5c, illustrating the diffusion and retention of LS301 in the lesions within ten minutes of administration. LS301 also showed high specificity towards dysplastic lesions possessing features such as aberrant crypt foci as shown in Fig. 6c. Fig. 7a demonstrates minimal fluorescence in the lumen of colonic crypts and features of inflammation, such as regions of neutrophil activation. H&E staining confirmed the presence of these morphological features as shown in Fig. 7c and 7d. *Ex-vivo* studies demonstrated relatively higher fluorescence intensities from regions exhibiting higher epithelial proliferation, which is a consequence of wound-repair as shown in Fig. 7c.

3.4.2 Polarization endoscopy utilizing DoLP contrast in AOM-DSS and wound healing inflammation models

The fluorescence molecular imaging approach deployed above does possess certain limitations. It does not furnish structural information that is useful for validating the presence of cancer or dysplasia, so this information much be obtained via *ex vivo* histologic validation. *Ex vivo* histology requires tissue biopsy and offline analysis that could delay clinical decisions and result in repeat hospital visits. Although the molecular fluorescence method can distinguish inflamed from cancerous tissue or flat lesions, a complementary method that can instantly validate the negative fluorescence contrast in suspicious but non-cancerous tissues would facilitate rapid clinical decision making during colonoscopy. Finally, the topical application of fluorescence

molecular probes and the subsequent washing step occasionally leave residual dye and gel in the vicinity of uninvolved tissue, which could be misinterpreted as cancerous. To resist oversampling of the colon through purely fluorescence guided biopsies and provide real-time confirmation of suspicious lesions, we incorporated the DoLP contrast obtained from reflectance polarization imaging into our fluorescence endoscope. Both the fluorescence and DoLP contrasts are orthogonal, providing complementary positive fluorescence and DoLP signals in cancerous and uninvolved colon tissues, respectively, but negative fluorescence and DoLP signals in uninvolved and cancerous colon tissues, respectively. To rule out false positive DoLP signature caused by the irregular contours of the colon, a small field of view was used to interrogate tissue highlighted by molecular fluorescence imaging.

Post-acquisition, regions of interest were selected to quantify the DoLP signature as shown in video 1. For adenomatous polyps, a mean DoLP value of 0.0414 ± 0.0142 was obtained compared to 0.0816 ± 0.0173 from the surrounding uninvolved regions. We found a similar trend for flat lesions, with a mean DoLP of 0.0225 ±0.0073 compared to 0.0924 ± 0.0284 from the surrounding wall as shown in video 2. While the fluorescence imaging was able to detect pathologic tissue, the high DoLP signal in uninvolved tissue provides an anatomical landscape of the colon and identifies different types of uninvolved colon tissue. For example, Peyer's patches, which were not detected by fluorescence, had a high mean DoLP signal of 0.1064 ± 0.0104, compared to 0.0872 ± 0.022 from surrounding wall (video 1). These differences in DoLP signal are probably due to the higher structural integrity of Peyer's patches caused by the high density of lymphoid tissue. In the wound-healing model, the increase in newly formed actin filaments resulted in a high birefringence signal, thereby polarizing the incident light in the process.[36] For example, a high mean DoLP signal of 0.1363 ± 0.0379 was obtained along the epithelium

surrounding the wound bed as demonstrated in Fig. 7a and 7b. Thus, the combined high polarization and low LS301 fluorescence signals in non-tumor tissue provide real-time validation of suspicious lesions during endoscopy, which reduces the number of false-positives and unnecessary biopsies.

To examine colon tissue under controlled conditions and provide maximum contrast, *ex-vivo* polarization imaging was conducted at 35^0 using the tissue from the *in vivo* study. Consistent with the *in vivo* studies, Fig. 6b exhibits a lower DoLP signature was obtained for flat lesions compared to surrounding uninvolved regions. Patches of higher DoLP signature were observed around the flat lesion, clearly identifying the non-tumor Peyer's patch.

4 Discussion

We have developed an integrated fluorescence and polarization endoscope for detecting and providing real-time confirmation of CAC, dysplasia, and associated flat lesions that are difficult to detect without *ex vivo* histologic validation. Although depressed cancerous lesions and sessile serrated adenomas have different pathology, we used the term flat lesions for both flat depressed carcinomas and adenomas to reflect the similarity in the level of difficulty in detecting these lesions during conventional colonoscopy. Unlike current endoscopic techniques that interrogate molecular or structural signatures of CAC and dysplasia, the combined fluorescence and polarization contrasts create a new paradigm for identifying colonic lesions with high accuracy. The murine AOM-DSS model used in this study recapitulates the molecular pathways and morphological features of CAC from dysplasia to carcinoma.[37] Similarly, the murine wound-healing model exhibits key features of inflammation that are reminiscent of malignancy. These

include wound-associated epithelial cell proliferation and stromal neutrophil and macrophage recruitment in the wound bed.

Our fluorescence imaging approach is similar to chromoendoscopy, where non-tumor targeted dyes are applied topically for improved visualization of dysplastic lesions.[11, 38] Previous studies attempted to use the FDA-approved NIR dye, indocyanine green (ICG), to enhance the detection of submucosal colon lesions and minimize tissue autofluorescence.[39] Unfortunately, the high background ICG fluorescence in the subserosa around the tumor confounded data analysis. In a recent study, we showed that LS301 selectively accumulates in tumors and achieves high tumor-to-background fluorescence at 24 hour post intravenous injection.[21] Using the AOM-DSS treated mouse model of CAC, we demonstrated in this study that *ex-vivo* staining of colon tissue with LS301 successfully identified adenomatous tumors and dysplastic lesions in the colon tissue as shown in Fig. 3c and 3d. *Ex vivo* histologic validation confirmed the *in vivo* imaging analysis. These results demonstrate that molecular fluorescence endoscopy, aided by LS301, detects multiple stages of oncogenesis with high potential to improve the management of colorectal cancer.

However, the intravenous administration of LS301 and the long wait time (24 h) to achieve high fluorescence contrast between tumors and uninvolved surrounding colon tissue are not suitable for colonoscopy. In addition, the excretion of LS301 through the hepatobiliary pathway after intravenous injection increases background NIR fluorescence in the colon, compounding the detection of flat lesions and dysplasia. Based on our *ex vivo* study, we postulated that the rapid and prolonged retention of LS301 in pathologic tissues lends it to topical administration during colonoscopy. The results demonstrate that the formulation of LS301 in a poloxamer sol-gel transition system allowed us to topically administer the imaging agent with a spray catheter during

endoscopy. In contrast to the use of generic dyes for chromoendoscopy, the selective uptake of LS301 in CAC and dysplastic colon tissue minimized nonspecific uptake in uninvolved mucosa, ushering in a new procedure for topical administration of tumor-targeted molecular probes. The commercially available poloxamer not only improved the solubility of the hydrophobic LS301, but also aided in the uniform coating of the tissue, thereby increasing the interaction of the molecular probe gel formulation with the colon tissue under investigation. The observed high mean CNR obtained from adenomatous tumors and flat lesions compared to surrounding uninvolved tissue is a function of the improved molecular probe selectivity for tumors, reduced autofluorescence in the NIR imaging window, and enhanced incubation time provided by the sol-gel formulation. This sol-gel approach can be extended to previously reported methods for imaging colon cancer and dysplasia. These include Cy5.5 labeled cathepsin B substrate used to identify polyps in adenomatous polyposis coli (Apc min) mice[40] and fluorescein-labeled VRPMPLQ heptapeptide that was shown to preferentially bind dysplastic rather than normal mucosa.[19] Unlike these molecular probes which are confined to identifying only specific stages of tumorigenesis,[41, 42] LS301 uniquely captures multiple stages of cancer development. A limitation of the sol-gel method is the lag time between topical application and imaging. Our current protocol uses about 10 minutes to optimize tumor uptake. A future goal is to optimize the procedure to shorten the incubation time for rapid assessment of the colon.

Although the topical administration of LS301 has enormous benefits for screening endoscopy, we found that polarization contrast can provide real-time cross-validation of suspicious lesions with an orthogonal but complementary signal. This approach is expected to minimize the need for *ex vivo* biopsy, accelerate medical decisions, and improve clinical outcomes with minimal

recall rates. In addition, false positive fluorescence arising from residual gelatinous materials in healthy colon can readily be identified by the low polarization contrast in healthy tissue.

Previous studies have reported the use of polarized light scattering spectroscopy and reflectance spectroscopy for tissue analysis.[28, 43, 44] In these studies, *ex vivo* colonic tissue specimens were illuminated with polarized light and morphological maps of the specimens were constructed based on varying nuclear sizes, population density and refractive index.[28, 43, 44] However, the system configuration and challenges in real-time mapping of the polarization signal undermine its use for *in vivo* applications. We circumvented these challenges by developing an imaging configuration and sensor setup capable of reporting DoLP and AOP changes in the reflected light, while taking into account the relative positions of the camera with respect to the tissue. As DoLP reports on the fraction of reflected light that is linearly polarized, we expect differences between the DoLP signature in epithelial layer of diseased and healthy tissue. Pre-cancerous and cancerous lesions within the epithelial layer possess distinct morphological features, such as increased nuclear size and increased nuclear-cytoplasmic ratio, which results in significant multiply scattered components of light and a corresponding decrease in DoLP signature. A mean DoLP change of 4% was obtained for polypoid tissue in the surrounding uninvolved region. This change was validated by simulation results as depicted in Fig. 1b, where we predicted a change of 4% in DoLP signature when imaging at 15^0. In the case of flat lesions, we obtained a DoLP difference of 7% relative to the surrounding Peyer's patch regions. The exceptionally high DoLP signal in Peyer's patches stems from the formation of firmly matted fibrotic bands within the serosa and mesentery as shown in video 1. The increase in concentration of linearly birefringent material, such as actin, results in a DoLP difference of 10% in the inflamed regions compared to surrounding uninvolved colonic tissue. We demonstrated our ability to rapidly interrogate regions of interest in

real time (at 40 frames per second) without distortion from motion artifacts arising from respiration and peristalsis as shown in videos 1 and 2.

In summary, the combination of a tumor-targeting molecular probe, topical application of a contrast agent with a biocompatible sol-gel formulation, and the development of a multimodal color, NIR fluorescence, and polarization endoscope provides a new paradigm for the accurate detection of colonic lesions, including CAC, dysplasia, and the associated flat lesions. Extension of this approach to a wound-healing inflammation model[22] demonstrated a reversal of the fluorescence-polarization signal, highlighting the complementary nature of both techniques. The ease of incorporating both fluorescence and polarization fibers into an existing endoscope allows seamless integration into current screening colonoscopy protocols. A similar approach can be envisaged for other forms of epithelial cancer such as esophageal, cervical, bladder, skin, and stomach tumors that account for over 65% of the non-colorectal cancer deaths.

5 Acknowledgements

We thank Mr. Nick Manieri for his assistance with the endoscopy and biopsy procedure on the AOM-DSS and wound-healing inflammation mice. We also thank Dr. James Ballard for reading the manuscript. The authors acknowledge funding support from US National Institutes of Health including R01 CA171651 (NCI). TC was supported by NIH grant F31 CA171798. The authors of this manuscript have no competing interests.

6 References

1. J. A. Eaden et al., "The risk of colorectal cancer in ulcerative colitis: a meta-analysis," *Gut* **48**(4), 526-535 (2001).
2. N. A. Molodecky et al., "Increasing incidence and prevalence of the inflammatory bowel diseases with time, based on systematic review," *Gastroenterology* **142**(1), 46-54 e42; quiz e30 (2012).
3. R. Siegel et al., "Cancer Statistics, 2012," *A Cancer Journal for Clinicians* **62**(1), 10-29 (2012).
4. S. D. Markowitz et al., "Molecular origins of cancer: Molecular basis of colorectal cancer," *The New England journal of medicine* **361**(25), 2449-2460 (2009).
5. S. H. Itzkowitz et al., "Inflammation and cancer IV. Colorectal cancer in inflammatory bowel disease: the role of inflammation," *American journal of physiology. Gastrointestinal and liver physiology* **287**(1), G7-17 (2004).
6. R. Kiesslich et al., "Methylene blue-aided chromoendoscopy for the detection of intraepithelial neoplasia and colon cancer in ulcerative colitis," *Gastroenterology* **124**(4), 880-888 (2003).
7. T. Ullman et al., "Progression of flat low-grade dysplasia to advanced neoplasia in patients with ulcerative colitis," *Gastroenterology* **125**(5), 1311-1319 (2003).
8. M. Kanneganti et al., "Animal models of colitis-associated carcinogenesis," *Journal of biomedicine & biotechnology* **2011**(342637 (2011).
9. C. Neufert et al., "An inducible mouse model of colon carcinogenesis for the analysis of sporadic and inflammation-driven tumor progression," *Nature protocols* **2**(8), 1998-2004 (2007).
10. F. A. Farraye et al., "AGA technical review on the diagnosis and management of colorectal neoplasia in inflammatory bowel disease," *Gastroenterology* **138**(2), 746-774, 774 e741-744; quiz e712-743 (2010).
11. M. F. Neurath et al., "Is chromoendoscopy the new standard for cancer surveillance in patients with ulcerative colitis?," *Nature clinical practice. Gastroenterology & hepatology* **6**(3), 134-135 (2009).
12. A. Hoffman et al., "High definition colonoscopy combined with i-Scan is superior in the detection of colorectal neoplasias compared with standard video colonoscopy: a prospective randomized controlled trial," *Endoscopy* **42**(10), 827-833 (2010).
13. C. Becker et al., "High resolution colonoscopy in live mice," *Nature protocols* **1**(6), 2900-2904 (2006).
14. F. Emura et al., "Narrow-band imaging optical chromocolonoscopy: advantages and limitations," *World journal of gastroenterology : WJG* **14**(31), 4867-4872 (2008).
15. J. Pohl et al., "Pancolonic chromoendoscopy with indigo carmine versus standard colonoscopy for detection of neoplastic lesions: a randomised two-centre trial," *Gut* **60**(4), 485-490 (2011).
16. P. A. Testoni et al., "Optical coherence tomography in detection of dysplasia and cancer of the gastrointestinal tract and bilio-pancreatic ductal system," *World journal of gastroenterology : WJG* **14**(42), 6444-6452 (2008).
17. E. Zagaynova et al., "Endoscopic OCT with forward-looking probe: clinical studies in urology and gastroenterology," *Journal of biophotonics* **1**(2), 114-128 (2008).
18. S. Foersch et al., "Molecular imaging of VEGF in gastrointestinal cancer in vivo using confocal laser endomicroscopy," *Gut* **59**(8), 1046-1055 (2010).
19. P. L. Hsiung et al., "Detection of colonic dysplasia in vivo using a targeted heptapeptide and confocal microendoscopy," *Nature medicine* **14**(4), 454-458 (2008).
20. H. Neumann et al., "Confocal laser endomicroscopy: technical advances and clinical applications," *Gastroenterology* **139**(2), 388-392, 392 e381-382 (2010).
21. Y. Liu et al., "Hands-free, wireless goggles for near-infrared fluorescence and real-time image-guided surgery," *Surgery* **149**(5), 689-698 (2011).
22. H. Seno et al., "Efficient colonic mucosal wound repair requires Trem2 signaling," *Proceedings of the National Academy of Sciences of the United States of America* **106**(1), 256-261 (2009).

23. T. York et al., "Characterization of a visible spectrum division-of-focal-plane polarimeter," *Applied optics* **51**(22), 5392-5400 (2012).
24. S. Achilefu, et al., "Synthesis, in vitro receptor binding, and in vivo evaluation of fluorescein and carbocyanine peptide-based optical contrast agents," *Journal of medicinal chemistry* **45**(10), 2003-2015 (2002).
25. T. V, *Tissue Optics: Light Scattering Methods and Instruments for Medical Diagnosis*, SPIE, Bellingham, WA (2000).
26. D. Hidovic-Rowe et al., "Modelling and validation of spectral reflectance for the colon," *Physics in medicine and biology* **50**(6), 1071-1093 (2005).
27. J. Ramella-Roman, et al., "Three Monte Carlo programs of polarized light transport into scattering media: part I," *Optics express* **13**(12), 4420-4438 (2005).
28. V. Backman et al., "Detection of preinvasive cancer cells," *Nature* **406**(6791), 35-36 (2000).
29. R. S. Gurjar et al., "Imaging human epithelial properties with polarized light-scattering spectroscopy," *Nature medicine* **7**(11), 1245-1248 (2001).
30. L. T. Perelman, "Observation of Periodic Fine Structure in Reflectance from Biological Tissue: A New Technique for Measuring Nuclear Size Distribution," *Phys. Rev. Lett.* **80**(627-630 (1998).
31. H. Ao et al., "Thermal coagulation-induced changes of the optical properties of normal and adenomatous human colon tissues in vitro in the spectral range 400-1,100 nm," *Physics in medicine and biology* **53**(8), 2197-2206 (2008).
32. V. Gruev et al., "CCD polarization imaging sensor with aluminum nanowire optical filters," *Opt Express* **18**(18), 19087-19094 (2010).
33. Y. Liu et al., "Complementary fluorescence-polarization microscopy using division-of-focal-plane polarization imaging sensor," *J Biomed Opt* **17**(11), 116001 (2012).
34. S. B. Powell et al., "Calibration methods for division-of-focal-plane polarimeters," *Optics express* **21**(18), 21039-21055 (2013).
35. Y. Danjo et al., "Actin 'purse string' filaments are anchored by E-cadherin-mediated adherens junctions at the leading edge of the epithelial wound, providing coordinated cell movement," *Journal of cell science* **111**(22),3323-3332 (1998).
36. K. Katoh et al., "Birefringence imaging directly reveals architectural dynamics of filamentous actin in living growth cones," *Molecular biology of the cell* **10**(1), 197-210 (1999).
37. T. A. Ullman et al., "Intestinal inflammation and cancer," *Gastroenterology* **140**(6), 1807-1816 (2011).
38. R. Kiesslich et al., "Surveillance colonoscopy in ulcerative colitis: magnifying chromoendoscopy in the spotlight," *Gut* **53**(2), 165-167 (2004).
39. M. Kusano et al., "Sentinel node mapping guided by indocyanine green fluorescence imaging: a new method for sentinel node navigation surgery in gastrointestinal cancer," *Digestive surgery* **25**(2), 103-108 (2008).
40. K. Marten et al., "Detection of dysplastic intestinal adenomas using enzyme-sensing molecular beacons in mice," *Gastroenterology* **122**(2), 406-414 (2002).
41. M. Karin et al., "NF-kappaB: linking inflammation and immunity to cancer development and progression," *Nature reviews. Immunology* **5**(10), 749-759 (2005).
42. S. I. Grivennikov et al., "Immunity, inflammation, and cancer," *Cell* **140**(6), 883-899 (2010).
43. M. B. Wallace et al., "Endoscopic detection of dysplasia in patients with Barrett's esophagus using light-scattering spectroscopy," *Gastroenterology* **119**(3), 677-682 (2000).
44. K. Sokolov et al., "Reflectance spectroscopy with polarized light: is it sensitive to cellular and nuclear morphology," *Optics express* **5**(13), 302-317 (1999)

Chapter 5

A NIR-fluorescence imaging platform distinguishes pancreatic cancer and pancreatitis non-invasively and guides NIR fluorescence laparoscopy for "smart biopsies"

Chapter 5 is a reformatted version of a manuscript in submission: “Tauseef Charanya, Yu Zhu, Pinaki Sarder, Joe Culver, David Denardo, Samuel Achilefu et al. A NIR-fluorescence imaging platform distinguishes pancreatic cancer and pancreatitis non-invasively and guides NIR fluorescence laparoscopy for “smart biopsies”. My contributions to this work included designing the experiments, carrying out the imaging studies involving pancreatitis and pancreatic cancer models, interpreting and analyzing data, and writing the manuscript. In this chapter, I discuss my work in the non-invasive detection of pancreatic cancer versus pancreatitis followed by guided intervention NIR laparoscopy approach using NIR targeted probe, LS301. Furthermore, binding studies using immunohistochemistry and flow cytometry helped further validate the specificity of the molecular probe.

Abstract

Pre-cancerous and cancerous pancreatic lesions typically go undetected and/or undifferentiated from pancreatitis by current non-invasive and invasive means, resulting in horrendous prognosis. We have developed a NIR fluorescence-based imaging platform consisting of a noninvasive fluorescence molecular tomography (FMT) system and a targeted NIR-fluorescent molecular probe to distinguish between pancreatitis and pancreatic cancer. This system allows for guided interventional fluorescence laparoscopy to ensure complete tumor resection and distinction of cancerous lesions from pancreatitis. Using caerulein-treated acute and chronic pancreatitis models along with both spontaneous and orthotopic pancreatic cancer models, we demonstrated five-fold higher total fluorescence intensity in pancreatic cancer models versus pancreatitis and 8 to 12 fold higher tumor-to-background ratios (TBR). Ex-vivo fluorescence binding patterns in pancreatic cancer of our molecular probe demonstrated high correlation with the established marker such as cytokeratin 19 (CK19). Flow-cytometry further validated the specific binding and retention of the molecular probe in pancreatic tumor cells. Together, the targeted molecular probe and FMT guided fluorescence laparoscopy intervention provides a method for early detection of pancreatic cancer and non-invasive distinction between cancer and pancreatitis.

Translational Relevance

Pancreatic ductal adenocarcinoma (PDAC) is a lethal disease with horrendous prognosis. This typically arises due to the relatively symptom-free nature of the disease. Moreover, the few common symptoms that it does possess are extremely similar to that of pancreatitis. The current procedural complexity of the disease has been known to introduce complications of its own. Advancements in detection methods from imaging and targeted molecular probe standpoint to

allow for non-invasive prognosis prior to any invasive procedure are lacking in specificity and sensitivity of detection. Our results have identified a platform of imaging that allows for a non-invasive distinction of PDAC from pancreatitis prior to a near-infrared-based-laparoscopy procedure that allows to collect "smart biopsies". The targeted molecular probe utilized plays an integral role in this platform for its ability to selectively retain in pancreatic tumor cells versus normal pancreas. This platform can be easily translated to humans *via* introducing a nuclear analog of this molecular probe to allow for SPECT/PET imaging.

Pancreatic ductal adenocarcinoma (PDAC) is one of the most lethal common cancers, mainly because it is usually diagnosed at a very advanced stage. In 2014, there were 46,420 new cases of pancreatic cancer with approximately 40,000 deaths in the United States alone[1]. It has an abysmal five year survival rate of <6% and which only increases to 10 to 25% after diagnosis and pancreatic head resection[2-4]. Late stage diagnosis of pancreatic cancer misdiagnosis of the disease with pancreatitis and the procedural complexity of obtaining biopsy samples serve as the key reasons for poor prognosis.

Late stage diagnosis in pancreatic cancer is associated with misdiagnosis of the disease as pancreatitis and the procedural complexity of obtaining biopsy samples. The distinction between pancreatitis, pancreatic intraepithelial neoplasia (PanINs), and pancreatic cancer is extremely difficult due to their common clinical symptom presentation such as pain, weight loss, and pancreatic endocrine and exocrine dysfunction. The complexity of differential diagnosis is further enhanced as pancreatic cancer is frequently associated with secondary inflammatory changes due to obstruction of the pancreatic duct[5]. Furthermore, obtaining tissue samples can be challenging,

as imaging studies typically fail to demonstrate an obvious mass. Subsequently, biopsy samples may only show a suspicion of neoplasia and not definitively document malignancy, subjecting patients to an inherent risk of morbidity *via* the operating procedure[6]. The need for accurate distinction of pancreatitis from pancreatic cancer and early detection is much desired in clinic.

Advances in pancreatic imaging provide potential to diagnose early. Cornerstones of endoscopic pancreatic imaging are endoscopic retrograde pancreatography (ERP) and endoscopic ultrasonography (EUS) with optical coherence tomography (OCT) and confocal laser endomicroscopy (CLE) serving as supplements to these methods along with intraductal ultrasonography, and enhanced EUS[7-12]. ERP has the ability to image the main pancreatic duct and is specifically used to identify chronic pancreatitis lesions while EUS, on the other hand, allows imaging of both the pancreatic duct as well as the parenchyma[13,14]. However, in early chronic pancreatitis, there are only minimal differences from the normal pancreas, resulting in a histological correlation of only 75% using ERP and 80% using EUS[7]. Furthermore, limitations exist in supplement methods to ERP and EUS such as lack of ability to image non-invasively and/or to identify pancreatic lesions based on their molecular footprint. As a result, both ERP and EUS identify PDAC with limited sensitivity and specificity in patients with chronic pancreatitis and are unable to differentiate chronic pancreatitis from PanINs[7,15]. The need for accurate diagnosis non-invasively prior to invasive laparoscopic procedures is much desired due to the inherent risk of developing pancreatitis *via* the ERP procedure itself[13-14].

Targeted molecular imaging is known to identify molecular signatures that distinguish cancerous lesions from surrounding tissue, and provide versatility to be combined with a modality that provides complementary structural information. Furthermore, it has the ability to image the pancreas non-invasively prior to the semi-invasive laparoscopic tumor resection procedure,

thereby reducing the risks associated with surgery. For example, Bausch et al isolated a biomarker (Plec-1) for pancreatic cancer *via* phage display and, in combination with a SPECT imaging agent, imaged cancerous lesions successfully in mice bearing orthotopic tumors[16]. However, the ability of this probe to distinguish pancreatic cancer from pancreatitis has yet to be explored.

The overarching goal of this study is twofold, firstly to establish an imaging platform that allows for non- invasive distinction between pancreatic cancer and pancreatitis prior to guiding NIR laparoscopy for "smart biopsies" and secondly to establish binding preferences of the targeted molecular probe in the pancreatic tumor microenvironment. In our study, we utilized fluorescence molecular tomography (FMT) prior to guiding a NIR-capable laparoscope for obtaining "smart biopsies". Binding preferences of the molecular probe were analyzed amongst precancerous, cancerous, and uninvolved pancreatic tissues utilizing immunohistochemistry and flow-cytometry. NIR laparoscopy and *ex-vivo* imaging of exteriorized pancreas validated differential signatures obtained between pancreatitis, and pancreatic cancer *via* non-invasive FMT. Binding studies validated preferential uptake of targeted molecular probe in pancreatic tumor versus pancreaetitis and normal pancreas.

Methods and Materials

Targeted NIR fluorescence molecular probes

We have previously demonstrated the use of the targeted molecular probe, LS301 in epithelial-based cancers and have extended its use towards detection of pancreatic cancer lesions in this study[17]. LS301 and its analog, LS789, were synthesized by a previously described method[18]. LS301 consists of a near-infrared fluorescent dye, cypate (780 $_{ex}$/ 830 $_{em}$), and the cyclic peptide

sequence D-Cys-Gly-Arg-Asp-Ser-Pro-Cys-Lys (c($_D$CGRDSPC)K). LS789 (680 $_{ex}$/ 710 $_{em}$) consists of cypate-3 and the peptide sequence cyclo($_D$Cys-Gly-Arg-Asp-Ser-Pro-Cys)-Lys-OH. The conjugation of the dye and peptide sequence was characterized by spectroscopy methods, analytical HPLC, and electrospray ionization mass spectrometry.

Cell lines and culture

We used mouse-derived pancreatic tumor cell lines for development of early and late stage orthotopic pancreatic tumor models. We also utilized mouse derived bone-marrow derived macrophages (BMDM) and human pancreatic cell lines for an *in vitro* binding preference study using LS301.

The KI cell line was derived from pancreatic adenocarcinomas from p48-CRE/LSL-KrasG12D/INK4aflox[19]. All cell lines were mycoplasma tested and labeled with a polycistronic click beetle red luciferase-mCherry reporter by lentiviral infection. These cells were maintained in Dulbecco's Modified Eagle Medium (DMEM) supplemented with 10% fetal bovine serum (Hyclone). All cells were cultured in a humidified incubator at 37^0C with 5% CO_2. Bone marrow was isolated from the femurs and tibias of wild-type B6 mice. Bone marrow was cultured in 20 ng/ml of colony stimulating factor-1 (CSF1) for five days. HPAC cells were derived from primary PDAC (wild type TP53 and SMAD4 with mutations in KRAS +CDKN2A) (p16) (20). The tumor is considered moderately differentiated and of ductal origin. Hs766T cells were derived from a lymph node metastasis (wild type KRAS, TP53, CDKN2A) with pancreatic carcinoma[20-22].

Animal models

All animal studies were performed according to protocols approved by the Washington University School of Medicine Animal Studies Committee for humane care and use of laboratory animals.

KPC spontaneous and orthotopic PDAC model

The well-established spontaneous pancreatic cancer model p48-/Cre^{+}/LSL-$Kras^{G-12D}$/$p53^{flox/+}$ (KPC model) was utilized in this study for its ability to develop a spectrum of premalignant pancreatic intraepithelial neoplasias (PANINs) over a two-month period that ultimately progressed to carcinoma in five to six months[23-24]. KPC mice with a palpable tumor at the five-six month stage were used for the advanced carcinoma stage and those at two and a half month stage were used for the precancerous stage. Synergistic orthotopic PDAC tumors were established by injecting 200,000 cells in 50 µL matrigel (BD Biosciences) into each mouse pancreas[25]. Tumors were allowed to grow over one to two weeks to allow for variable tumor sizes of less than 0.5 cm and between 1-1.5 cm respectively. 50 µL of matrigel alone was injected into the pancreas as control.

Pancreatitis model

To induce acute pancreatitis, we performed 7 intraperitoneal injections of 50 µg/kg caerulein (Sigma, St. Louis, MO, USA) or vehicle in 0.9% NaCl within a 2 day period[26-27]. To induce chronic pancreatitis, we injected caerulein every other day for two months.

Fluorescence Molecular Tomography (FMT) System

FMT system was used as first pass, binary assessment tool for differentiating pancreatic cancer from pancreatitis and normal pancreas prior to follow-up investigation using NIR laparoscopy. Animal studies were conducted on a recently developed temporally resolved fluorescence molecular tomography system[28]. Briefly, a pulsed supercontinuum laser source (K93-120-02; 80 MHz, 400-1200 nm, 5-ps pulse width, integrated power over the spectral window is ~3.5W with 1 mW/nm) was used for illumination. The beam from the laser was expanded ~10 times using two concave mirrors, and passed through a 769/41 nm Brightline® single-band bandpass filter (Semrock, Rochester, NY) for focusing. The beam, after passing through the focusing lens, was steered by a pair of galvanometer scanning mirrors to the source side of an imaging cassette. Light emitted from the detector plane of the imaging cassette was collected by a lens, temporally gated by an ultrafast gated image intensifier, and detected by an electron-multiplying charge-coupled device camera for read-out. Optional filters in front of the lens allow acquisition of either the transmitted excitation or fluorescence emission (832 ± 10 nm). Timing between the source and the gated detection was controlled by a programmable delay unit, allowing a series of images to capture the light emission as a function of time. A scan resulted in a temporal profile of transmitted excitation and stimulated emission at each detector location. From these data, we reconstructed a map of fluorescence yield and lifetime simultaneously via a normalized Born approach[29-30]. Specifically, we used an analytical solution to the diffusion equation that incorporated absorption and scattering in the light model[31]. Our studies described in this manuscript employed the econstructed fluorescence yield for detection of pancreatic cancer in the mice that we imaged.

For studies, each mouse was anesthetized with a mixture of ketamine (87mg/kg) and xylazine (13 mg/kg) intraperitoneally, prior to scanning. They were then suspended vertically

within the optical-matching fluid-filled imaging cassette for duration of the scanning session, as previously described[28]. The role of the optical-matching fluid is to create diffuse optical properties that match those of the mouse. Intralipid and India ink are added to deionized (DI) water to reduce the scattering coefficient (μ_s') and absorption coefficient (μ_a') respectively. For the in vivo experiments, we use μ_s' = 10 cm^{-1} and μ_a' = 0.2 cm^{-1} to match optical properties of the mouse[28]. Subsequently, a computed tomography (CT) image of the mouse was obtained in the orientation it was placed in the cassette, to provide supplementary structural information to FMT data.

Small animal imaging

Planar imaging systems serve as a reliable tool for biodistribution studies due to their high sensitivity of detection along with their ability to reliably resolve depths less than 1 cm (within the range of excised tissues). A commercially available fluorescence planar imaging system (LiCor Biosciences, Lincoln, Nebraska) was used to perform superficial (<1 cm) NIR fluorescence imaging of live mice, and exteriorized organs for validation, post-FMT and NIR laparoscopy imaging. The method employed for imaging has been reported previously[32]. Mice were positioned supine on the heated imaging platform. A 785 nm excitation wavelength and 830 nm emission was used to conduct *in vivo* imaging. Scans were obtained immediately, 1 hour, 4 hours, 24 hours, and 48 hours post administration of imaging agent. The pancreas and/or pancreatic tumor was exteriorized prior to imaging and regions of interest (ROIs) were identified. For each selected region, the mean fluorescence intensity values for the tumor or pancreas and the surrounding region (spleen) were determined and reported for analysis. In cases where tumor had infiltrated to the surrounding spleen organ (PDAC two week models), areas of the spleen that weren't affected

were used as a point of reference. Mean fluorescence intensity was determined for each tissue by ROI analysis and results were combined for each group for statistical analysis.

Color-NR Endoscope

A color-NIR endoscope was utilized in order to guide biopsy post non-invasive imaging using (FMT) system. NIR laparoscopy was also performed to validate the findings from FMT and ensure complete resection of pancreatic tumor. The NIR color endoscope device developed in our lab and used in this study has been previously reported[33]. Briefly, in color mode, a xenon light source with adjustable light intensity was coupled to the illumination channel on a 0^0 Hopkins (1.9 mm x 10 cm) straightforward telescope (Karl Storz, Tuttlingen, Germany). A telescope coupler with a focus ring focused the CCD camera on the image formation plane at the back of the telescope. In the fluorescence mode, a 780 nm mounted LED, 420 mW (Thorlabs, Newton, New Jersey) with a 26.5 mm Carco poly-carbonate collimated lens coupled to a 769/41 nm Brightline ® single-band bandpass filter (Semrock, Rochester, NY) was used. An 808 nm long-pass emission filter (Chroma Technology, Bellows Falls, VT) was utilized to ensure capturing the emission characteristics of the molecular probe. Images were captured using a NIR-sensitive CCD camera.

Forty-eight hours after the injection of LS301, mice were anesthetized *via* intraperitoneal injection of a solution of ketamine and xylazine and placed supine on the surgical bed prior to the procedure. An incision was made from the epi-gastric/zyphoid process region down to the lower abdomen. An exploratory laparotomy was performed around the pancreatic region using color-NIR laparoscope. Once an identifiable NIR signal was observed, images were captured and the corresponding color image was obtained. Similarly, images and the corresponding NIR signals were captured of surrounding organs such as spleen, liver, stomach and small intestine.

Flow Cytometry Analysis

In order to better understand the probe binding characteristics, flow cytometry was conducted utilizing normal pancreas and orthotopic pancreatic tumor tissue. Mouse tumors or normal pancreatic tissues were minced and enzymatically digested into a single cell suspension, and incubated with anti-mouse CD16/CD32 antibodies (eBiosciences) to prevent nonspecific antibody recognition. Cells were stained for 20 minutes at 4^0C with 100 μL of fluorophore-conjugated anti-mouse antibodies [CD3e (145-2C11), CD11b (M1/70), CD19 (MB19-1), CD45 (30-F11), CD49f (eBioGoH3), CD90 (53-2.1), F4/80 (BM8), Ly6C (HK1.4), Ly6G (1A8), MHCII (M5/114.15.2)] (all from eBiosciences) at concentrations recommended by the manufacturer. Data was acquired on the LSR-II system (BD Biosciences) and analyzed using the FlowJo software version 9.2 (Tree Star).

Immunofluorescence

Tissues were harvested from mice 48 hours post probe administration, immediately embedded in optimal cutting temperature compound, and snap frozen. Six μm thick sections were fixed in 4% paraformaldehyde for 15 minutes at room temperature and stained with CK19 (TROMA-III-c, from Developmental Studies Hybridoma Bank). Olympus BX51 upright epifluorescence microscope (Olympus America, Center Valley, PA, USA) was used to image Cy 5 fluorescence originating from CK19 probe (620 +/- 60 excitation, 700 +/- 75 emission filters used), and NIR fluorescence originating from LS301 molecular probe (775 +/-50 nm excitation, 810 nm long-pass dichroic, and 845 +/-55 nm emission filters was used). Golds standard

hematoxylin and eosin (H&E) staining was conducted to compare fluorescence binding patterns with corresponding morphological features of pancreatic tissues.

Internalization Study

Mouse BMDM and HPAC cells were grown on Lab-Tek slides. Cells were treated for 6h with 1 uM LS301. After the incubation the cells were rinsed one with PBS containing 1 mM $CaCl_2$ and imaged with an Olympus FV 1000 confocal microscope, using a 60x water immersion objective and a 780 nM laser for excitation. ImageJ software (NIH, Bethesda, Maryland) was used to measure and compare the fluorescence intensity values associated with macrophages and tumor cells.

Results

Characterization of molecular probes LS301 and LS789

LS301 has demonstrated its ability to selectively identify precancerous and cancerous lesions in colon cancer, as well as several other adenocarcinomas[33-34]. In this study we explored its use for identifying precancerous and cancerous pancreatic lesions, and differentiating cancer from acute and chronic pancreatitis. The use of NIR fluorescence allows us to minimize tissue auto-fluorescence and avoid absorption by hemoglobin (<650 nm), and water and lipds (>900 nm). This allows for deeper tissue penetration, making non-invasive optical imaging possible. In order to better examine the binding preferences of LS301 towards pancreatic cancer and normal pancreas tissue, we conducted flow cytometric analyses utilizing several markers to identify specific cell

types. Due to lack of ability of the NIR FACS system to image in both the visible (panel of markers) and NIR (LS301) fluorescence, we developed an LS301 analog, LS789, which has excitation and emission spectra closer to the visible spectrum. The chemical structure and the fluorescence spectra (ex/em) of LS301 and LS789 are presented in Figure 1A and 1B, respectively.

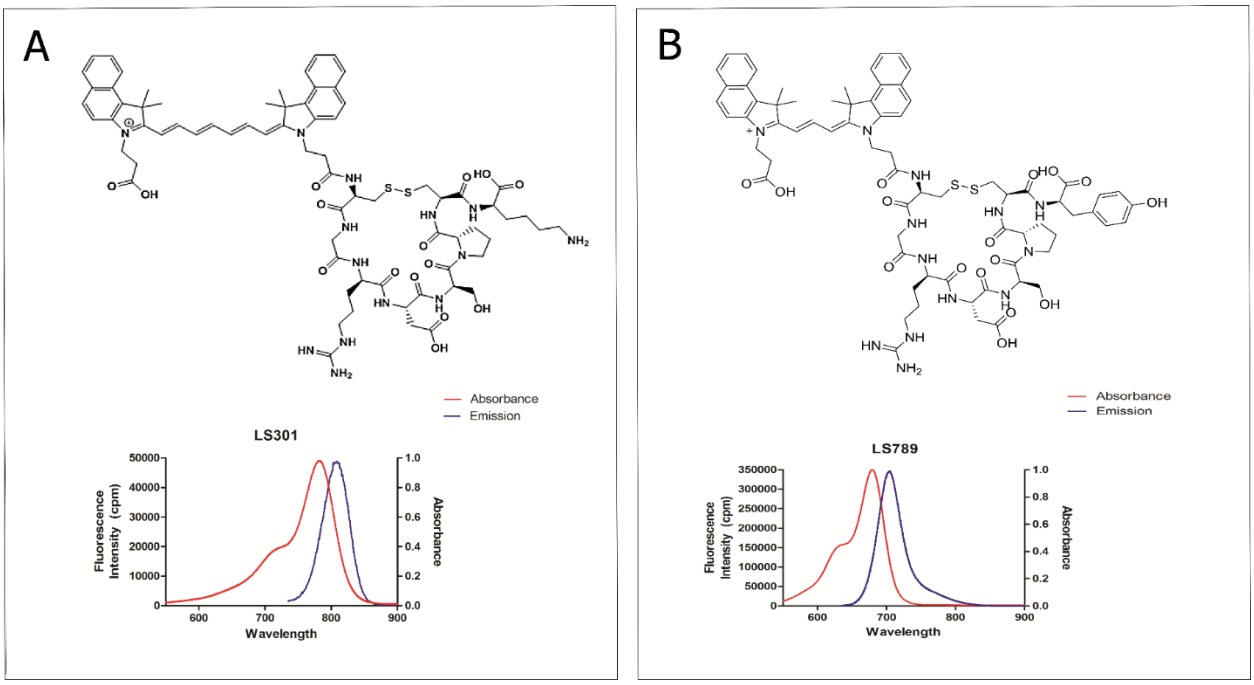

Figure 1: Structure and physical characteristics of molecular probes LS301 and LS789. (A) Chemical structure of LS301 Cypate-(c($_D$CGRDSPC)K) and (B) LS789 (analog of LS301)Cypate-3-cyclo($_D$Cys-Gly-Arg-Asp-Ser-Pro-Cys)-Lys-OH. Note the difference in normalized excitation and emission spectra of LS301 and LS789.

Fluorescence Molecular Tomography (FMT) imaging is able to distinguish PDAC from pancreatitis, non-invasively.

The goal of CT-FMT in this study was to utilize it as a first-pass diagnostic screening tool, prior to conducting any invasive laparoscopic procedures. Utilizing the molecular specificity of LS301 and overlaying the readout with CT imaging, we can gain insight into both structural and

molecular aspects of pancreatic tissue. To test this possibility, we utilized spontaneous KPC pancreatic cancer model to recapitulate precancerous (2.5 month stage) and cancerous (5-6 months stage; n=3) lesions. Alongside, orthotopic pancreatic cancer models (1 week stage; <0.5 cm tumor size, 2 week stage <1 cm tumor size; n=3), pancreatitis models (acute, chronic; n=3), and a control, sham surgery model (n=4) were developed to test efficacy of the molecular probe utilizing the detection platform. Figure 2 demonstrates the data collected by utilizing this CT-FMT method, where we specifically examined the region illustrated in Figure 2A. Unlike the KPC spontaneous model, in which the tumor generates within the pancreas, the orthotopic PDAC models presented with large tumors engulfed in the pancreatic head closer to the skin, while the tail maintained its anatomical position. For this reason, we obtained the signal at six mm depth in all the models to capture the pancreas and/or tumor in all models.

In order to non-invasively distinguish pancreatitis and pancreatic cancer, we utilized total fluorescence intensity as a tool for CT-FMT. Total fluorescence intensity was measured by summing all the voxels in the region of interest (common amongst all mice imaged). Total fluorescence intensity was five fold higher in PDAC and seven fold higher in KPC models than in control and acute pancreatitis models. A threshold value of $4E^{-5}$ was established for mean fluorescence intensity to distinguish pancreatitis and control models from PDAC tumor and KPC spontaneous tumors models, as shown in Figure 2B. This metric allowed for a very clear distinction between pancreatitis and control models, as compared to tumor models orthotopic and spontaneous PDAC.

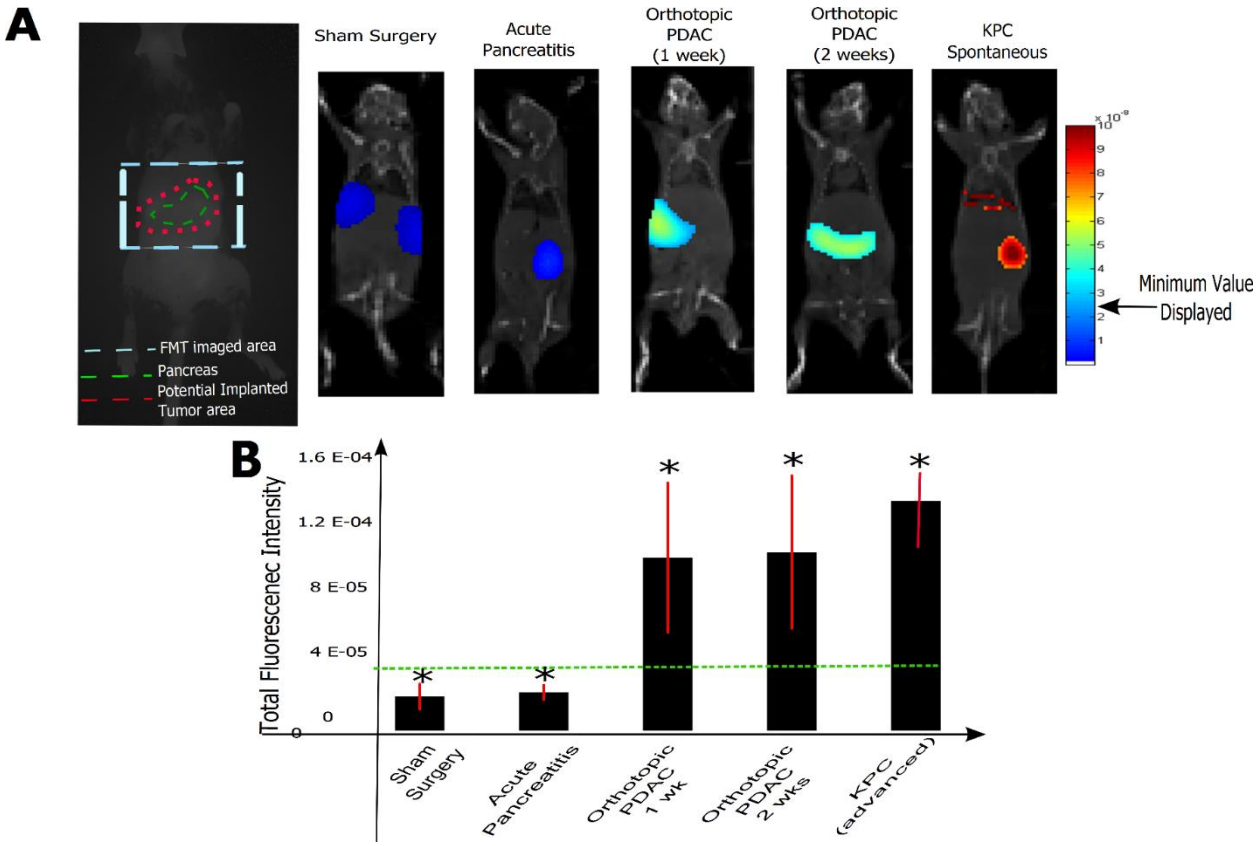

Figure 2: Non-invasive NIR CT-FMT imaging and analysis in control, acute pancreatitis, orthotopic PDAC, and KPC PDAC models. (A) Pancreas is outlined by the dotted green line, whereas the region where the implanted tumor extends is shown by the dotted red line. Dotted blue line marks the region that was imaged using the FMT system. Representative images of various murine models were super-imposed on their respective CT images. (B) Measured total fluorescence intensity values compared amongst control, acute pancreatitis, orthotopic and spontaneous PDAC models. Dotted green line represents a potential threshold established for the system that distinguishes pancreatitis and control from tumor models. Values represent mean ± SE, n = 3. $p < 0.05$

A NIR-capable endoscope is able to locate cancerous lesions for “smart biopsies"

NIR-based laparoscopy was used to validate the FMT findings, isolate precancerous and cancerous tissues, and ensure complete tumor resection. The signal established from FMT was used as a supplementary tool prior to each mouse surgery, as in certain cases the pancreatic tumor was hidden deeper within the core of the mouse’s body as shown in Figure 3A. Having

exposed the organs, mice that possessed orthotopically implanted or spontaneously generated tumors exhibited eight-ten-fold higher tumor-to-background ratios, whereas early KPC models exhibited six-fold higher TBR compared to normal pancreas in the sham surgery model as shown in Figure 3B. LS301 demonstrated a 100% specificity and sensitivity towards both precancerous and cancerous lesions. The chronic pancreatitis model demonstrated a close to three fold higher TBR than the sham surgery model and two fold higher than the acute pancreatitis, likely due to acinar to ductal metaplasia associated with prolonged tissue damage *via* caerulein.

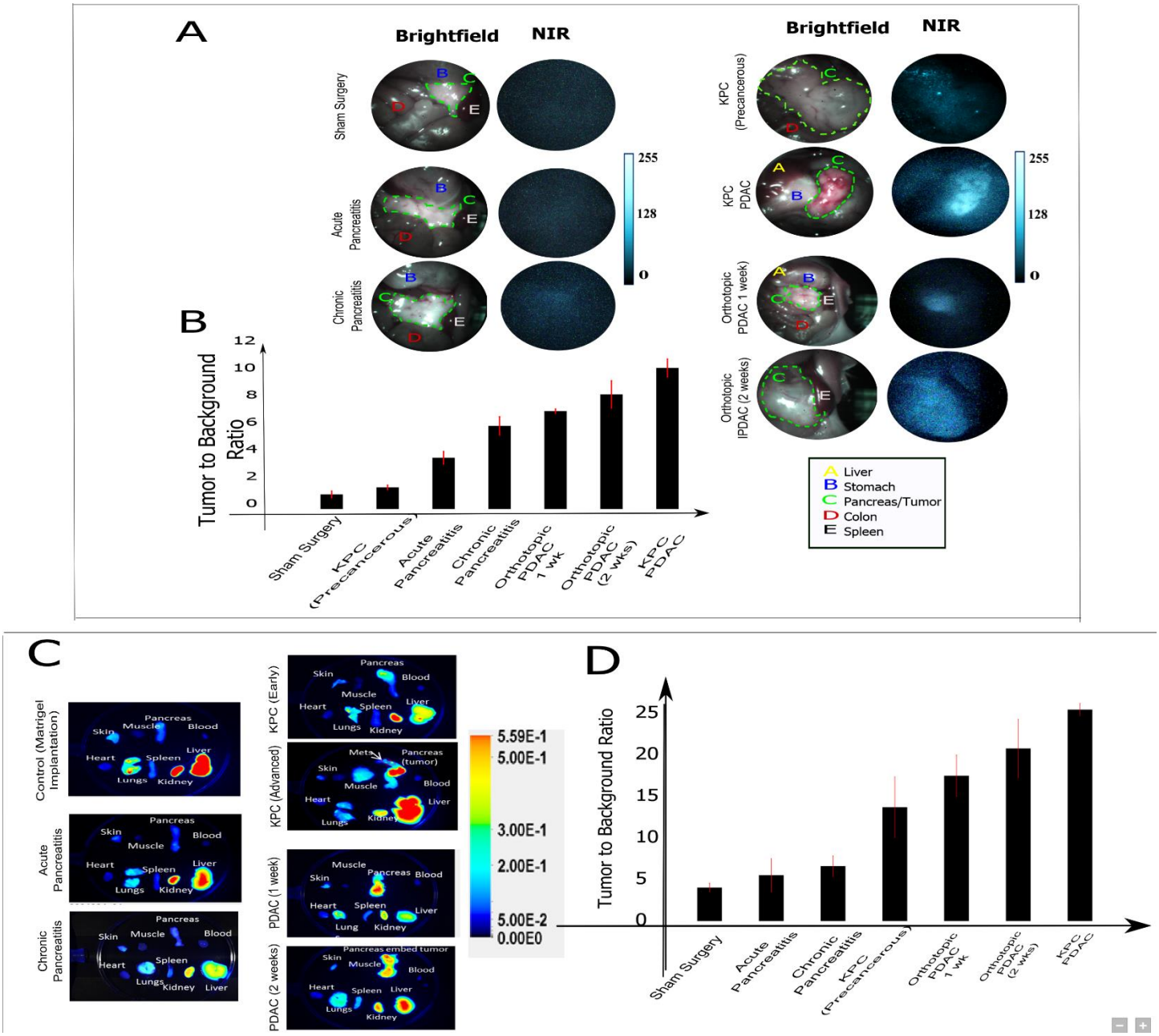

Figure 3: *In vivo* NIR fluorescence laparoscopy and *ex-vivo* biodistribution imaging of PDAC, pancreatiits, sham surgery models A) Brightfield and NIR images are presented with liver (A), stomach (B), pancreas/tumor (C), colon (D) and spleen (E). B) Tumor to background ratio measured and recorded by comparing fluorescence intensity values of pancreas/tumor and that arising from surrounding spleen region. C) *Ex-vivo* biodistribution imaging of skin, muscle, pancreas/tumor, blood, heart, lung, spleen, kidney and liver of all animal models tested. Normalized mean fluorescence intensity values are shown amongst various models: control, acute pancreatitis, and orthotopic PDAC (1 week),

orthotopic PDAC (2 week), and KPC tumor models. D) Tumor to background ratio of pancreas/tumor and spleen region in each respective model. Values represent mean ± SE, n = 3. $p < 0.05$

Efficacy study in pancreatic cancer and pancreatitis murine models using LS301

The goal of this portion of this study involving an established small animal imaging paradigm was to establish time point that provides maximum contrast between tumor and surrounding tissue, and validate findings from FMT and NIR laparoscopy *via ex vivo* biodistribution studies examining exteriorized organs as shown in Figure 3C. Having performed *in vivo* time course imaging on all animal models at 0, 1, 4, 24, and 48h, we obtained optimal tumor-to-background ratio (TBR) at 48h (Supplementary Figure 1). Orthotopic pancreatic tumor models demonstrated a TBR of 4.2 ± 0.5 and 6.02 ± 0.8, respectively. The KPC advanced tumor model demonstrated a TBR of 5.2 ± 0.4 whereas chronic pancreatitis and acute pancreatitis demonstrated TBR's of 1.6 ± 0.2 and 1.5 ± 0.2, respectively as shown in Figure 3D. It is important to note, however, that the small planar imaging system is limited to imaging only to depths of 8-10 mm, as opposed to the DOT which allows us to perform deeper volumetric imaging.

Comparing non-invasive, NIR FMT and guided, invasive NIR laparoscopy with ex-vivo bio-distribution imaging and validatory H&E

The TBR ratios obtained post sacrifice and biopsy, as shown in Figure 3D, consistently increased from a normal to diseased pancreas state (sham surgery model → acute, chronic pancreatitis → pre-cancerous PanIN → overt cancer models (PDAC and advanced KPC)), agreeing with the results obtained *via* FMT and NIR laparoscopy. The mean fluorescence intensity

values amongst models tested between FMT, NIR laparoscopy, and established planar imaging platform were reported in Figure 4A. Correlation coefficient values of 0.96 were obtained between FMT and NIR post-mortem biodistribution and of 0.98 between NIR laparoscopy and post-mortem biodistribution. Histological validation of models tested using H&E and their associated fluorescence intensities are presented in Figure 4B. Pancreas and associated tumor slice fluorescence shown demonstrates a similar, consistent phenomenon in which control and pancreatitis models have minimal NIR fluorescence intensity compared to tumor models. Interestingly, the chronic pancreatitis model demonstrated two-fold higher fluorescence intensity than the sham surgery model. Having cross-referenced with histology, regions that exhibited higher fluorescence intensity patterns appeared to be going through ductal transformation (as a result of PanIN progression).

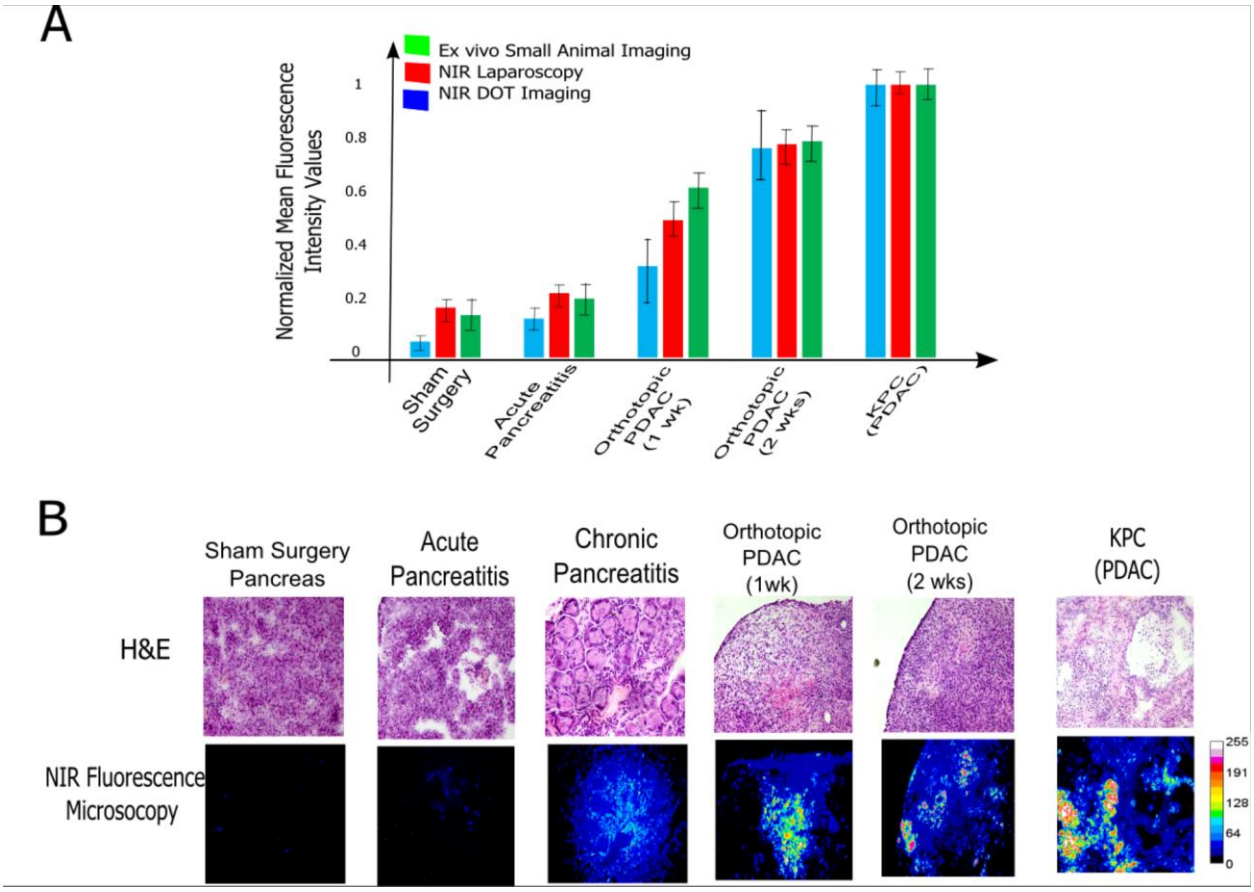

Figure 4. Comparing normalized mean fluorescence intensity amongst non-invasive NIR FMT imaging and NIR laparoscopy with *ex vivo* NIR biodistribution and gold-standard H&E. (A) Normalized MFI values compared for control, acute pancreatitis, orthotopic PDAC (1 week and 2 weeks) and KPC spontaneous PDAC models. (B) H&E and corresponding NIR fluorescence microscopy derived intensity of tissues amongst control, pancreatitis, and tumor models. Values represent mean ± SE, $n = 3$. $p < 0.05$

Targeted molecular probe LS301 has ability to identify similar regions within pancreatic tumors as CK19

In order to better understand the molecular probe binding preferences, we examined pancreatic tissue from pancreatitis, PDAC, and sham surgery models. Binding patters of LS301 to the pancreatic tissue were compared to known marker for pancreatic ductal adenocarcinoma, CK19 as shown in Figure 5. For the sham surgery model, <10% of the cells are CK19+ where only 0% of the cells are labeled with LS301. In the acute pancreatitis model, 30% of the cells are CK19+, whereas <10% of the cells are labeled with LS301. Orthotopic PDAC 1 week and 2 week models along with KPC show more than 60%, 70%, and 70% of the cells to be CK19+, respectively, whereas 55%, 75%, and 85% of the cells are labeled with LS301. This level of specificity towards precancerous and cancerous lesions prodded us to further investigate and validate binding patterns in various cell lines using flow cytometry.

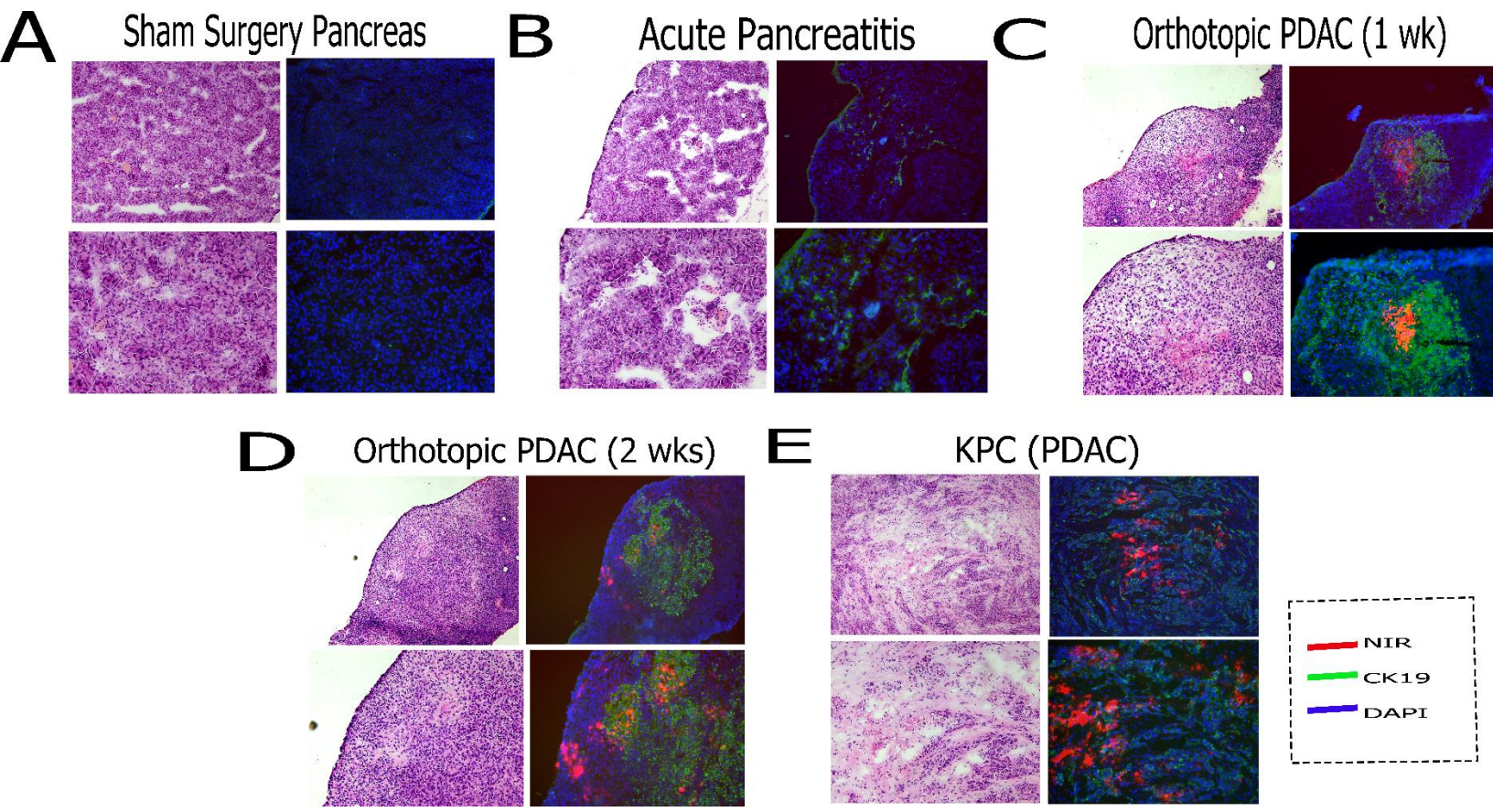

Figure 5: Immunohistochemistry and corresponding NIR fluorescence and histological verification in control pancreas, KRAS Ink, acute pancreatitis, and spontaneous KPC pancreatic tumor models. A) CK19 (green) binding pattern and DAPI (blue) stain of control sham implantation and corresponding NIR (yellow) signal and H&E staining. B) CK19 binding pattern and DAPI stain of acute pancreatitis model with corresponding NIR signal and H&E staining. C) CK19 binding pattern and mCherry+ (red) tumor cells in KRAS Ink model with DAPI stain and corresponding NIR signal. D) CK19 binding pattern and DAPI stain of KPC Spontaneous tumor and corresponding NIR signal and H&E staining. Values represent mean ± SE, n = 3. $p < 0.05$

LS301 and LS789 have binding specificity and selectivity towards pancreatic tumor cells and macrophages: a flow cytometry study

To determine what cell types within the tumor tissues bound the LS301, we injected LS789, analog of LS301, into PDAC tumor-bearing mice and performed flow cytometry analysis on dissociated tumor tissue to detect LS789 fluorescence signals in various cell types. Orthotopic PDAC tumor models were utilized to examine differences in the uptake of LS789 in a variety of cell types present in the tumor tissue or normal pancreas. We found robust uptake in PDAC tumor cells compared to normal pancreatic epithelial cells. By contrast internalization of the molecular probe was minimal in normal pancreatic cells, normal pancreatic fibroblasts, B cells, T cells and neutrophils (Supplementary Figure 2). Modest uptake was observed in tumor macrophages and some lower level uptake in tumor associated fibroblasts Figure 6. The modest uptake in macrophages could possibly be explained by phagocytosis of tumor cells that have bound probe. 80% of TAMs have been shown to have mCherry+ signal, which is derived from pancreatic tumor cells[35]. To distinguish phagocytosis from direct binding, we conducted *in vitro* studies using various pancreatic tumor cell lines and bone marrow derived macrophages (BMDM). PDAC tumor cells exhibited significantly higher fluorescent intensity than BMDMs, and this difference was greatest at the 6-hr time point. This further accentuates the specificity of the molecular probe towards tumor cells and also associates the signal in tumor-associated macrophages, as possibly due to phagocytosis or other non-specific uptake mechanisms.

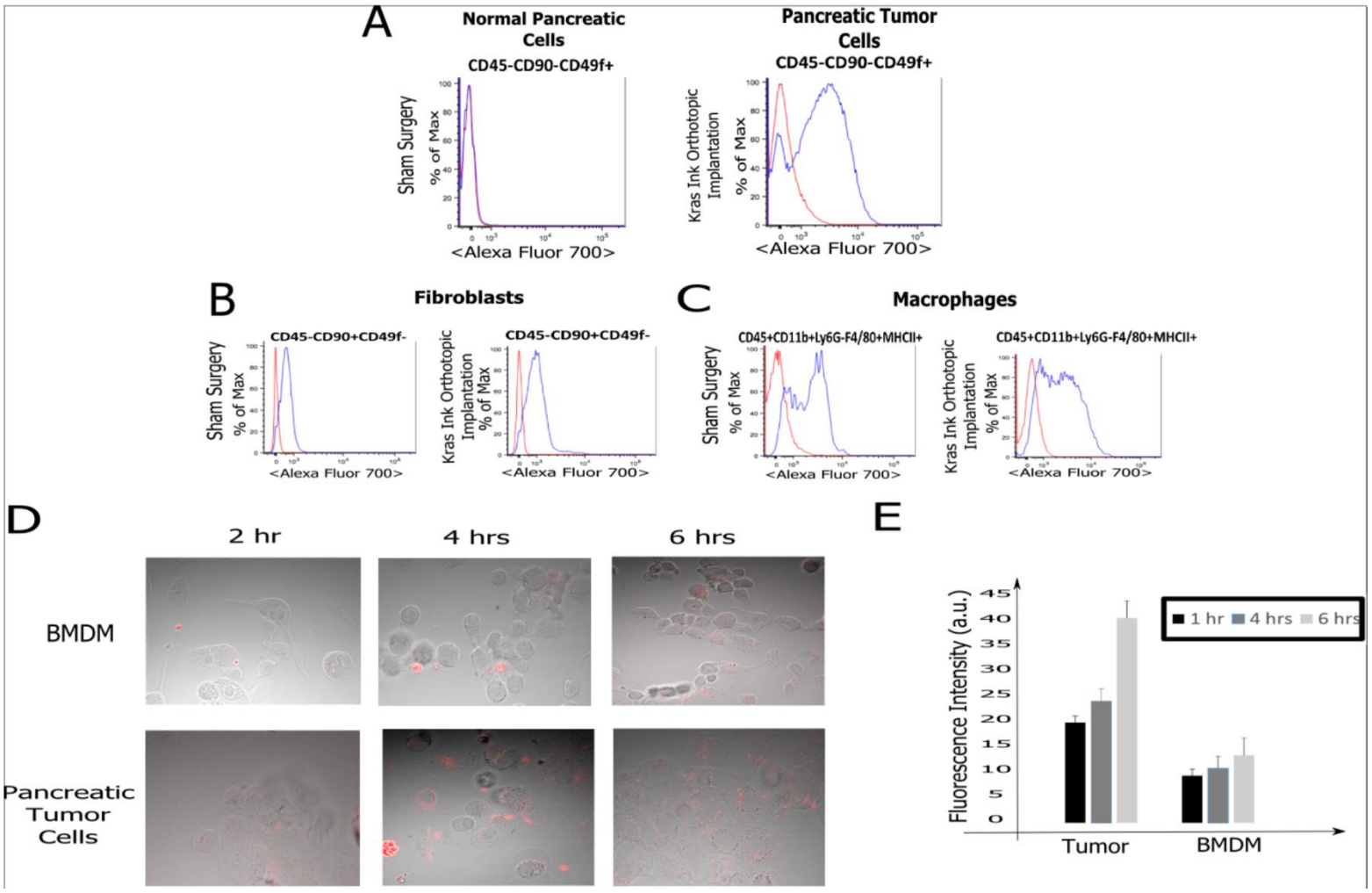

Figure 6: FACS data examining LS 789 in distinct tumor infiltrating immune cell types within control pancreas (sham implantation) and KRAS Ink pancreatic tumors. Binding was compared amongst (A) normal and tumor pancreatic cells, (B) fibroblasts, (C) macrophages, in sham surgery and Kras Ink orthotopic implanted tumor-bearing mice. (D) Time-lapse *in vitro* LS301 binding in bone-marrow-derived macrophages (BMDM), normal pancreatic cells, and pancreatic tumor cells. (E) Fluorescence intensity distribution in tumor, normal, BMDM at 2h, 4h, 6h. Values represent mean ± SE, n = 3. $p < 0.05$

Discussion

We have developed an imaging platform that encompasses three elements; a targeted molecular probe with enhanced specificity and sensitivity for detection of pancreatic lesions, FMT-CT for non-invasive differentiation of pancreatitis from pancreatic cancer, and NIR laparoscopy to guide "smart" biopsies. Unlike current clinical standards that are reliant on structural information and are invasive in nature, FMT-CT coupled with a targeted molecular probe allows us to take advantage of molecular-sensitive information associated with tissues and combine it with structural information. This combined approach allows for a non-invasive diagnosis method for pancreatic cancer versus pancreatitis. Conducting a highly sensitive non-invasive screen prior to a semi-invasive laparoscopic procedure, has been shown to reduce the complications associated with surgery and lower the risk of developing pancreatitis as a result of surgery. Furthermore, the use of a NIR-capable endoscope allows the surgeon to obtain "smart biopsies" and ensure complete resection.

To best recapitulate progression of pancreatic cancer at various stages, various models were employed. Using early and late stage spontaneous pancreatic cancer models, we were able to recapitulate pre-cancerous and cancerous lesions, respectively, which best represent human pancreatic cancer. Early and late stage orthotopic implantation models provided tumors of varying sizes and stages, making imaging systems' sensitivity in detecting lesions possible to test. Widely accepted caerulein-induced acute and chronic pancreatitis models demonstrated an abundance of neutrophils, edema, and necrosis, along with regions exhibiting ductal transformation (chronic pancreatitis models).

Our imaging platform is somewhat similar to SPECT-CT, where we have the ability to non-invasively identify molecular level information along with structural information. However,

due to depth limitations, the FMT imaging platform could be substituted by SPECT-CT by simply conjugating a SPECT contrast agent to the molecular probe, while retaining the targeting moiety. The versatility of the NIR-FMT was observed in its ability to report on the presence of tumors on the surface, as shown by the two-week PDAC orthotopic model, along with tumors up to 10 mm deep, such as in KPC model. It even provided the ability to report on tumors with even smaller nodules of sizes as low as 0.4 cm (1 week orthotopic PDAC), which was later verified *via* NIR laparoscopy and *ex vivo* biodistribution studies. Using metric such as total fluorescence intensity, we were able to establish thresholds and clearly distinguish pancreatitis from pancreatic cancer non-invasively, as shown in Figure 2. With the molecular probe's ability to selectively bind to pre-cancerous and cancerous lesions versus pancreatitis, a SPECT equivalent of the probe has immense potential to allow for a similar non-invasive diagnostic platform.

While the first half of the imaging platform demonstrates great potential for non-invasively screening patients for the presence/absence of pancreatic cancer, obtaining "smart" biopsies during the laparoscopic procedure still remains a huge concern. Our guided-NIR laparoscopy approach allowed us to identify tumors as small as 0.3 cm hidden deep within the cavity of the mouse. Furthermore, while the control and acute pancreatitis models demonstrated very minimal fluorescent signal, chronic pancreatitis, pre-cancerous and cancerous tumor models (early and late stage orthotopic and KPC advanced) demonstrated increasing TBR with disease progression as shown in Figure 3B. This trend was further validated *ex vivo,* as shown in Figure 3C and 3D. NIR laparoscopy serves as a strong validatory tool for NIR-FMT and provides a microscopic diagnosis of diseased tissue status with the potential to ensure complete tumor removal and minimize unnecessary biopsies.

The high level of specificity and sensitivity LS301 demonstrated towards pre-cancerous and cancerous lesions led us to compare its binding preferences to those of CK19, marker for PDAC known to correlate with aggressive phenotypes[36]. Both LS301 and CK19 binding patterns correlated extremely well within pancreatic tumor, and sham surgery models, as shown in Figure 6. However, the co-localization of binding patterns of LS301 and CK19 were not always similar, leading us to further investigate the cell types that exhibited higher uptake of LS301. Having conducted a flow cytometry study using control and pancreatic tumor bearing mice as shown in Figure 6A, we learned that pancreatic tumors exhibit a greater than 44-fold uptake of LS301 analog compared to normal pancreas. However, increased uptake was also observed in macrophages of the pancreatic tumor model possibly due to phagocytosis of tumor cells. To distinguish binding from phagocytosis, an *in vitro* study demonstrated four-fold higher uptake of LS301 in tumor cells versus BMDM.

The combination of a tumor-targeting molecular probe with an imaging platform that allows for a non-invasive-directed-guided intervention NIR laparoscopy provides a new paradigm for the accurate detection of pre-cancerous and cancerous pancreatic lesions versus pancreatitis. Moreover, this platform has the potential to stage oncogenesis and improve the management of pancreatic cancer in patients. The imaging platform and method described in this study are applicable to the assessment of other pathologic conditions, such as upper and lower GI lesions, lung carcinoma, and cardiovascular diseases.

References

1. Siegel R, Ma J, Zou Z, Jemal A. Cancer statistics, 2014. CA: a cancer journal for clinicians. 2014;64:9-29.
2. Abraham SC, Wilentz RE, Yeo CJ, Sohn TA, Cameron JL, Boitnott JK, et al. Pancreaticoduodenectomy (Whipple resections) in patients without malignancy: are they all 'chronic pancreatitis'? The American journal of surgical pathology. 2003;27:110-20.
3. Winter JM, Cameron JL, Campbell KA, Arnold MA, Chang DC, Coleman J, et al. 1423 pancreaticoduodenectomies for pancreatic cancer: A single-institution experience. Journal of gastrointestinal surgery : official journal of the Society for Surgery of the Alimentary Tract. 2006;10:1199-210; discussion 210-1.
4. Richter A, Niedergethmann M, Sturm JW, Lorenz D, Post S, Trede M. Long-term results of partial pancreaticoduodenectomy for ductal adenocarcinoma of the pancreatic head: 25-year experience. World journal of surgery. 2003;27:324-9.
5. van Gulik TM, Moojen TM, van Geenen R, Rauws EA, Obertop H, Gouma DJ. Differential diagnosis of focal pancreatitis and pancreatic cancer. Annals of oncology : official journal of the European Society for Medical Oncology / ESMO. 1999;10 Suppl 4:85-8.
6. Tessler DA, Catanzaro A, Velanovich V, Havstad S, Goel S. Predictors of cancer in patients with suspected pancreatic malignancy without a tissue diagnosis. The American Journal of Surgery.191:191-7.
7. Cote GA, Smith J, Sherman S, Kelly K. Technologies for imaging the normal and diseased pancreas. Gastroenterology. 2013;144:1262-71 e1.
8. Iftimia N, Cizginer S, Deshpande V, Pitman M, Tatli S, Iftimia NA, et al. Differentiation of pancreatic cysts with optical coherence tomography (OCT) imaging: an ex vivo pilot study. Biomedical optics express. 2011;2:2372-82.
9. Testoni PA, Mariani A, Mangiavillano B, Arcidiacono PG, Di Pietro S, Masci E. Intraductal optical coherence tomography for investigating main pancreatic duct strictures. The American journal of gastroenterology. 2007;102:269-74.
10. Furukawa T, Oohashi K, Yamao K, Naitoh Y, Hirooka Y, Taki T, et al. Intraductal ultrasonography of the pancreas: development and clinical potential. Endoscopy. 1997;29:561-9.
11. Hara T, Yamaguchi T, Ishihara T, Tsuyuguchi T, Kondo F, Kato K, et al. Diagnosis and patient management of intraductal papillary-mucinous tumor of the pancreas by using peroral pancreatoscopy and intraductal ultrasonography. Gastroenterology. 2002;122:34-43.
12. Gong TT, Hu DM, Zhu Q. Contrast-enhanced EUS for differential diagnosis of pancreatic mass lesions: a meta-analysis. Gastrointestinal endoscopy. 2012;76:301-9.
13. Vitale GC, Davis BR, Zavaleta C, Vitale M, Fullerton JK. Endoscopic retrograde cholangiopancreatography and histopathology correlation for chronic pancreatitis. The American surgeon. 2009;75:649-53; discussion 53.
14. Tamura R, Ishibashi T, Takahashi S. Chronic pancreatitis: MRCP versus ERCP for quantitative caliber measurement and qualitative evaluation. Radiology. 2006;238:920-8.

15. Meining A, Shah RJ, Slivka A, Pleskow D, Chuttani R, Stevens PD, et al. Classification of probe-based confocal laser endomicroscopy findings in pancreaticobiliary strictures. Endoscopy. 2012;44:251-7.
16. Bausch D, Thomas S, Mino-Kenudson M, Fernandez-del CC, Bauer TW, Williams M, et al. Plectin-1 as a novel biomarker for pancreatic cancer. Clinical cancer research : an official journal of the American Association for Cancer Research. 2011;17:302-9.
17. Charanya T, York T, Bloch S, Sudlow G, Liang KX, Garcia M, et al. Trimodal color-fluorescence-polarization endoscopy aided by a tumor selective molecular probe accurately detects flat lesions in colitis-associated cancer. Journal of biomedical optics. 2014;19.
18. Achilefu S, Jimenez HN, Dorshow RB, Bugaj JE, Webb EG, Wilhelm RR, et al. Synthesis, in vitro receptor binding, and in vivo evaluation of fluorescein and carbocyanine peptide-based optical contrast agents. Journal of medicinal chemistry. 2002;45:2003-15.
19. Aguirre AJ, Bardeesy N, Sinha M, Lopez L, Tuveson DA, Horner J, et al. Activated Kras and Ink4a/Arf deficiency cooperate to produce metastatic pancreatic ductal adenocarcinoma. Genes & development. 2003;17:3112-26.
20. Deer EL, Gonzalez-Hernandez J, Coursen JD, Shea JE, Ngatia J, Scaife CL, et al. Phenotype and genotype of pancreatic cancer cell lines. Pancreas. 2010;39:425-35.
21. Owens RB, Smith HS, Nelson-Rees WA, Springer EL. Epithelial cell cultures from normal and cancerous human tissues. Journal of the National Cancer Institute. 1976;56:843-9.
22. Smith HS. In vitro properties of epithelial cell lines established from human carcinomas and nonmalignant tissue. Journal of the National Cancer Institute. 1979;62:225-30.
23. Hingorani SR, Wang L, Multani AS, Combs C, Deramaudt TB, Hruban RH, et al. Trp53R172H and KrasG12D cooperate to promote chromosomal instability and widely metastatic pancreatic ductal adenocarcinoma in mice. Cancer cell. 2005;7:469-83.
24. Olive KP, Jacobetz MA, Davidson CJ, Gopinathan A, McIntyre D, Honess D, et al. Inhibition of Hedgehog signaling enhances delivery of chemotherapy in a mouse model of pancreatic cancer. Science. 2009;324:1457-61.
25. Mitchem JB, Brennan DJ, Knolhoff BL, Belt BA, Zhu Y, Sanford DE, et al. Targeting tumor-infiltrating macrophages decreases tumor-initiating cells, relieves immunosuppression, and improves chemotherapeutic responses. Cancer research. 2013;73:1128-41.
26. Niederau C, Ferrell LD, Grendell JH. Caerulein-induced acute necrotizing pancreatitis in mice: protective effects of proglumide, benzotript, and secretin. Gastroenterology. 1985;88:1192-204.
27. Otsuki M, Yamamoto M, Yamaguchi T. Animal models of chronic pancreatitis. Gastroenterology research and practice. 2010;2010:403295.
28. Nothdurft RE, Patwardhan SV, Akers W, Ye Y, Achilefu S, Culver JP. In vivo fluorescence lifetime tomography. Journal of biomedical optics. 2009;14:024004.
29. Ntziachristos V, Weissleder R. Experimental three-dimensional fluorescence reconstruction of diffuse media by use of a normalized Born approximation. Optics letters. 2001;26:893-5.
30. O'Leary MA, Boas DA, Li XD, Chance B, Yodh AG. Fluorescence lifetime imaging in turbid media. Optics letters. 1996;21:158-60.

31. Haskell RC, Svaasand LO, Tsay TT, Feng TC, McAdams MS, Tromberg BJ. Boundary conditions for the diffusion equation in radiative transfer. Journal of the Optical Society of America A, Optics, image science, and vision. 1994;11:2727-41.
32. Achilefu S, Bloch S, Markiewicz MA, Zhong T, Ye Y, Dorshow RB, et al. Synergistic effects of light-emitting probes and peptides for targeting and monitoring integrin expression. Proceedings of the National Academy of Sciences of the United States of America. 2005;102:7976-81.
33. Charanya T, York T, Bloch S, Sudlow G, Liang K, Garcia M, et al. Trimodal color-fluorescence-polarization endoscopy aided by a tumor selective molecular probe accurately detects flat lesions in colitis-associated cancer. Journal of biomedical optics. 2014;19:126002.
34. Liu Y, Bauer AQ, Akers WJ, Sudlow G, Liang K, Shen D, et al. Hands-free, wireless goggles for near-infrared fluorescence and real-time image-guided surgery. Surgery. 2011;149:689-98.
35. Zhu Y, Knolhoff BL, Meyer MA, Nywening TM, West BL, Luo J, et al. CSF1/CSF1R Blockade Reprograms Tumor-Infiltrating Macrophages and Improves Response to T Cell Checkpoint Immunotherapy in Pancreatic Cancer Models. Cancer Res. 2014.
36. La Rosa S, Rigoli E, Uccella S, Novario R, Capella C. Prognostic and biological significance of cytokeratin 19 in pancreatic endocrine tumours. Histopathology. 2007;50:597-606.

Chapter 6

Conclusions

In this dissertation, we have explored a novel way of addressing clinically relevant problems such as detection of precancerous and cancerous lesions in colorectal and pancreatic cancer. Flat lesions in CAC have been particularly hard to detect given their physical appearance. Efforts thus far suffer from poor specificity and sensitivity of detection. We devised a novel approach that takes advantage of two modalities which have immense potential in capturing both physical as well as molecular abnormalities associated with cancerous lesions. Furthermore, we were able to develop a novel topical administration strategy, which ensures even distribution of molecular probe for "incubation" and allows for selective uptake. Given the use of dye in colonoscopy procedures in cases of dysplasia has become mandatory, this novel method has some great potential implications in future practice. Collaborating with clinicians, we were able to capture appropriate animal models to best test our FP endoscopy and targeted molecular probe approaches. Furthermore, with the complementary fluorescence-polarization microscopy approach, we were able to offer a rapid, structural and molecular diagnosis immediately post biopsy to potentially circumvent H&E analysis altogether and lower risks associated with repeated surgeries. Lastly, we were able to extend our application towards differentiation of pancreatic cancer from pancreatitis using the targeted molecular probe and a non-invasive guided imaging platform that allows us to take "smart biopsies". Optical imaging platforms involving fluorescence-polarization endoscopy or fluorescence molecular tomography aided laparoscopy for invasive or noninvasive diagnostic imaging holds great promise in shifting the paradigm of surgical oncology in the future.